THERMAL DESIGN AND OPTIMIZATION OF HIGH TORQUE DENSITY ELECTRIC MACHINES

A Thesis
Presented to
The Academic Faculty

by

S. Andrew Semidey

In Partial Fulfillment
of the Requirements for the Degree
Doctor of Philosophy in the
G. W. Woodruff School of Mechanical Engineering

Georgia Institute of Technology
August 2012

THERMAL DESIGN AND OPTIMIZATION OF HIGH TORQUE DENSITY ELECTRIC MACHINES

Approved by:

Dr. J. Rhett Mayor, Advisor
G. W. Woodruff School of Mechanical Engineering
Georgia Institute of Technology

Dr. Bert Bras
G. W. Woodruff School of Mechanical Engineering
Georgia Institute of Technology

Dr. Ronald G. Harley
School of Electrical and Computer Engineering
Georgia Institute of Technology

Dr. Sheldon Jeter
G. W. Woodruff School of Mechanical Engineering
Georgia Institute of Technology

Dr. Yogendra Joshi
G. W. Woodruff School of Mechanical Engineering
Georgia Institute of Technology

Date Approved: 6/29/2012

In Dedication to my beautiful intelligent wife, Laura

ACKNOWLEDGEMENTS

I would like to thank my committee members, Dr. Bras, Dr. Harley, Dr. Jeter, and Dr. Joshi, for their time and effort. Their help has greatly influenced this work for the better.

I would also like to thank my colleagues in the Electrical Engineering department, Yao Duan, Siwei Cheng, and Yi Du, for their collaboration. This work would not have been possible without their help.

I am grateful to my labmates for the lively discussions and debates that have helped me become a better collaborator and engineer. I would like to thank the undergraduates who have assisted me in my research, particularly David Judah for his countless hours of machining and metrology.

I am especially grateful to Dr. J. Rhett Mayor. He has challenged me to become the engineer and researcher I am today. Without his help, I would not have pursued a doctoral degree.

Most importantly, I would like to thank my wife Laura. She has lovingly supported my efforts through this entire process. I would have been lost without her companionship.

TABLE OF CONTENTS

LIST OF TABLES

LIST OF FIGURES

SUMMARY

The overarching goal of this work is to address the design of next-generation, high torque density electrical machines through numerical optimization using an integrated thermal-electromagnetic design tool that accounts for advanced cooling technology. The goal was accomplished by first developing a parametric thermal model of electric machines. The thermal model was implemented using a finite difference approach. The model was extended to include a novel advanced cooling technology termed the direct winding heat exchanger (DWHX). The advanced cooling technology involves placing a heat exchanger directly next to the windings in the stator, thereby dramatically improving the thermal transport within the machine and increasing torque density. The DWHX requires a high convection coefficient with low pressure drop. The heat transfer to pressure drop tradeoff was addressed by developing an empirically based Nusselt number and friction factor correlation for micro-hydrofoil enhanced meso-channels. The parametric thermal model, advanced cooling technique, Nusselt number correlation, and friction factor correlation were combined with an electromagnetic model. The integrated thermal-electromagnetic model was then used in conjunction with particle swarm optimization to determine optimal conceptual designs.

CHAPTER 1

INTRODUCTION

The overarching goal of the proposed research is to enhance the design of next-generation, high torque density electrical machines through numerical optimization using an integrated thermal-electromagnetic design tool that accounts for advanced cooling technology. 99% of electric machines are commodity machines. Commodity machines typically run at a constant load and speed, such as motors for conveyer belts, fans, or pumps. An example of these standard machines produced by Baldor is presented in Figure 1.1. These machines are typically designed as standalone units and the designs do not vary with the application. This type of design is known as a machine-centric design and means the end users must select a standard motor from a product line to fit their application. This machine-centric design works well for commodity machines, but there has been an increase in applications that require non-commodity machines.

Figure 1.1 - Typical commodity electric machines[1]

Recently there has been a push to develop "more electric" vehicles. "More electric" vehicles have higher system efficiencies by using electric machines instead of

other less efficient systems. Some examples of these applications are shown in Figure 1.2.

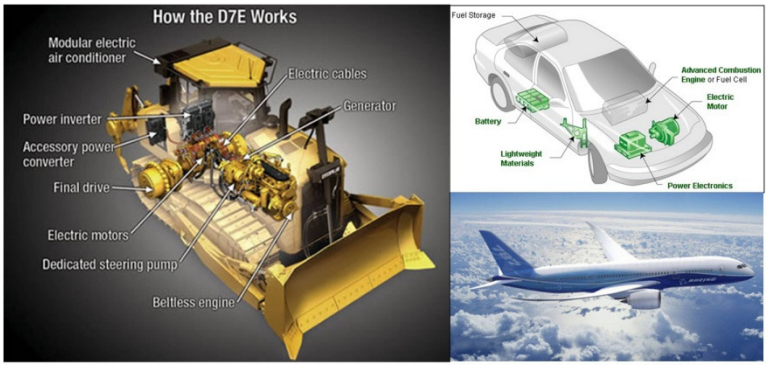

Figure 1.2 - Applications that require Application-Centric machine design[2-4]

Figure 1.2 shows the first hybrid bulldozer developed by Catepillar, a typical hybrid electric vehicle, and the Boeing 787 Dreamliner. Commodity machines are not suited for applications in which load and speed change dramatically. Furthermore, commodity machines are typically significantly over designed, leading to heavy and large machines that are not suited for weight and volume restricted applications. Such applications require electric machines that are specifically designed for the specific duty cycle of the application. Thus, the design of these machines must change to application-centric designs, which is different from the machine-centric design paradigm that dominates commodity machine design methodology.

Currently the application-centric design process is modeled off the machine-centric design process. The machine-centric traditional design process is illustrated in Figure 1.3.

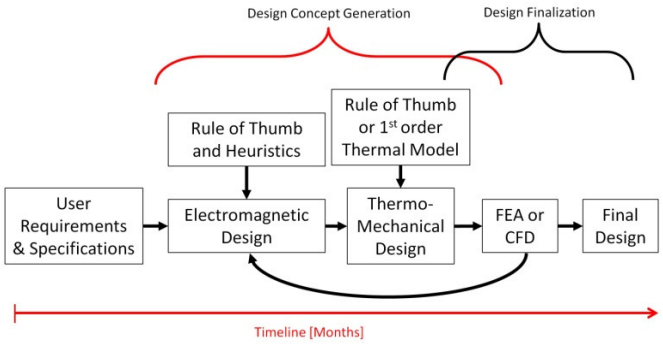

Figure 1.3 - Traditional electric machine design process

The design process begins with the user requirements and specifications. In the application-centric design, these requirements and specifications depend on the specific application. Next, the electromagnetic design is preformed. The electromagnetic design is currently dominated by rule of thumb and heuristics gained through the experience of the designer. Once the electromagnetic design is completed, the mechanical design is preformed. The mechanical design is also dominated by rule-of-thumb and first-order thermal models. The design is then analyzed using finite element analysis (FEA) and/or computational fluid dynamics (CFD) to confirm performance and thermal limits. If the temperature rise is above the acceptable limit for the available cooling, the electromagnetic design must be redone. However, temperature rise is a multi-physics problem that can be manipulated by varying several combinations of electromagnetic design parameters. Design iterations continue until all design requirements, specifications, and thermal limits are satisfied. This design method is inefficient and time consuming, potentially lasting months, and often leading to over- or under-designed machines. With new applications emerging weekly, electric machine designers need a way to quickly and effectively design application specific electric machines. A new

application-centric design process is required to reduce the design process cycle time and provide near optimal electric machine designs.

This dissertation proposes an advanced application-centric design process as illustrated in Figure 1.4.

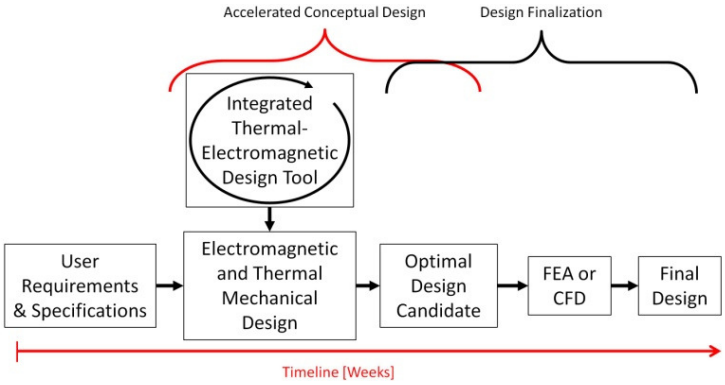

Figure 1.4 - Accelerated conceptual design process

The key to reducing the design cycle time is to incorporate an accelerated conceptual design process. The idea of accelerated conceptual design replaces the rule of thumb and heuristics from the traditional design process. Accelerated conceptual design means that several conceptual designs are quickly generated. The performances of all conceptual designs are compared and the optimal conceptual design is indentified. This optimal conceptual design can then be finalized with the use of FEA and/or CFD. A design tool is required to quickly generate and evaluate each conceptual design. This design tool must combine thermo-mechanical and electromagnetic models to evaluate the performance of the conceptual design. The design tool must also be computationally efficient to reduce conceptual design performance evaluation. Current design tools suffer from two substantial deficiencies. The first is the selection of electromagnetic design parameters, which are currently dominated by heuristics and empirical curves. The second is limitations in thermo-mechanical design models. Current thermo-mechanical design tools

are limited by three factors; poor thermal models, misguided duty cycle design methods, and lack of advanced cooling technology.

This dissertation focuses on the limitations of current thermo-mechanical design models. The first deficiency is the poor thermal models of electric machines. Classical thermal modeling of electric machines approximates the machine as a cylinder to simplify thermal analysis [5]. The current advanced methods for modeling the thermal transport in electric machines include thermal circuit approaches and numerical techniques such as FEA or CFD [6]. These methods have significant drawbacks, which limit their use as parametric design tools. Thermal circuits are fast to solve but require experimental fitting of parameters. Furthermore, thermal circuits are not able to fully capture temperature gradients within the machine, which drastically increase with improved cooling. FEA and CFD are generic, but suffer significant setup up and computational times. A parametric, fast-solving, thermal model of an electric machine that predicts the spatial- temporal temperature distribution is needed.

The second deficiency is misguided duty cycle design methods. Currently machines are designed to operate at steady state. The transient response of the machine is an afterthought in the design process. If the machine heats up too quickly at high loads, the designer simply adds more material to increase the thermal capacitance. Furthermore, the typical transient response considered is a response to a step input. This imparts an impulsive response, termed a quasi-transient response in this study, in which the machine eventually reaches a steady state temperature profile. A periodic thermal response, termed a fully-transient response in this study, is one in which the load continually changes with time as illustrated in Figure 1.5.

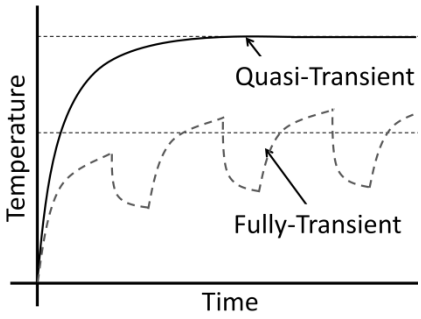

Figure 1.5 - Illustration of Quasi- vs. Fully- transient

The continually changing load profile more closely represents real world applications. Designing for the actual load cycle, instead of steady state responses, results in smaller, lighter machines.

The final deficiency is the lack of advanced cooling in electric machines. Typically, electric machines are cooled through the frame. Figure 1.6 illustrates the conduction paths from the heat source (copper windings) to the frame. The heat is typically dissipated from the frame to the ambient through natural convection, forced convection, or water jackets. These conduction paths are long and go through low thermal conductivity materials.

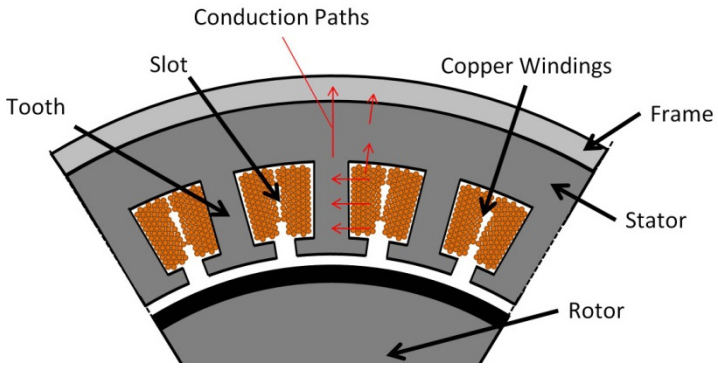

Figure 1.6 - Illustration of conduction paths in a permanent magnet electric machine

The thermal conductivity of magnetic steel is on the same order as stainless steel. The copper windings are composed of copper, epoxy insulation, and a filler material, typically

air. The effective thermal conductivity of the windings is low due to the low thermal conductivity of the insulation and filler material. The effective thermal conductivity can be increased by increasing the thermal conductivity of the filler material. However, the conduction paths to the frame are still long and must travel through the low thermal conductivity magnetic steel. An advanced cooling technique that reduces these conduction paths would dramatically increase thermal performance of electric machines.

This work will provide a detailed account of a thermo-mechanical design tool that addresses the deficiencies identified above. Chapter 2 details the steady state thermal model of electric machines. Chapter 3 details the transient thermal model that accounts for both quasi- and fully-transient load cycles in electric machines. Chapter 4 details the proposed advanced cooling approach for use in electric machines. Chapter 5 and Chapter 6 present the development of Nusselt number and friction factor correlations. These correlations are used in the design of the proposed advanced cooling method for electric machines. Chapter 7 details the optimization of an electric machine with advanced cooling utilizing an integrated thermal-electromagnetic design tool. The conclusions, contributions, and recommendation for future work are presented in Chapter 8. A detailed review of salient literature is provided within each relevant chapter.

CHAPTER 2

STEADY STATE PARAMETRIC THERMAL MODELING OF ELECTRIC MACHINES

2.1 Introduction

This chapter presents a steady-state parametric thermal model of a permanent magnet (PM) electric machine. The model has been implemented using a finite difference (FD) approach. The algorithm used to solve the FD approach is self-meshing and self-segmenting, only requiring nine geometric parameters to define the machine. This chapter develops a slot transformation technique and verifies it to within 2% accuracy. This chapter also develops a frame modeling approach and verifies it to within 5% accuracy. The proposed algorithm is able to solve a 100,000 node temperature field in 1.1s, resulting in significant gains in computational speed over widely adopted finite element analysis (FEA) approaches. This fast-solving parametric model enables closed loop machine design once integrated with an electromagnetic model.

2.2 Review of Salient Literature

Classical thermal electric machine design approximates the motor as a cylinder to simplify thermal analysis [5]. The current advanced methods for modeling the thermal transport in electric machines include thermal circuit approaches and numerical techniques such as FEA or CFD [6]. However, these methods have significant drawbacks, which limit their use as parametric design tools.

The thermal circuits approach was initially presented by Mellor et al in 1991 [7]. Importantly, this original study noted that some resistances could not be directly calculated and must be experimentally measured and applied to the model. Following this

work many authors proposed simplified thermal circuit networks to reduce the complexity of the initial formulation for different machine topologies and exterior boundary conditions [8-17]. The simplest of these models utilizes three thermal resistances (of the frame, stator and rotor) that are calculated from experimental temperature and loss data [18, 19]. Boglietti et al conducted extensive research in formulating the experimentally fit thermal resistance values for use in the thermal circuits method [20-23]. These experimentally fit thermal resistance values were used to develop the thermal simulation software MotorCAD. This software transforms user inputs detailing machine geometry into a thermal circuit network. This network is based on analytical and experimentally fit thermal resistance values from geometrical similar machines [24-27].

The thermal circuits approach is computationally inexpensive, but has the drawback of relying on experimental fitting of the thermal resistance parameters. The calibration required for the thermal circuit models of electric machines limits this modeling approach to a predictive model rather than a parametric design tool. Consequently, there has been significant interest in using physics-based FEA tools that do not rely on experimental data to model thermal transport in electric machines.

The first work in which FEA was used to evaluate temperature distribution in electric machines was done in 1980 by Armor [28]. This work involved a 3-D thermal simulation of a turbine generator rotor. FEA has shown to provide accurate predictions of temperature fields in electric machines [29, 30]. In recent years, FEA results have been compared to thermal circuits and used to calibrate thermal circuits [6, 10, 24]. CFD has mostly been used to evaluate heat transfer coefficients for use in thermal circuits instead

of well known heat transfer correlations [6, 15, 31]. Liao et al used CFD to solve the temperature distribution in an induction machine [32]. Both FEA and CFD are geometrically generic, but typically have long setup up and computational times, which limit their use as design selection tools. This work presents a steady-state parametric thermal model of an electric machine that does not require experimental calibration. This thermal model is solved in a computationally efficient manner thus leading to fast solution times. This provides a preferential trade-off between computational accuracy and solution speed that allows for rapid, high fidelity, temperature field predictions. Resultantly, the proposed thermal modeling approach could be integrated with an electromagnetic design approach to produce a multi-physics design tool. This design tool can be used for closed loop thermo-electro-mechanical design evaluation to rapidly select an optimal electric machine design candidate thus reducing the design generation time as compared to traditional electric machine design.

2.3 Thermal Modeling of Electric Machines

It is vital to understand the basics and complexities of thermal modeling of electric machines. The temperature rise of the machine is due to several loss components including copper loss (ohmic heating), core loss, windage loss, and frictional loss. There is also heat dissipation through either an active or passive cooling typically in the form of a convective load as illustrated in Figure 2.1. The complexity of thermal modeling is due to the composition of materials that form the machine including magnetic steel, copper and lacquer, slot liner paper, aluminum, etc. The anisotropy in the thermal conductivity of the materials such as the stator windings also adds to the complexity thermal modeling.

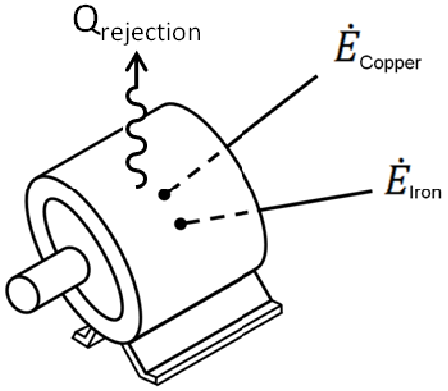

Figure 2.1 - Illustration of thermal problem in electric machines

Equation (2.1) is the heat diffusion equation in cylindrical coordinates, which governs the steady state temperature within a cylindrical geometry. This equation is extremely difficult to solve analytically for electric machines due to the complexities of the geometry, loads, and cooling presented above and a solution may not exist.

$$\frac{1}{r}\frac{\partial}{\partial r}\left(kr\frac{\partial T}{\partial r}\right)+\frac{1}{r^2}\frac{\partial}{\partial \theta}\left(k\frac{\partial T}{\partial \theta}\right)+\frac{\partial}{\partial z}\left(k\frac{\partial T}{\partial z}\right)+\dot{E}=0 \tag{2.1}$$

In (2.1), $\dot{E}$ is the heat generated per unit volume. In a typical thermal electric machine model, the only heat losses that are considered are the core and copper loss, because the other losses are much smaller in magnitude. The heat generated by the windings and the iron are defined by (2.2) and (2.3).

$$\dot{E}_{copper}=\frac{I^2\cdot R}{V_{windings}} \tag{2.2}$$

$$\dot{E}_{iron}=\frac{\dot{E}_{core\ loss}}{V_{iron}} \tag{2.3}$$

In (2.2), I is the single phase RMS current, R is the total phase resistance of the wire, $V_{windings}$ is total volume of the windings including the end-windings. In (2.3), $\dot{E}_{core\ loss}$ is the core loss which can estimated from an electromagnetic simulation and V_{iron} is the total

volume of the stator. This formulation of the heat generated assumes that the copper and core loss are evenly distributed through their respective volumes, which in most cases is a fair assumption.

Equation (2.4) defines the heat that is rejected from the frame of the electric machine to the ambient. The total heat rejection from the outer surface of the frame of the electrical machine is the summation of the heat rejected due to radiation effects and convective effects. The radiation effects will be pronounced under natural convection boundary conditions, wherein the heat rejection due to the radiation transfer is of the same order as the convective transfer. However, under forced convection boundary conditions the increased convective transfer will dominate over the radiation transfer effects.

$$Q_{rejection} = \left(h_{convection} + h_{radiation}\right) \cdot A_s \cdot \left(T_f - T_\infty\right) \tag{2.4}$$

In (2.4), $h_{convection}$ is the convection heat transfer coefficient, $h_{radiation}$ is the radiation heat transfer coefficient, A_s is the surface area of the frame, T_f is that temperature of the frame, and T_∞ is the ambient temperature. The radiation heat transfer coefficient is a linearization of the fourth order radiation heat transfer equation and is calculated as seen in (2.5).

$$h_{radiation} = \varepsilon \cdot \sigma \cdot \left(T_f + T_\infty\right) \cdot \left(T_f^2 + T_\infty^2\right) \tag{2.5}$$

In (2.5), ε is the emissivity of the frame surface and σ is the Stefan-Boltzmann constant (5.67e-8 $W/m^2\text{-}K^4$). The convection coefficient is calculated as seen in (2.6).

$$h_{convection} = Nu \cdot \frac{L_c}{k} \tag{2.6}$$

In (2.6), Nu is the Nusselt number, L_c is the characteristic length of the geometry, and k is the thermal conductivity of the fluid. The Nusselt number is dimensionless ratio between conduction and convection heat transfer at the surface-fluid interface and is calculated using heat transfer coefficient correlations. These correlations are well known throughout the heat transfer community and can be found in most general heat transfer texts for various conditions. The heat transfer correlations used in this work stem from the boundary conditions that were investigated as illustrated in Figure 2.2. These boundary conditions, smooth frame under buoyancy and forced flow, were selected because they represent typical frame styles seen in practice. For buoyancy driven flow, natural convection, the orientation has an effect on the heat transfer coefficient and must be accounted for.

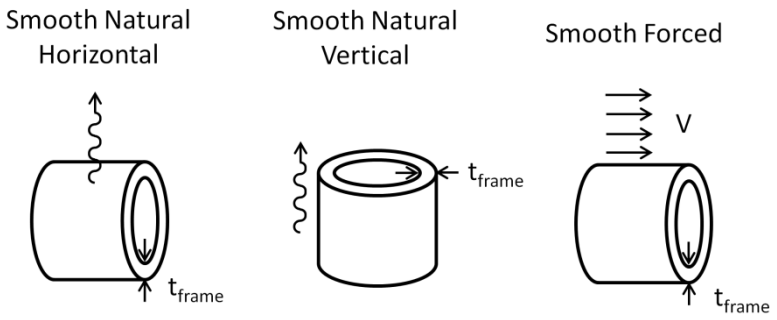

Figure 2.2 - Boundary conditions to be considered

Under natural convection, the Nusselt number is a function of Rayleigh number and Prandtl number. The Rayleigh number is a dimensionless ratio of buoyancy effects to viscous effects as seen in (2.7) and the Prandtl number is dimensionless ratio of viscosity to thermal diffusivity as seen in (2.8). Under forced convection, the Nusselt number is a

function of Reynolds number and Prandtl number. Reynolds number is a dimensionless ratio between momentum and viscosity as seen in (2.9).

$$Ra = \frac{g\beta(T_s - T_\infty)L_c^3}{\nu\alpha};\ \mathrm{Pr} = \frac{\nu}{\alpha};\ \mathrm{Re} = \frac{VL_c}{\nu} \qquad (2.7), (2.8), \& (2.9)$$

In (2.7), g is the acceleration due to gravity, β is the coefficient of expansion defined as the inverse of absolute temperature, ν is the kinematic viscosity, and α is the thermal diffusivity. In (2.9), V is the velocity of the fluid.

The Nusselt number correlation for a smooth frame under natural convection in a horizontal configuration is seen in (2.10). For a smooth frame under natural convection in a vertical configuration, the Nusselt number correlation is seen in (2.11).

$$Nu_{hor} = \left[\left(\left(1.93^{1.07} + (0.912\cdot\chi)^{1.07}\right)^{1/1.07}\right)^{10} + \left(0.1038\cdot Ra^{1/3}\right)^{10}\right]^{1/10};\ where, \qquad (2.10)$$

$$Nu_{ver} = \left[\left(\left(1.93^{1.07} + (0.792\cdot\chi)^{1.07}\right)^{1/1.07}\right)^{10} + \left(0.087\cdot Ra^{1/3}\right)^{10}\right]^{1/10};\ where, \qquad (2.11)$$

$$\chi = Ra^{1/4}\cdot 0.671/\left(1+(0.492/\mathrm{Pr})^{9/16}\right)^{4/9}$$

Equation (2.12) shows the Nusselt number correlation for a smooth frame under forced convection.

$$Nu = \left(0.037\cdot \mathrm{Re}^{4/5} - 871\right)\cdot \mathrm{Pr}^{1/3} \qquad (2.12)$$

These definitions for heat generation and rejection can be used in a numerical solution to obtain the temperature distribution within an electric machine.

Further simplifications to the thermal model are made to increase computation efficiency without significantly sacrificing accuracy. Thermal transport to the rotor is

ignored because in PM machines the rotor is not a heat source. Furthermore the windings are modeled as a lumped mass with an effective thermal conductivity which is typical in most thermal simulations [32]. Many geometric simplifications can be made as well.

The geometric symmetry of the electric machine enables further simplification of the model leading to even greater computational efficiency. Considering the radial symmetry of the stator, illustrated in Figure 2.3A, adiabatic boundaries can be implemented in order to create a simplified stator model, presented in Figure 2.3B, that is typically know as the half slot model. However, many stator geometries have features that are not described easily in cylindrical coordinates; the features are not defined by a combination of radii and angles. Therefore, a transformation is developed in order to convert the geometries of existing slot-types into slot geometries that are uniquely described by parametric descriptions in cylindrical coordinates.

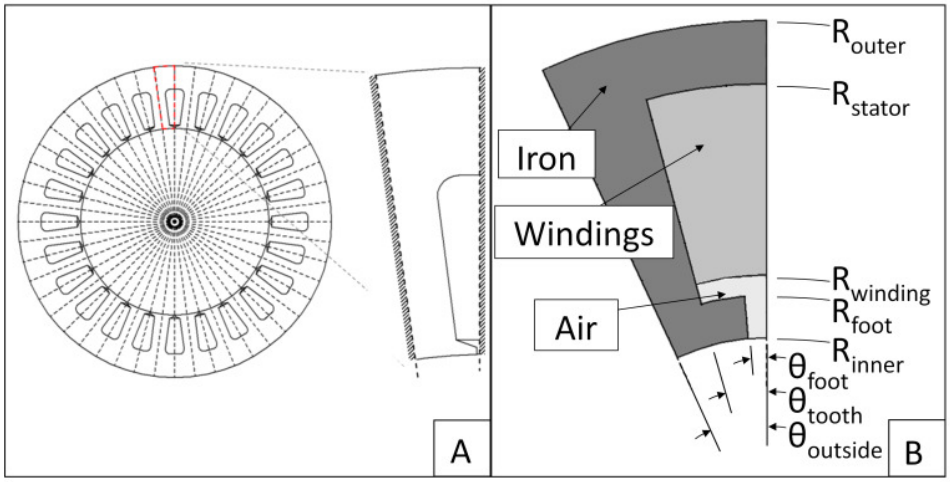

Figure 2.3 - Stator lines of symmetry and half slot model (A) and cylindrical description of the slot geometry (B)

2.4 Transformation of Slot Geometry

Many stator geometries have features that do not correspond to either a radius or an angle in cylindrical coordinates. An example of a conventional Type-1 Slot [33] design is presented in Figure 2.4A. Typical slot designs are not composed of purely radial and circumferential features. However, it is desirable to have a parametric cylindrical description of the slot geometry, as seen in Figure 2.4B, that would be applicable to several slot types because as previously stated the model is in R and θ. This was achieved by transforming the features of the actual slot to correspond to either a radius or angle. This application of the transformation technique is demonstrated here on slot type 1. The application of the transformation technique is demonstrated on slot type 3 in appendix A. The types 1 and 3 are the most common types.

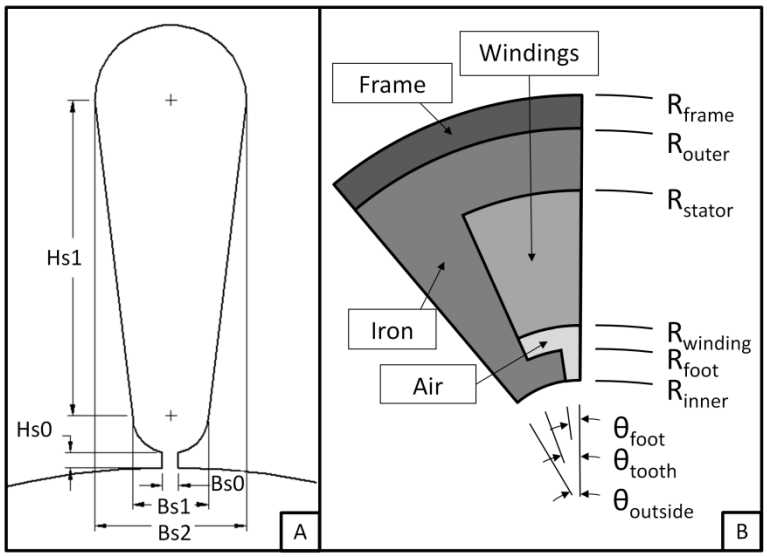

Figure 2.4 - Illustration of Slot Type 1 (A) and cylindrical description of the slot geometry (B)

The transformation of the actual slot geometry to the cylindrical coordinate representation begins with the calculation of the active winding area by (2.13) which is

the area of a trapezoid plus the area of the semicircle. Next, the area of the air below the windings is calculated as seen in (2.14). This area does not include the area between the pole shoes and is approximated by a semicircle.

$$A_{active} = \frac{Bs1 + Bs2}{2} \cdot Hs2 + \frac{\pi}{8} \cdot Bs2^2 \tag{2.13}$$

$$A_{air} = \frac{\pi}{8} \cdot Bs1^2 \tag{2.14}$$

The inner radius of the cylindrical coordinate representation is equal to the gap diameter over two as seen in (2.15).

$$R_{inner} = \frac{DiaSGap}{2} \tag{2.15}$$

The radius of the windings is calculated using (2.16).

$$R_{windings} = R_{inner} + Hs0 + \frac{Bs1}{2} \tag{2.16}$$

The middle radius is calculated as seen in (2.17) and is used to aid in the calculation of the angle of the tooth. This ensures the line that creates the radial sided tooth bisects the line that creates the parallel-sided tooth.

$$R_{middle} = R_{inner} + Hs0 + \frac{Bs1}{2} + \frac{Hs2}{2} \tag{2.17}$$

The angle of the tooth is then calculated using (2.18). Equation (2.18) was formulated by setting the arc length at the middle radius equal for both the radial and parallel-sided tooth.

$$\theta_{tooth} = \tan^{-1}\left(\frac{Bs1 + Bs2}{4 \cdot R_{middle}}\right) \tag{2.18}$$

The radius of the foot is calculated using the area of the air as seen in (2.19).

$$R_{foot} = \sqrt{R_{windings} - \frac{A_{air}}{\theta_{tooth}}} \tag{2.19}$$

The angle of the foot is calculated using (2.20) by setting the area between the pole shoes equal to each other in each case.

$$\theta_{foot} = \frac{Bs0 \cdot Hs0}{R_{foot}^2 - R_{inner}^2} \tag{2.20}$$

The radius of the stator is calculated using the active area and radius of the windings as seen in (2.21).

$$R_{stator} = \sqrt{R_{windings}^2 + \frac{A_{active}}{\theta_{tooth}}} \tag{2.21}$$

The outer radius is calculated in (2.22) using the diameter of the yoke. The outer angle is calculated in (2.23) using the number of slots.

$$R_{outer} = \frac{DiaSYoke}{2} \tag{2.22}$$

$$\theta_{outside} = \frac{\pi}{Nm} \tag{2.23}$$

The combined application of the adiabatic radial symmetric boundaries and the parametric description of the slot geometry result in a parametric, computationally efficient thermal model of an electric machine. The parametric thermal model could be numerically solved using an FEA package. However, utilizing an FEA package has two drawbacks. First, a bridging software that communicates between the FEA package and the optimization software would have to be written which increases computational time. Second, a license is required to use an FEA package that adds cost to the overall optimization software. To avoid these drawbacks, this work utilizes the finite difference

(FD) approach to numerically calculate the temperature distribution in the stator of an electric machine. This approach allows for integration of all physics into a single multi-physics code that maintains high computation speed, accuracy, and ease of use.

2.5 Steady State Parametric Finite Difference Thermal Model

The finite difference approach begins by writing an energy balance equation for each node that accounts for all energy entering, exiting, generated, and stored in the node. The general energy conservation equation is seen in (2.24). Only paths in the radial and tangential directions are considered as per the modeling assumptions. The energy that enters the node depends on the temperature and thermal resistance to the neighboring nodes.

$$\sum \dot{E}_{in} - \sum \dot{E}_{out} = -\dot{E}_{generated} \tag{2.24}$$

Figure 2.5 shows the thermal resistance network between the node and a neighboring node in the radial and tangential directions. The thermal resistance networks were constructed using conventional cylindrical thermal resistor network theory [34]. R_{tc} is the thermal contact resistance between the nodes. Contact resistance occurs when two free surfaces are in contact and create a finite temperature difference between the two surfaces. This formulation accounts for the possibility of neighboring nodes to have a different thermal conductivity than the node.

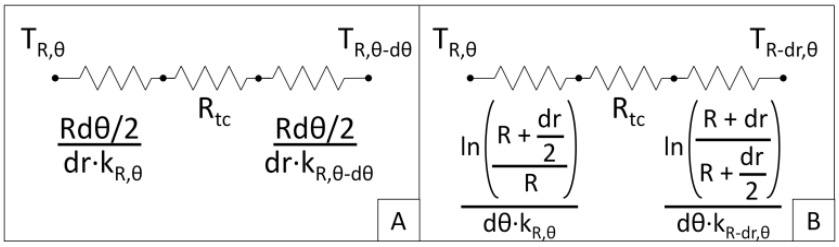

Figure 2.5 - Thermal resistance network (A) through the circumferential path, (B) through the radial path

The thermal resistance network shown in Figure 2.5 can be solved to find a total thermal resistance between nodes. The total thermal resistance relates to the energy entering/exiting the node through one direction as seen in (2.25).

$$\dot{E}_{in} = \frac{\Delta T_{R,\theta}}{R_{tot}} \tag{2.25}$$

The energy generated at the node can be from either copper loss or core loss as previously discussed.

Combining (2.24) and (2.25) with (2.2) and (2.3) leads to the steady state energy equation for a node as seen in (2.26). Each term on the left hand side of the equation represents energy contributions from neighboring nodes. The right hand side represents the energy generated at the node.

$$\frac{T_{R,\theta+d\theta} - T_{R,\theta}}{R_{tot-R,\theta+d\theta}} + \frac{T_{R,\theta-d\theta} - T_{R,\theta}}{R_{tot-R,\theta-d\theta}} + \frac{T_{R+dr,\theta} - T_{R,\theta}}{R_{tot-R+dr,\theta}} + \frac{T_{R-dr,\theta} - T_{R,\theta}}{R_{tot-R-dr,\theta}} = \dot{q}_{R,\theta} V_{R,\theta} \tag{2.26}$$

In (2.26), $T_{R,\theta+d\theta}$ is the temperature to the left of the node, $T_{R,\theta}$ is the temperature at the node, $R_{tot\text{-}R,\theta+d\theta}$ is the thermal conduction resistance between the nodes, $\dot{q}_{R,\theta}$ is the energy generated at the node per unit volume i.e. core losses or winding heating and $V_{R,\theta}$ is the volume of the node. The coefficients for the unknown temperatures and the constants are collected as seen in (2.27) for the steady state formulation.

$$\begin{aligned}\left(\frac{1}{\sum R_{tot}}\right) T_{R,\theta} &\frac{1}{R_{tot-R,\theta+d\theta}} T_{R,\theta+d\theta} + \frac{1}{R_{tot-R,\theta-d\theta}} T_{R,\theta-d\theta} \\ &+ \frac{1}{R_{tot-R+dr,\theta}} T_{R+dr,\theta} + \frac{1}{R_{tot-R-dr,\theta}} T_{R-dr,\theta} = C_{R,\theta}\end{aligned} \tag{2.27}$$

The governing energy balance equations for all the nodes lead to a system of linear equations as represented in (2.28). The coefficients of the unknown temperatures are

collected in a form of a tri-diagonal matrix represented in (2.28) by $\boldsymbol{R}$. The form of the tri-diagonal matrix has five diagonals, which is due to the 2-D representation of the finite difference. The temperatures can then be solved using matrix inversion.

$$\boldsymbol{R} \cdot \vec{T} = \vec{C} \tag{2.28}$$

2.6 Frame Thermal Resistance Model

A two dimensional approach simplifies the required computation. However, to maintain accuracy of the model, the three-dimensional thermal effects need to be captured. Specifically the model needs to account for heat transfer in the Z direction since this model is in R and θ. The most significant heat transfer in the Z direction takes place in the frame. Furthermore, the frame area of the machine is significantly larger than the active length area. This area needs to be accounted for in the boundary condition for the two dimensional model. A straight area multiplier would lead to over prediction of cooling capabilities because the temperature along the frame is not uniform. It is more accurate to describe the frame as a fin, which accounts for the temperature drop across the frame.

The heat flow through the frame of the machine is illustrated in Figure 2.6A. Notice that there are two heat flows, the first from the active length and the second into the end caps. The end caps can be represented as an extension to frame as seen in Figure 2.6B. This frame overhang from the active length can now be modeled as an annular fin and the temperature drop across this annular fin extension can be accounted for using classic fin theory as found in most general heat transfer texts [34].

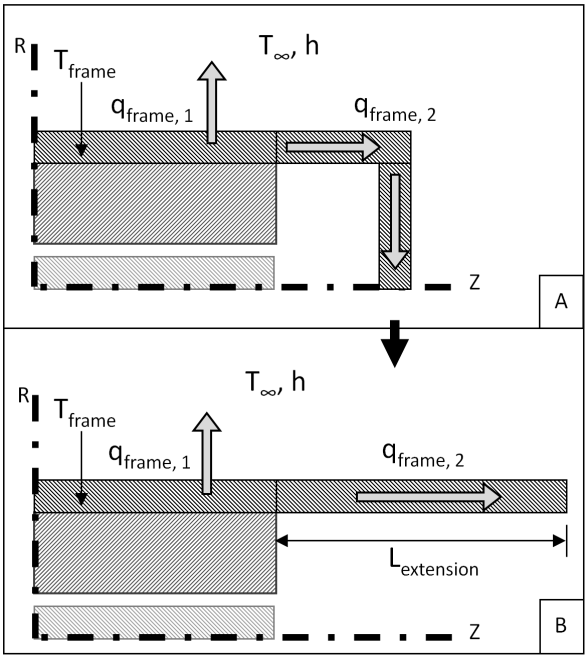

Figure 2.6 - Illustration of frame heat flow (A) and frame extension representation (B)

The heat flow through the frame can now be represented as a thermal circuit as seen in Figure 2.7. Notice that in Figure 2.7 the second heat flow has a fin efficiency associated with the frame extension. The efficiency accounts for the temperature drop along the length of the fin. Fin efficiency is calculated using standard analytical solutions found in most heat transfer texts. A fin with no temperature drop along its length would have an efficiency of one. The thermal circuit can then be solved and applied as a thermal resistance boundary condition thus accounting for the frame three-dimensional effects.

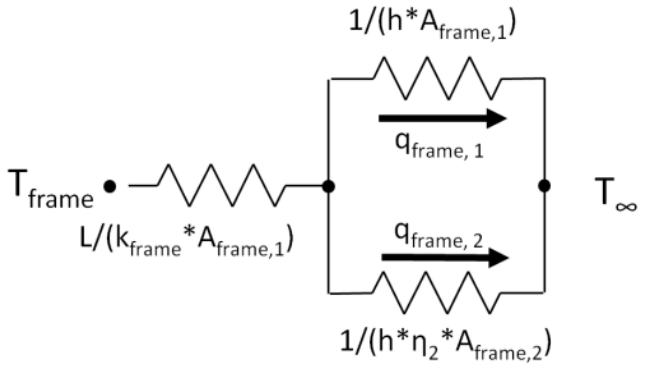

Figure 2.7 - Thermal circuit representation of frame

2.7 Parametric Self Segmenting Finite Difference Algorithm

An algorithm was written to implement the parametric half-slot stator model used to solve temperature distribution as seen in Figure 2.8. The algorithm begins with the user inputs of the nine geometric parameters, machine losses, ambient temperature, initial temperature, and boundary type. Using the geometric parameters the algorithm auto-generates and auto-segments the mesh.

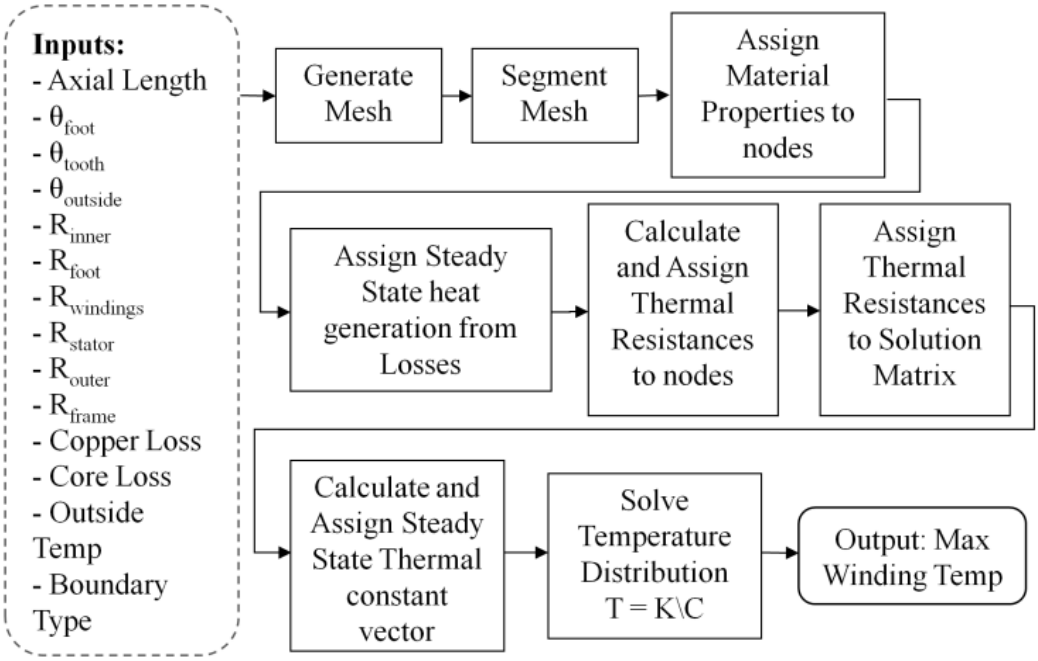

Figure 2.8 - Steady-state thermal algorithm flow chart

Mesh generation begins with the creation of vector arrays that store the node locations along the radial and circumferential directions. Four radial and three circumferential segment vector arrays are constructed to ensure that the boundary between material segments is accurately represented. To create the radial and circumferential segment vectors the step size dr and $d\theta$ must be calculated. Equation

(2.29) was formulated to ensure to that the middle of mesh has square elements, thus reducing the possibility of elongated elements. *dr* and *dθ* are defined by (2.30) and (2.31).

$$dr = d\theta \cdot \frac{R_f + R_i}{2} \tag{2.29}$$

$$d\theta = \frac{\theta_{outside}}{N_{approx,circumferential}} \tag{2.30}$$

$$dr = \frac{R_f - R_i}{N_{approx,radial}} \tag{2.31}$$

In (2.30), $N_{approx,circumferential}$ is the approximate number of elements in the circumferential direction and in (2.31) $N_{approx,radial}$ is the approximate number of elements in the radial direction. The number of nodes desired in the mesh is defined by the user as seen in (2.32).

$$N_{nodes,desired} = N_{approx,circumferential} \cdot N_{approx,radial} \tag{2.32}$$

Equations (2.29) - (2.32) can then be rearranged to calculated the approximate number of nodes in the circumferential direction based only on geometric inputs and the user defined number of nodes desired in the mesh as seen in (2.33). In (2.33) round is an operator that rounds the values to the nearest integer. Equation (2.32) can then be used to calculate the number of nodes in the radial direction. *dr* and *dθ* can thus be calculated from (2.30) and (2.31).

$$N_{approx,circumferential} = round\left(\sqrt{\frac{N_{nodes,desired}}{R_f - R_i} \cdot \theta_{outside} \cdot \frac{R_f - R_i}{2}}\right) \tag{2.33}$$

dr is used to calculate the number of elements in the first segment of the radial vector array as seen in (2.34). The number of elements in the first segment of the radial vector

array is used to calculate the step size for the first segment vector array that ensures the boundary between segments is accurately represented as seen in (2.35). The first radial segment vector array is seen in (2.36) which utilizes a center node distribution. This procedure is used to calculate the rest of the radial and circumferential segment vector arrays.

$$N_{radial,seg-1} = round\left(\frac{R_{o,seg-1} - R_{i,seg-1}}{dr}\right) \tag{2.34}$$

$$dr_{seg-1} = \frac{R_{o,seg-1} - R_{i,seg-1}}{N_{radial,seg-1}} \tag{2.35}$$

$$\vec{R}_{seg-1} = \left[R_{i,seg-1} + \frac{dr_{seg-1}}{2}, R_{i,seg-1} + \frac{3 \cdot dr_{seg-1}}{2}, R_{o,seg-1} - \frac{dr_{seg-1}}{2}\right] \tag{2.36}$$

The radial and circumferential segment vector arrays are concatenated to form the radial and circumferential vector arrays as seen in (2.37) and (2.38) respectively. The step sizes in the radial and circumferential directions associated with each segment are used to create step size vectors as seen in (2.39) and (2.40) respectively.

$$\vec{R} = \left[\vec{R}_{seg-1} \;\; \vec{R}_{seg-2} \;\; \vec{R}_{seg-3} \;\; \vec{R}_{seg-4} \;\; \vec{R}_{seg-5}\right] \tag{2.37}$$

$$\vec{\theta} = \left[\vec{\theta}_{seg-1} \;\; \vec{\theta}_{seg-2} \;\; \vec{\theta}_{seg-3}\right] \tag{2.38}$$

$$\overrightarrow{dr} = \left[\overrightarrow{dr}_{seg-1} \;\; \overrightarrow{dr}_{seg-2} \;\; \overrightarrow{dr}_{seg-3} \;\; \overrightarrow{dr}_{seg-4} \;\; \overrightarrow{dr}_{seg-5}\right] \tag{2.39}$$

$$\overrightarrow{d\theta} = \left[\overrightarrow{d\theta}_{seg-1} \;\; \overrightarrow{d\theta}_{seg-2} \;\; \overrightarrow{d\theta}_{seg-3}\right] \tag{2.40}$$

The actual number of nodes is then calculated by multiplying the number of elements in the radial and circumferential vector arrays. The actual number of nodes is used to

construct a node vector array that represents the node number for each node in the geometry as seen in (2.41).

$$\overrightarrow{Node} = \left[1, 2, 3, 4, \ldots N_{nodes,actual}\right] \tag{2.41}$$

The node vector array is then reshaped to create a mapping matrix as seen in the right side of Figure 2.9. This mapping matrix is the numerical representation of the location of the node numbers in the physical geometry. The linear indices of $\vec{R}$ and $\vec{\theta}$ correspond to the row-column subscripts of the mapping matrix.

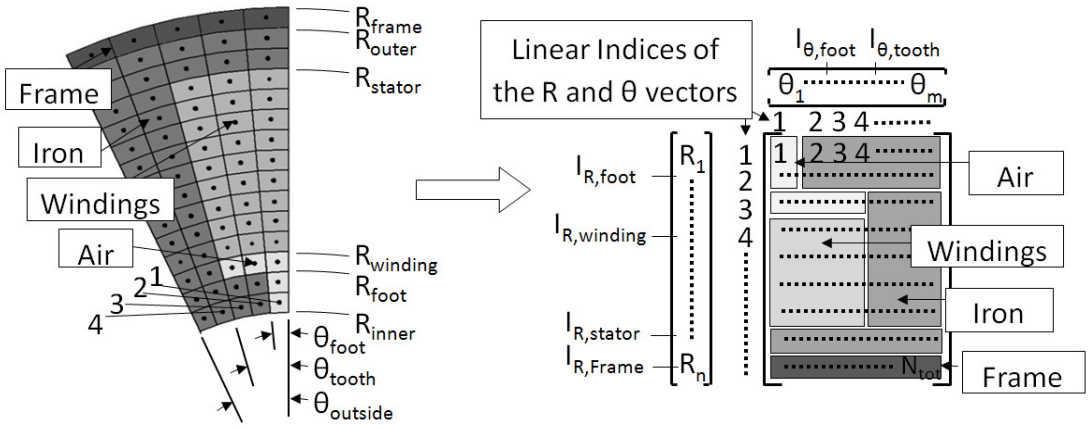

Figure 2.9 - Illustration of sector mesh segmentation

The algorithm then segments the mesh into the different material regions. Linear indices of the $\vec{R}$ and $\vec{\theta}$ vector arrays are found that correspond to the geometric features shown on the left hand side of Figure 2.9. The indices needed from the $\vec{R}$ vector are $I_{R,Foot}$, $I_{R,winding}$, $I_{R,stator}$, and $I_{R,frame}$. The indices needed from the $\vec{\theta}$ vector are $I_{\theta,Foot}$, $I_{\theta,tooth}$. These indices are used to extract material segment matrixes from the mapping matrix. Even though there are only three material segments in the actual geometry, there are six material segment matrixes as seen on the right side of Figure 2.9. The six material segment matrixes are needed because each matrix must be rectangular to facilitate matrix

algebra. The six material segment matrixes are then reshaped into vector arrays and concatenated to form three material segment vector arrays. The contents of the material segment vector arrays are the node numbers of the nodes within each material segment. The node numbers in the material segment vector arrays can then be used as indices for material property arrays. Each material property is stored in a separate array. In these arrays, the array index corresponds to a physical node number while the value at that index corresponds to the material property for that node number. This is done for the following properties: thermal conductivity and volumetric heat generation.

The contact resistance is accounted for by creating contact resistance vector array. The creation of the contact vector arrays begins with finding the node number of the nodes that have contact boundaries. These node numbers are found using the mapping matrix and the linear indices of the $\vec{R}$ and $\vec{\theta}$ utilizing the same technique as previously discussed. Once these node numbers are known contact resistance vector arrays can be constructed using the same procedure as described above.

The calculation of the diagonals in the tri-diagonal matrix begins with the calculation of the thermal resistances between nodes. Since the off diagonals in the tri-diagonal matrix are symmetric, only two thermal resistance vector arrays need to be calculated. The thermal resistances are calculated using the sum of the thermal resistance networks between nodes. To calculate the thermal resistance vector arrays, the radius at each node and the *dr* and *dθ* at each node and the node above need to be known. To create these vector arrays two matrices are created from the meshgrid between the $\vec{R}$ and $\vec{\theta}$ vectors and the $\overrightarrow{dr}$ and $\overrightarrow{d\theta}$ vectors. These matrices are similar to the mapping matrix in that the entries in the matrix correspond to the physical dimensions of the geometry and the row-

column indices correspond to the linear indices in the $\vec{R}$ and $\vec{\theta}$ vectors. Vector arrays containing the radius at each node and the *dr* and *dθ* at each node and the node above are then extracted from these matrices using the index technique. Vector array math is then used to calculate the thermal resistance vector for the nodes above. The same technique is used to calculate the thermal resistance for the nodes to the left.

The thermal resistance vector arrays are then placed into a sparse matrix in the off diagonal positions. The main diagonal in calculated by summing the rows of the sparse matrix to create a sum resistance vector array. The boundary condition vector array is added to the sum resistance vector array to create the main diagonal. Once the main diagonal in calculated it is placed in the sparse matrix. The steady-state solution in calculated using the Matlab function left matrix division between the sparse thermal resistance matrix and the constant vector array.

2.8 Mesh Convergence Study

A convergence study was performed to determine the number of nodes required to minimize numerical errors associated with mesh size. The convergence study involved comparing course mesh solutions with an ultra-fine mesh solution containing two million nodes. The course mesh solutions were compared to the ultra-fine mesh solution using a nearest interpolation method. The difference between the course mesh and the ultra-fine mesh temperatures were averaged to determine convergence error. The course mesh solutions were obtained from 1,000 to 200,000 nodes in increments of 1,000. Four cases were investigated as summarized in Table 2.1. The cases were selected based on the smallest and largest electric machine size and number of teeth expected to be designed with the FD parametric design tool. The copper loss and core loss were manually

manipulated to maximize the temperature gradient in the windings without exceeding a thermal limit of 150°C. Larger temperature gradients require finer meshes to capture the thermal effects. Maximizing the temperature gradient in this study creates a worst-case scenario.

Table 2.1 - Losses and geometries simulated in mesh convergence case study

	Case 1	Case 2	Case 3	Case 4
Copper Loss [W]	350	2400	370	3000
Core Loss [W]	100	500	120	750
$R_{foor,inner}$ [mm]	30	100	100	200
$R_{stator,outer}$ [mm]	50	150	120	250
Number of Teeth	6	36	6	36

The three angles in the half slot model were formulated as a function of the number of teeth as shown in (2.42), (2.43), and (2.44). The angles were formulated to break the geometry into thirds in the theta direction.

$$\theta_{outer} = \frac{2\pi}{N_{slots}} \tag{2.42}$$

$$\theta_{foot} = \frac{\theta_{outer}}{3} \tag{2.43}$$

$$\theta_{tooth} = \frac{2 \cdot \theta_{outer}}{3} \tag{2.44}$$

The three other radial geometric parameters that define the half slot model were formulated as functions of the inner radius of the foot, $R_{foor,inner}$, and outer radius of the stator, $R_{stator,outer}$ as displayed in (2.45), (2.46), and (2.47). In (2.47), the thickness of the stator yoke was set to 20% of the total stator thickness.

$$R_{foot,outer} = R_{foot,inner} + 1 \tag{2.45}$$

$$R_{windings} = R_{foot,inner} + 3 \tag{2.46}$$

$$R_{stator,inner} = R_{stator,outer} - 0.2\left(R_{stator,outer} - R_{foot,inner}\right) \tag{2.47}$$

The results from the mesh convergence study are presented in Figure 2.10. Notice that the convergence error decreases with increasing number of nodes as expected. The computation time increases linearly with increasing number of nodes as expected. The temperature plots for each case illustrates the large temperature gradients in the windings confirming a worst-case scenario. The convergence error for all four cases is below 0.5°C at 100,000 nodes. This error tolerance is consistent with the absolute error of high precision T-type thermocouples. The computational time at 100,000 nodes is 1.1s, thus 100,000 nodes was selected as a reasonable number of nodes for the thermal simulations.

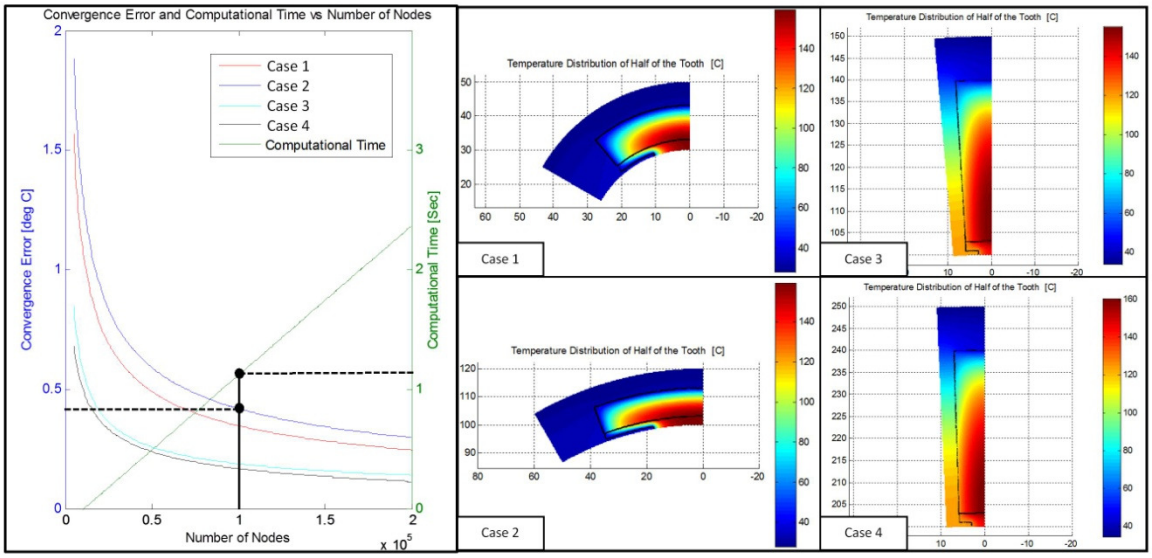

Figure 2.10 - Convergence error and computational time versus nodes of numbers for the mesh convergence study (left). Temperature plots at 100,000 nodes for each of the cases (right).

2.9 Modeling Approach Verification

Two verification studies were preformed that compared the FD model with FEA. The machine that was simulated had an air gap diameter of 115.8 mm, a stator diameter of 200 mm, and active length of 80 mm, and an overall length of 167 mm. The frame on the simulated machine was made of aluminum with a thickness of 10 mm. 100,000 nodes were used in the FD parametric model which equates to a nominal radial element size, *dr*, of 100 μm. To ensure a fair comparison a node size of 100 μm was used in the FEA analysis.

The first study was the slot modeling verification study. This study was preformed to validate the FD model was producing correct results when compared a FEA of the transformed slot model. This study also verified the validity of the slot transformation technique. The second study was preformed to verify the 2-D frame modeling technique was accurate when compared to a 3-D FEA.

Table 2.2 shows the thermal properties used in the simulations. The material for the backiron was Hiperco 50. The core loss was calculated with a 60hz frequency, the weight of the material, and an average flux density of 1T [35]. The thermal conductivity for these materials was found from [36]. The winding effective thermal conductivity was found in [37]. The heat transfer coefficients were calculated using the correlations from (10) and (12).

Table 2.2 - Thermal properties and loads for the simulation

Property	Unit	Value
$k_{backiron}$	W/m-K	29.8
$k_{winding}$	W/m-K	1
k_{frame}	W/m-K	170
k_{air}	W/m-K	0.03
$h_{natural}$	W/m^2-K	6.55
h_{forced}	W/m^2-K	61.1
Core loss	W	21.5
T_{inf}	C	22

The cases that were simulated in each study are presented in Table 2.3. The cases were a combination of convective boundary conditions, current densities, and slot types. The convective boundary conditions investigated are natural and forced. The current densities investigated are typical values used for the respective convective boundary condition type.

Table 2.3 - Cases simulated in study

Case Number	Convective Boundary Condition	Current Density [A/mm^2]	Slot Type
1	Natural	4	1
2	Natural	4	3
3	Natural	6	1
4	Natural	6	3
5	Forced	8	1
6	Forced	8	3
7	Forced	12	1
8	Forced	12	3

The slot geometries used in the verification studies are illustrated in Figure 2.11. Figure 2.11A is commonly known as slot type 1. This stator geometry has 24 slots. Figure 2.11B is similar to slot type 3, but is an advanced design from a traction drive and has 12 slots.

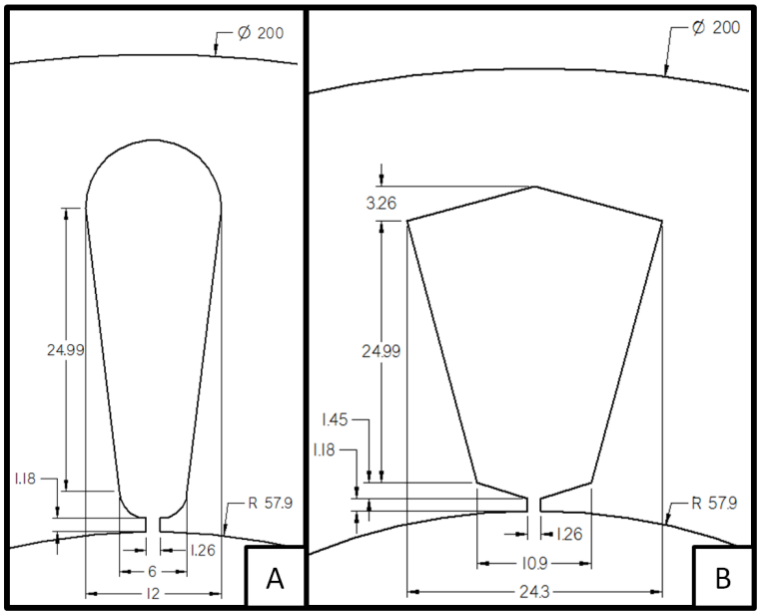

Figure 2.11 - Slot geometries simulated in this study

2.9.1 Slot Modeling Approach Verification

The results for the eights cases for the slot verification study is presented in Table 2.4. Notice that the FD model and the FEA of the transformed slot are the same. Also, notice that the maximum difference between the actual slot FEA and the FD model is 1.5%. The results from the case eight in this study are presented in Figure 2.12. The results from the FD model are presented in Figure 2.12A, the results from the FEA of the transformed slot are presented in Figure 2.12B, and the results from the FEA of the actual slot are presented in Figure 2.12C.

Table 2.4 - Results for slot modeling approach verification study

Case Number	FEA Max Temp °C (actual)	FEA Max Temp °C (trans)	FD Max Temp °C	Percentage Difference
1	309.2	308.8	308.8	-0.1%
2	316.9	313.1	313.1	-1.2%
3	593.1	592.6	592.6	-0.1%
4	611.2	602.2	602.2	-1.5%
5	138.9	138.6	138.6	-0.2%
6	157.95	156.7	156.7	-0.8%
7	276.7	275.8	275.8	-0.3%
8	319.51	316.7	316.7	-0.9%

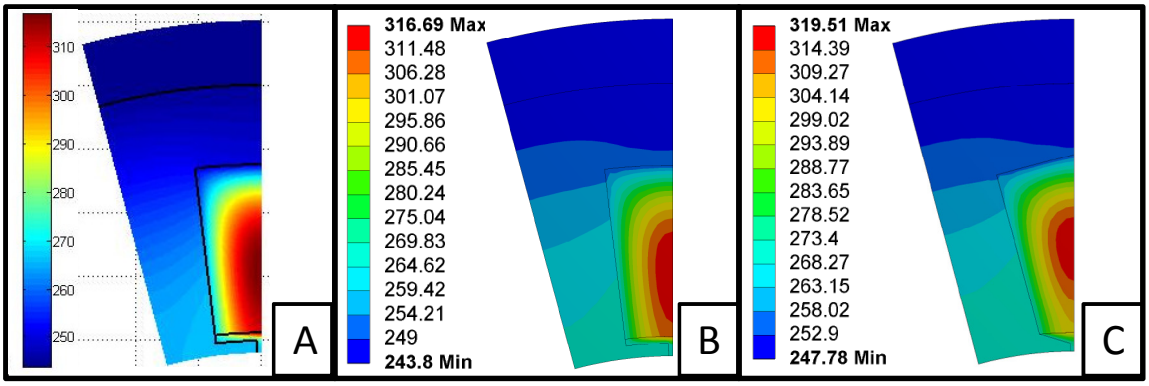

Figure 2.12 - Temperature distribution for case 8 from finite difference (A), FEA of transformed tooth (B), and FEA of actual tooth (C)

2.9.2 Frame Modeling Approach Verification

The results from the frame modeling verification study are presented in Table 2.5. Notice that the FD model was within 5% in all cases. The results from case eight are presented in Figure 2.13. The results from the FD model are presented in Figure 2.13A, the isometric view of the 3-D FEA is presented in Figure 2.13B, and the midplane results of the 3-D FEA are presented in Figure 2.13C.

Table 2.5 - Results for frame modeling approach verification study

Case Number	FEA Max Temp °C	FD Max Temp °C	Percentage Difference
1	108.72	113.19	4.1%
2	114.05	118.47	3.9%
3	194.84	203.76	4.6%
4	207.03	215.49	4.1%
5	69.29	70.09	1.2%
6	87.17	88.62	1.7%
7	125.41	127.05	1.3%
8	165.68	168.81	1.9%

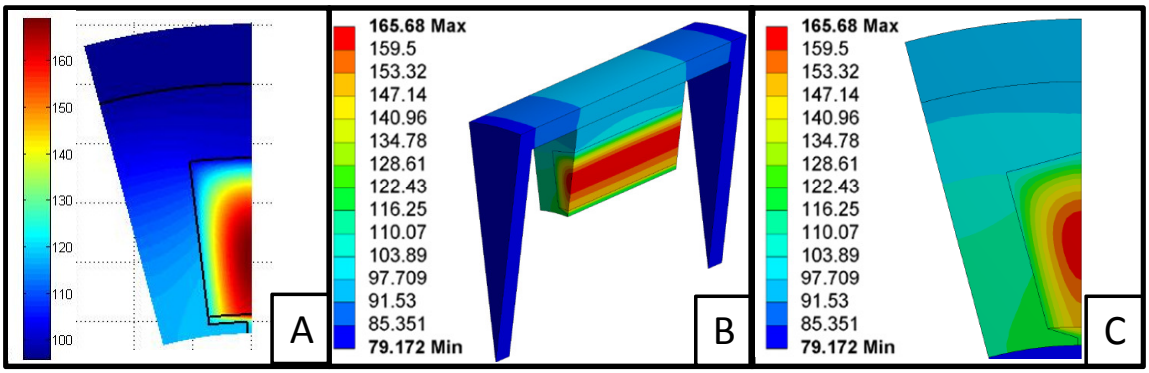

Figure 2.13 - Temperature distribution results for case 8 from finite difference (A) and 3-D FEA (B&C)

2.10 Discussion

In the slot verification case study, the temperature results were significantly higher than in the frame verification study for the same cases. This is because in the slot modeling approach verification study the model only accounted for the active length. In actuality, the frame length is larger than the active length. The frame length as well as the end-cap area dissipates a significant portion of the heat. This area was not accounted for in the slot modeling approach verification study leading to the significantly higher temperatures.

In the frame modeling approach verification study, the results showed that the forced convection cases were more accurate than the natural convection cases. This is because the frame modeling approach is applied to the exterior of the frames nodes. This assumes that heat travels better in the radial direction rather than through the length of the frame. This assumption is valid for the forced cases, but is not a perfect description in the natural cases. Also in all cases the FD model over predicted the temperatures when compared to the FEA. This indicates the frame modeling approach is a conservative estimate of the frame cooling capacity when compared to the 3-D FEA. However, the accuracy is within 4.6%, which is acceptable for a design tool.

2.11 Summary

This chapter has presented a steady-state parametric thermal model of a permanent magnet electric machine. This model has been implemented using a finite difference approach. The thermal model includes a slot transformation technique that transforms typical slot geometries into polar coordinates for computational efficiency. This technique was validated to within 2% of high-fidelity FEA thermal analysis of the actual slot geometries. In addition, the thermal model includes frame modeling technique that accounts for the three-dimensional conduction within the frame. Similarly, this technique was validated to within 5% error as compared to a three-dimensional FEA of an electric machine.

CHAPTER 3

TRANSIENT PARAMETRIC THERMAL MODELING OF ELECTRIC MACHINES

3.1 Introduction

This chapter presents a transient parametric thermal model of an electric machine that is able to consider time varying speeds and loads. The thermal model has been implemented using a finite difference (FD) approach. This work develops a frame capacitance model and verifies it to within 5% accuracy for the quasi-transient cases and 6.5% accuracy for the fully-transient cases. The proposed algorithm is able to solve a 100,000 node transient temperature with 50 time steps in 41.5s, resulting in significant gains in computational speed over widely adopted finite element analysis (FEA) approaches. This fast-solving parametric model enables closed loop machine design once integrated with an electromagnetic model with the ability to consider time varying loads.

3.2 Review of Salient Literature

The thermal circuits approach was initially presented by Mellor et al in 1991 [7]. Importantly, this original study noted that some resistances could not be directly calculated and must be experimentally measured and applied to the model. Thermal circuit models were extended towards transient problems by adding thermal capacitors at each node. Valenzuela et al. simplified the transient thermal circuit network to a first-order model and a second-order model [12]. The first-order model contained one loss source, one thermal resistance, and one thermal capacitor. During experimentation, the authors found that the time constant of the motor varied with load conditions and concluded that a calibrated first-order model was not sufficient to accurately model the

transient thermal transport. The authors then presented a calibrated second-order model, which contained three loss sources, two thermal resistances, and two thermal capacitors. The authors concluded that the calibrated second-order model works well for predicting the transient thermal response of an induction machine. Kral et al. found that a calibrated first-order thermal circuit model was within 10°C for three test machines for constant loading conditions [19]. Other authors have found that larger thermal circuit model containing 11 nodes can accurately predict transient thermal response when calibrated [13, 14, 38]. Thermal circuit approaches have the advantage of being fast to solve, but suffer from the need for experimental fitting of the thermal resistance parameters. The calibration required for the thermal circuit models of electric machines limits this modeling approach to a predictive model rather than a parametric design tool. Consequently, there has been significant interest in using physics-based FEA tools that do not rely on experimental data to model thermal transport in electric machines.

The first work in which FEM was used to evaluate the temperature distribution in electric machines was done in 1980 by Armor[28]. This work involved a 3-D thermal simulation of a turbine generator rotor. FEM has shown to give accurate predictions of temperature in electric machines [29, 30]. In recent years, FEM has been compared to thermal circuits and used to calibrate thermal circuits [6, 10, 24]. CFD has mostly been used to evaluate heat transfer coefficients for use in thermal circuits in lieu of well known heat transfer correlations [6, 15, 31]. Liao et al has used CFD to solve the temperature distribution in an induction machine [32]. Both FEA and CFD are generic, but typically have long setup up and computational times associated with them, which limit their use as design tools. This works presents a numerical FEA verification of a parametric thermal

model of an electric machine [39] that does not require experimental calibration. This thermal model can be incorporated with electromagnetic design to produce an integrated design tool that can be used for closed loop design of electric machines while considering time varying loads.

3.3 Thermal Modeling of Electric Machines

The basics concepts for thermal modeling of electric machines were detailed in chapter 2. However, when transient cases are considered there are some notable changes to thermal modeling. The transient heat diffusion equation in cylindrical coordinates which governs the transient temperature distribution within a cylindrical geometry [34] is presented in (3.1).

$$\frac{1}{r}\frac{\partial}{\partial r}\left(kr\frac{\partial T}{\partial r}\right)+\frac{1}{r^2}\frac{\partial}{\partial \theta}\left(k\frac{\partial T}{\partial \theta}\right)+\frac{\partial}{\partial z}\left(k\frac{\partial T}{\partial z}\right)+\dot{E}(t)=\rho C\frac{\partial T}{\partial t} \tag{3.1}$$

In (3.1), $\dot{E}(t)$ is the heat generated per unit volume as a function of time. In a typical thermal electric machine model, the only heat losses that are considered are the core and copper loss, because the other losses are much smaller in magnitude. The heat generated by the windings and the iron are defined by (3.2) and (3.3) respectively.

$$\dot{E}(t)_{copper}=\frac{I(t)^2\cdot R}{V_{windings}} \tag{3.2}$$

$$\dot{E}(t)_{iron}=\frac{\dot{E}(t)_{core\ loss}}{V_{iron}} \tag{3.3}$$

In (3.2), *I(t)* is the single phase RMS current as a function of time, *R* is the total phase resistance of the windings, $V_{windings}$ is total volume of the windings including the end-windings. In (3.3), $\dot{E}(t)_{core\ loss}$ is the core loss which is estimated from an electromagnetic

simulation as a function of time and V_{iron} is the total volume of the stator. As in chapter 2, this formulation of the heat generated assumes that the copper and core loss are evenly distributed through their respective volumes, which in most cases is a fair assumption.

The definition between quasi and transient thermal response has been detailed in chapter 1. Those definitions are used here in the parametric transient thermal model of electric machines. Furthermore, the geometric simplifications and slot modeling technique detailed in chapter 2 are used to simplify used in this model as well. This model is then implemented using a two dimensional finite difference technique as detailed in the next section.

3.4 Transient Parametric FD Thermal Model

The finite difference approach begins by writing an energy balance equation for each node that accounts for all energy entering, exiting, generated, and stored in the node. The general energy conservation equation is seen in (3.4). Only paths in the radial and tangential directions are considered as per the modeling assumptions. The energy that enters the node depends on the temperature and thermal resistance to the neighboring nodes.

$$\sum \dot{E}_{in} - \sum \dot{E}_{out} = \dot{E}_{stored} - \dot{E}_{generated} \tag{3.4}$$

Figure 3.1 shows the thermal resistance network between the node and a neighboring node in the radial and tangential directions. The thermal resistance networks were constructed using conventional cylindrical thermal resistor network theory [34]. R_{tc} is the thermal contact resistance between the nodes. Contact resistance occurs when two free surfaces are in contact and create a finite temperature difference between the two

surfaces. This formulation accounts for the possibility of neighboring nodes to have a different thermal conductivity than the node.

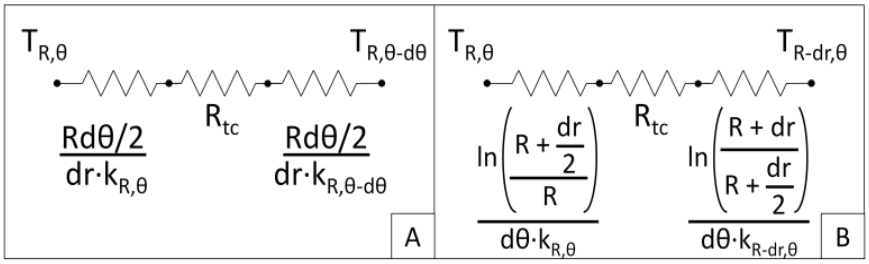

Figure 3.1 - Thermal resistance network (A) through the circumferential path, (B) through the radial path

The thermal resistance network shown in Figure 3.1 can be solved to find a total thermal resistance between nodes. The total thermal resistance relates to the energy entering/exiting the node through one direction as seen in (3.5).

$$\dot{E}_{in} = \frac{\Delta T_{R,\theta}}{R_{tot}} \tag{3.5}$$

The energy generated at the node can be either from copper loss or core loss as previously defined. In finite difference, the partial derivative of temperature with respect to time can be approximated as the difference of the future temperature and current temperature over the time step.

$$\dot{E}_{stored} = \rho CV\big|_{R,\theta} \frac{\partial T}{\partial t} \approx \rho CV\big|_{R,\theta} \frac{T_{R,\theta}^{t+1} - T_{R,\theta}^{t}}{\Delta t} \tag{3.6}$$

In (3.6), ρ is the density at the node, C is the specific heat at node (R,θ), Δt is the time step, $T_{R,\theta}^{t}$ is the current temperature at the node, and $T_{R,\theta}^{t+1}$ is the unknown temperature at the next time step. Combining (3.4), (3.5),& (3.6) with (3.2) & (3.3) leads to the implicit transient energy balance equation for a node as seen in (3.7). Each term on the left hand side of the equation represents energy contributions from neighboring nodes.

The right hand side represents the energy stored at the node less the energy generated at the node. The expected time constant for this system is approximately several minutes to hours. An explicit method requires the selection of a time step that leads to convergence whereas an implicit method guarantees convergence for any time step. An explicit method has a faster computation at each time step, but the increased number of times steps required for convergence overshadows this benefit. The implicit method was chosen due to this expected time benefit and guarantee of convergence.

$$\frac{T_{R,\theta+d\theta}^{t+1}-T_{R,\theta}^{t+1}}{R_{tot-R,\theta+d\theta}}+\frac{T_{R,\theta-d\theta}^{t+1}-T_{R,\theta}^{t+1}}{R_{tot-R,\theta-d\theta}}+\frac{T_{R+dr,\theta}^{t+1}-T_{R,\theta}^{t+1}}{R_{tot-R+dr,\theta}}+\frac{T_{R-dr,\theta}^{t+1}-T_{R,\theta}^{t+1}}{R_{tot-R-dr,\theta}}= \rho CV\big|_{R,\theta}\frac{T_{R,\theta}^{t+1}-T_{R,\theta}^{t}}{\Delta t}-\dot{q}_{R,\theta}^{t}V_{R,\theta} \tag{3.7}$$

In (3.7), $T_{R,\theta+d\theta}$ is the temperature to the left of the node, $T_{R,\theta}$ is the temperature at the node, $R_{tot\text{-}R,\theta+d\theta}$ is the thermal conduction resistance between the nodes, $\dot{q}_{R,\theta}^{t}$ is the energy generated at the node per unit volume i.e. core losses or winding heating and $V_{R,\theta}$ is the volume of the node. The coefficients for the unknown temperatures and the constants are collected as seen in (3.8) for the transient formulation.

$$\left(\frac{1}{\sum R_{tot}}-\frac{\rho CV\big|_{R,\theta}}{\Delta t}\right)T_{R,\theta}^{t+1}+\frac{1}{R_{tot-R,\theta+d\theta}}T_{R,\theta+d\theta}^{t+1}+\frac{1}{R_{tot-R,\theta-d\theta}}T_{R,\theta-d\theta}^{t+1} +\frac{1}{R_{tot-R+dr,\theta}}T_{R+dr,\theta}^{t+1}+\frac{1}{R_{tot-R-dr,\theta}}T_{R-dr,\theta}^{t+1}=C_{R,\theta}^{t} \tag{3.8}$$

The governing energy balance equations for all the nodes lead to a system of linear equations as represented in (3.9). The coefficients of the unknown temperatures are collected in a form of a tri-diagonal matrix represented in (3.9) by ***R***. The form of the tri-diagonal matrix has five diagonals, which is due to the 2-D representation of the finite difference. The temperatures can then be solved using matrix inversion at each time step.

$$\boldsymbol{R} \cdot \vec{T}^{t+1} = \vec{C}^{t} \tag{3.9}$$

3.5 Frame thermal Capacitance

This thermal model uses a two dimensional approach which simplifies the required computation. However, to maintain accuracy of the model, the three-dimensional thermal effects need to be captured. Specifically, the two-dimensional model only accounts for the active length of the electric machine. However, there is significant thermal capacitance in the frame of the machine. Thermal capacitance is the ability to absorb thermal energy and slow the temperature rise within the machine. Figure 3.2 illustrates a machine in the R and Z coordinates.

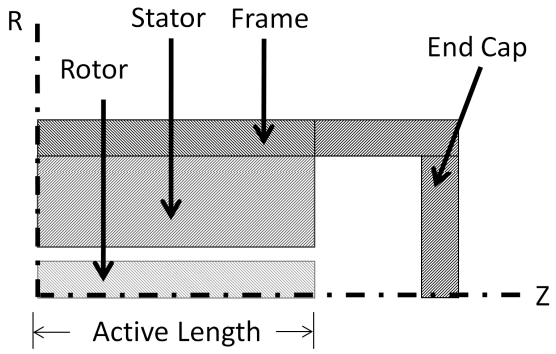

Figure 3.2 - Illustration of frame capacitance modeling

To account for the frame capacitance beyond the active length the density of the frame in the finite difference simulation must be augmented as seen in (3.10). In (3.10) $m_{tot,frame}$ is the total mass of the frame and $V_{frame,\ active\ length}$ is the volume of the frame in the active length.

$$\hat{\rho}_{frame} = \frac{m_{tot,\,frame}}{V_{frame,\,active\ length}} \tag{3.10}$$

3.6 Parametric Self-Segmenting Transient FD Algorithm

An algorithm was written to implement the parametric half slot transient thermal model as seen in Figure 3.3. The algorithm begins with the user inputs of the nine geometric parameters, machine losses, ambient temperature, initial temperature, boundary type, and transient load cycle. The algorithm uses the geometric parameters to generate and segment the mesh. The segmented mesh is then assigned thermal materials properties to each node. The algorithm creates a vector of transient losses based on the user defined transient load cycle. The thermal resistance between nodes is calculated based on the segmented mesh and assigned to a form of a tridiagonal matrix. The algorithm then calculates the transient temperature distribution for one transient load cycle using and iterative solution of the linear system of equations. If the solution type is quasi transient the simulation ends and the algorithm outputs the maximum winding temperature. If the solution is fully-transient, the algorithm continues to simulate transient load cycles until a quasi steady state transient temperature distribution or the iteration limit is reached. The algorithm then outputs the maximum winding temperature during the final transient load cycle.

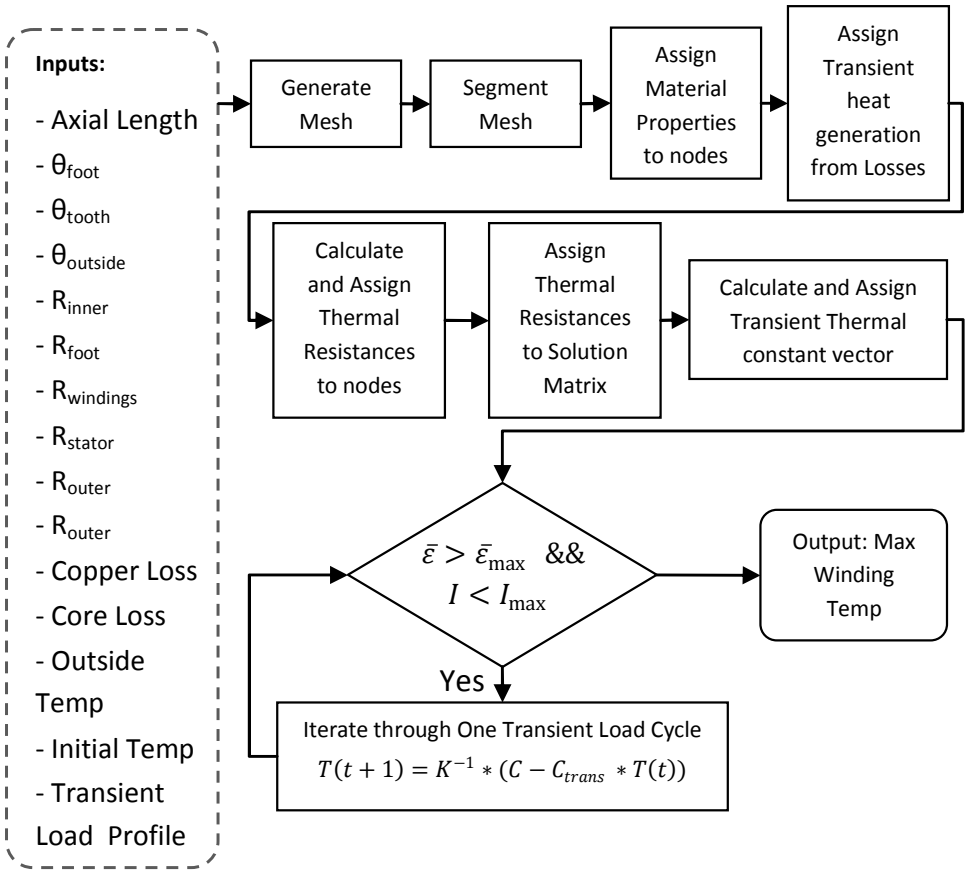

Figure 3.3 - Transient algorithm flowchart

3.7 Thermal Modeling Approach Verification

3.7.1 Verification Study Approach

Two verification studies were preformed that compared the FD model with FEA. The same machine from Chapter 2 was used in this verification study. The dimensions of the machines are repeated here for completeness. The machine that was simulated had an air gap diameter of 115.8 mm, a stator diameter of 200 mm, and active length of 80 mm, and an overall length of 167 mm. The frame on the simulated machine was made of aluminum with a thickness of 10mm. The first study focused on the frame capacitance modeling verification only. This study was preformed to validate the FD model was producing correct results when compared a FEA under a quasi-transient simulation. This

study also verified the validity of the frame capacitance modeling technique. The second study was preformed to verify the FD fully-transient simulation as compared to FEA.

Table 3.1 - Thermal properties and loads for the simulation

Property	Value	Unit
$k_{backiron}$	29.8	W/m-K
$\rho_{backiron}$	7874	kg/m^3
$Cp_{backiron}$	449	J/kg-K
$k_{winding}$	1	W/m-K
$\rho_{winding}$	2710.5	kg/m^3
$Cp_{winding}$	900	J/kg-K
k_{frame}	170	W/m-K
ρ_{frame}	2700	kg/m^3
Cp_{frame}	896	J/kg-K
k_{air}	0.03	W/m-K
ρ_{air}	1	kg/m^3
Cp_{air}	1009	J/kg-K
$h_{natural}$	6.55	W/m^2-K
h_{forced}	61.1	W/m^2-K
Core loss	21.5	W

The thermal properties used in the simulations are presented in Table 3.1. The assumed material for the backiron was Hiperco 50. The core loss was calculated with a 60hz frequency, the weight of the material, and an average flux density of 1T [35]. The frame was aluminum. The thermal conductivity, specific heats, and densities for these materials was found from [36]. The winding effective thermal conductivity was found in [37]. The heat transfer coefficients were calculated using the correlations from [34] for a horizontal cylinder under natural convection and forced convection.

The cases that were simulated in the quasi-transient study are presented in Table 3.2. The cases were a combination of convective boundary conditions, current densities, and slot types. The convective boundary conditions to be investigated are natural and

forced. The current densities to be investigated are typical values used for the respective convective boundary condition type.

Table 3.2 - Cases simulated in frame modeling study

Case	Convective Boundary Condition	Current Density [A/mm^2]	Slot Type
1	Natural	4	1
2	Natural	4	3
3	Natural	6	1
4	Natural	6	3
5	Forced	8	1
6	Forced	8	3
7	Forced	12	1
8	Forced	12	3

The cases that were simulated in the fully-transient study are presented Table 3.3. The cases involved two duty cycles, convective boundary types, and two slot types. The duty cycles refer to the copper loss varying with time. The current densities were selected to be the maximum from the previous study for each respective convective boundary.

Table 3.3 - Cases simulated in fully-transient verification

Case	Duty Cycle	Current Density [A/mm^2]	Convective Boundary Condition	Slot Type	Cycle time [min]
1	50	6	Natural	1	200
2	50	6	Natural	3	200
3	75	6	Natural	1	20
4	75	6	Natural	3	20
5	50	12	Forced	1	200
6	50	12	Forced	3	200
7	75	12	Forced	1	20
8	75	12	Forced	3	20

The slot geometries used in the verification studies are illustrated in Figure 3.4. These geometries are the same as in the previous chapter and are presented here for completeness.

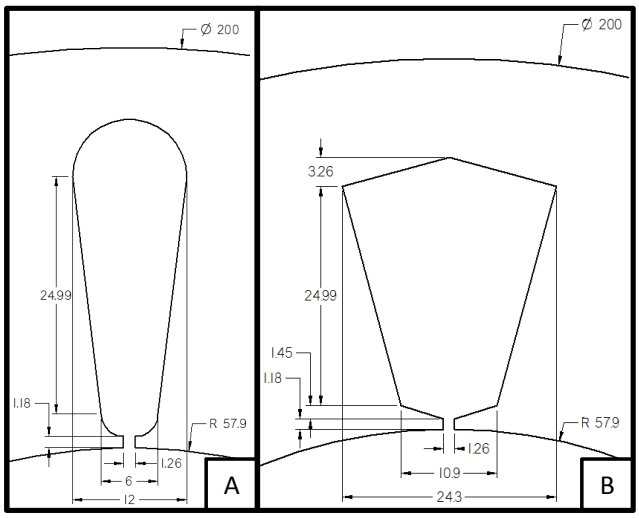

Figure 3.4 - Slot geometries simulated in this study

3.7.1 Quasi - Transient Verification

The results from the quasi-transient verification studies are presented in Table 3.4. Notice that in each case the final percentage difference between the FD and FEA is less than 5%. This percentage difference is taken from the maximum winding temperature seen in each simulation. Also, notice that in each case the average temperature difference is less than 10°C. This average difference is maximum winding temperature difference between the FD and FEA at the end of the simulation. The results from case 4 and case 8 for the quasi-transient study are presented in Figure 3.5 and Figure 3.6 respectively. These plots show the maximum winding temperature from the FD and FEA as a function of time. In all cases the FD over predicts the maximum temperature of windings.

Table 3.4 - Frame capacitance modeling verification results

Case	Convective Boundary Condition	FEA Max Temp [C]	FD Max Temp [C]	Final Percent Diff.	Avg. Diff. [C]
1	Natural	108.4	113.9	4.83%	4.80
2	Natural	113.8	118.3	3.80%	3.92
3	Natural	194.84	205.1	5.00%	9.58
4	Natural	206.6	215.1	3.95%	7.50
5	Forced	69.19	70.04	1.21%	0.44
6	Forced	87.11	88.53	1.60%	0.70
7	Forced	125.1	127.5	1.88%	1.12
8	Forced	165.5	168.6	1.84%	1.48

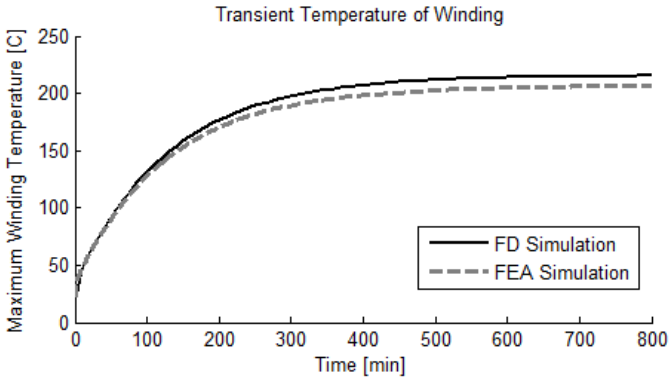

Figure 3.5 - Results from case 4 of frame capacitance modeling verification study

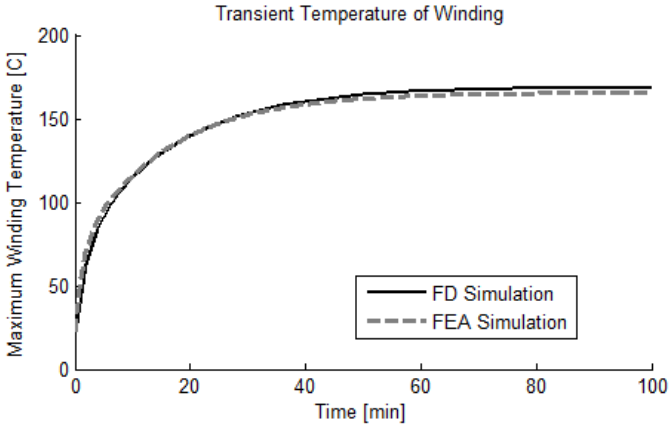

Figure 3.6 - Results from case 8 of frame capacitance modeling verification study

3.7.2 Fully - Transient Verification

The results from the fully-transient verification studies are presented in Table 3.5. Notice that in each case the final percentage difference between the FD and FEA is less than 7%. This percentage difference is taken from the maximum winding temperature seen in each simulation. Also, notice that in each case the average temperature difference is less than 8°C. This average difference is the maximum winding temperature difference between the FD and FEA at the highest point. The results from case 4 and case 8 for the fully-transient study are presented in Figure 3.7 and Figure 3.8 respectively. These plots show the maximum winding temperature from the FD and FEA as a function of time. The second portion of the each plot shows the load cycles that were being simulated. In both cases, a 75% duty cycle of copper loss was being simulated. In all cases the FD over predicts the maximum temperature of windings.

Table 3.5 - Fully-transient verification results

Case	Convective Boundary Condition	FEA Max Temp [C]	FD Max Temp [C]	Final Percent Diff.	Avg. Diff. [C]
1	Natural	145.5	155.4	6.37%	4.90
2	Natural	156	163.9	4.82%	3.84
3	Natural	174.5	184.7	5.52%	7.25
4	Natural	186.1	194.3	4.22%	5.69
5	Forced	95.9	96.9	1.03%	-0.24
6	Forced	132.6	134.8	1.63%	0.38
7	Forced	112.7	114.5	1.57%	0.26
8	Forced	151.5	154.2	1.75%	0.99

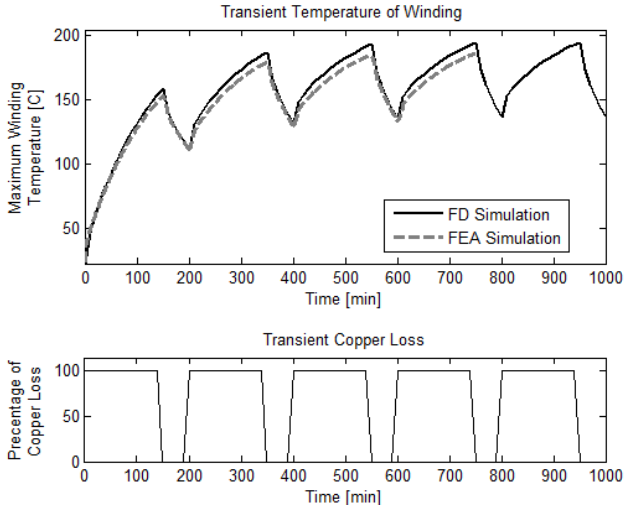

Figure 3.7 - Results from case 4 of fully-transient verification study

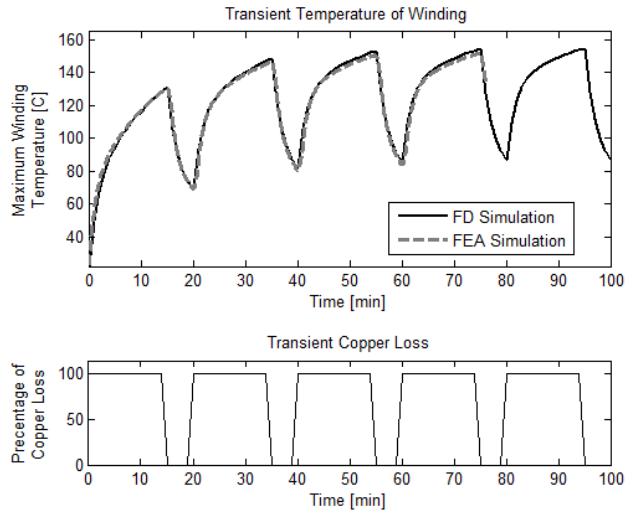

Figure 3.8 -Results from case 8 of fully-transient verification study

3.8 Initial Experimental Validation

3.8.1 Experimental Approach

An initial experimental validation of the proposed thermal model was performed on a 10 kW, three phase, concentrated winding, twelve slot, surface mount permanent machine (SMPM) machine with a rated speed and torque of 2450 rpm and 40 Nm

respectively. The geometries of the machine, the core loss, the copper loss, and midplane winding temperatures must be measured to validate the parametric thermal model.

The machine (stator) geometries were precisely measured using an optical comparator (Starrett HB400) to measure a stator tooth removed from a duplicate motor. The geometric conversion technique discussed previously, and presented in chapter 2, was used to convert the actual stator geometries to equivalent cylindrical coordinate geometries. The calculated motor geometries are presented in Table 3.6.

Table 3.6 - Calculated motor geometries

Item	Unit	Value
Angle of Foot	[rad]	1.1E-03
Angle of Tooth	[rad]	1.2E-01
Outside Angle	[rad]	2.6E-01
Inner Radius of Foot	[mm]	57.9
Outer Radius of Foot	[mm]	59.9
Radius of Windings	[mm]	60
Inner Radius of Stator	[mm]	87.4
Outer Radius of Stator	[mm]	100

The core loss was measured using no-load tests in a previous set of experiments and presented here for completeness. During the core loss tests the test machine was connected to a 10 kW DC machine and driven as a generator. Three tests were performed at no-load conditions at speed of 990, 1050, and 1700 rpm. An inline torque sensor (Omega TQ501-200) was used to measure the speed and torque during the no-load tests. Assuming that the windage, transmission or coupling, and bearing losses in the test set-up were negligible, the input mechanical power must be predominantly dissipated in core losses. Therefore, the measurements from the torque sensor were used to characterize the core loss of the machine. The results from the previous experiments are shown in Figure 3.9.

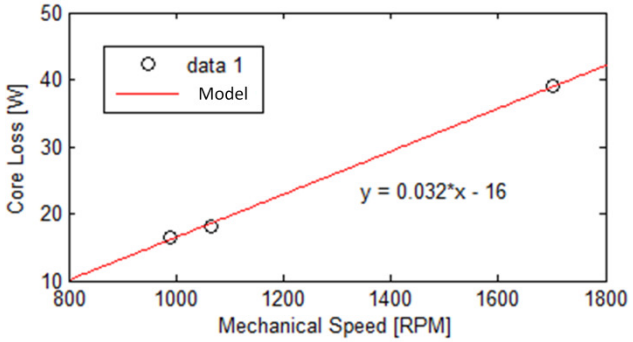

Figure 3.9 - Core loss data with trend line

The copper loss was calculated using the measured stator winding resistance and the average measured stator current for the three phases. The winding resistance was measured before the tests to be 5.11 mΩ using an digital winding tester (Baker D12R). The stator current was measured using an oscilloscope (Tektronix TDS5054), current probe (Tektronix TCPA 303), and amplifier (Tektronix TCPA 300).

Eight j-type thermocouples were placed at the mid-plane of the stator to measure the temperature response in the machine during testing. A thermocouple was placed at the top and bottom of every third slot to assess any temperature gradients in the slot. A t-type thermocouple was used to measure the ambient temperature. The thermocouples and torque sensor readings were recorded using a DAQ system. The experimental setup using for the tests is illustrated in Figure 3.10. Notice the output of the test machine is connected to a 3-phase line inductor. This is because the test machine is a low voltage high amperage machine for traction drive applications. Equipment to dissipate generated energy at low voltage and high amperage was not available necessitating a short circuit test. Shorting the phases of the test machine lead to excessive current well above the rated condition. A 3-phase line inductor was connected in Y configuration to limit the current in the circuit.

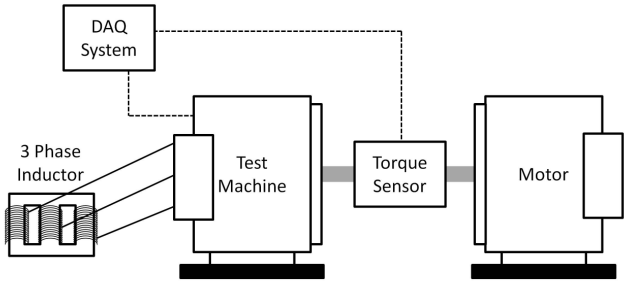

Figure 3.10 - PM motor connected to DC motor

3.8.2 Experimental Results

Three short circuit tests were run at varying speeds of 1000, 2000, and 3000 rpm. The motor geometries and the losses were input into the parametric thermal model. The results from the simulation and the measured temperatures are shown in Table 3.7 for the three tests. The measured temperatures shown are a maximum spatial average of all eight thermocouples. The temperatures were measured at steady state, which was defined as a temperature change less than 0.01°C over ten seconds. In each of the tests, the simulation was able to predict the maximum measured temperature to within +5°C. Notice that the error in the simulation is increasing with increasing temperature. This most likely comes from an overestimation of the thermal contact resistance between the windings and the stator.

Table 3.7 - Experimental and simulation results

Test Number	Copper Loss [W]	Core Loss [W]	Max Measured ΔT [C]	Max Calculated ΔT [C]	Difference Between Simulation and Measurement [C]
1	65.2	17.2	54.9	55.5	0.6
2	61.3	54.1	69.5	72.1	2.6
3	60.3	81.5	81	85.1	4.1

The results for the measured and simulated winding temperature for test 1 are presented in Figure 3.11. Notice that the transient simulation response matches the

measured response well. There is some deviation in the experimental data from the expected exponential response. This may be due to electrical noise from the motor or changes in ambient conditions during the test.

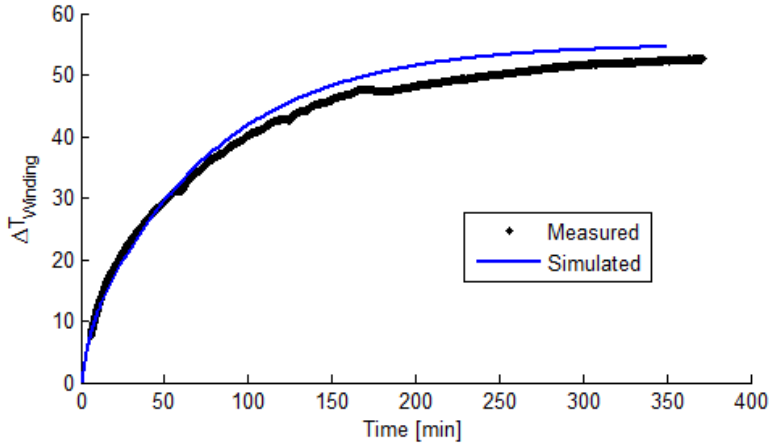

Figure 3.11 - Transient measured and simulated temperature for test 1

3.9 Discussion

The quasi-transient results show that the method of modeling the frame capacitance using an effective frame density is valid. In the results, the natural convection cases had more error than the forced convection cases. This is due to the frame modeling method. This method is where the three-dimensional effects of the frame are accounted for in the two dimensional system. This method has been previously shown to agree with forced convection better than natural convection. This fact was presented and explained in chapter 2. Also, note that cases 3 and 4 predict winding temperatures that are above typical insulation limits. This means that cases 3 and 4 are not valid designs. The temperatures also increase from case 1 to 4 and case 5 to 8, which is expected since the current density, is increasing.

The fully-transient results show that this tool can accurately simulate duty cycles. This method is not just limited to varying copper loss. In fact, this method can simulate both time varying core and copper loss at any magnitude and duty cycle. The results also show that for the same current density and convective load from the early study the maximum winding temperature is reduced. This is an expected result as the motor has time to cool between loading cycles and does not reach the maximum steady state temperature. In case 5, the average difference is negative, but the final percentage difference is 1%. This means that for a portion of the simulation the FD under predicts the maximum winding temperature, but over predicts the final maximum winding temperature. Again similar to the quasi-transient study the natural convection cases have more error than the forced convection cases.

3.10 Summary

The transient model utilized a frame capacitance technique that accounts for the three-dimensional frame capacitance. The frame capacitance technique was verified it to within 5% and 6.5% for the quasi and fully-transient cases. The fully-transient simulation of 50% and 75% duty cycles was shown to be within an average difference of 7.5°C when compared to FEA. Initial experimental validation of the proposed thermal model was presented. The results show that the proposed model was within +5°C of experimental results.

CHAPTER 4

ADVANCED COOLING OF ELECTRIC MACHINES

4.1 Introduction

This chapter presents a novel advanced cooling technique for electric machines termed the direct winding heat exchanger (DWHX). This technique places an advanced heat exchanger between the winding bundles on the stator. This cooling technique dramatically reduces the thermal resistance from the stator windings to the ambient. The cooling technique is explained in detailed and the design challenges are addressed. An initial case study is presented to demonstrate the capabilities on this advanced cooling technique. Finally, a brief discussion on manufacturability, DWHX electric machine design, and micro-feature enhanced meso-channels is presented.

4.2 Review of Salient Literature

The techniques to improve the thermal transport processes in small scale (<100kW) electrical machines has focused mainly on improving the internal and external air flow across the electrical machine in order to increase the effective heat transfer coefficient and thereby remove more heat from the machine [40, 41]. Nakahama et al used visualization experiments to understand flow patterns inside an open type motor and suggested corrections to flow separation issues that improved heat transfer [42]. Micallef et al [43] and Mugglestone et al [44] studied the flow around the end windings of the electric machine in order to improve the heat transfer from the end windings to the frame. These methods are limited because they rely on the winding heat to be conducted through the stator.

Water-cooling has typically been used in large motor applications but there has been some recent activity investigating water cooling for smaller scale motors. Direct Lamination Cooling (DLC) was used by Rippel et al to increase the current density in an 75kW induction machine by passing coolant directly through channels in the stator as seen in [45]. This work changes the flux paths inside the stator. In addition, DLC primarily removes heat from the stator and relies on conduction to cool the windings. Rahman et al presented a 42kW axial flux machine with integrated aluminum water cooling ring for HEV traction drive applications as seen in [46]. This application is an obvious cooling technique applied to a specific electric machine topology. Phase change cooling is typically applied to thermal management of large scale electrical machines on the order of several hundred megawatts [47]. Zhang et al. investigated the use of evaporative cooling for under water applications as seen in [48]. The method for applying evaporative cooling, involved submerging the stator in coolant, which lead to pool boiling. The coolant was condensed on the surface of the frame, which was cooled by a water jacket. The location of the condenser depends on the free surface, which depends on the orientation of the machine. The authors noted that a difficult challenge, large temperature gradients, arises from the increased heat transfer from evaporative cooling. Advanced cooling in electric machines is limited and there is little knowledge in designing electric machines with advanced cooling.

4.3 DWHX Electric Machines

The advanced cooling technique proposed in this chapter involves placing heat exchangers directly next to the stator windings. This direct winding cooling technique is illustrated in Figure 4.1 and incorporates a novel enhanced heat exchanger component,

termed a direct winding heat exchanger (DWHX), which is inserted between the winding bundles on the stator. A 3/4 section isometric view of an example DWHX electric machine is presented in Figure 4.2. Figure 4.2 also contains a close up view of the DHWX internal flow channel and flow inlet.

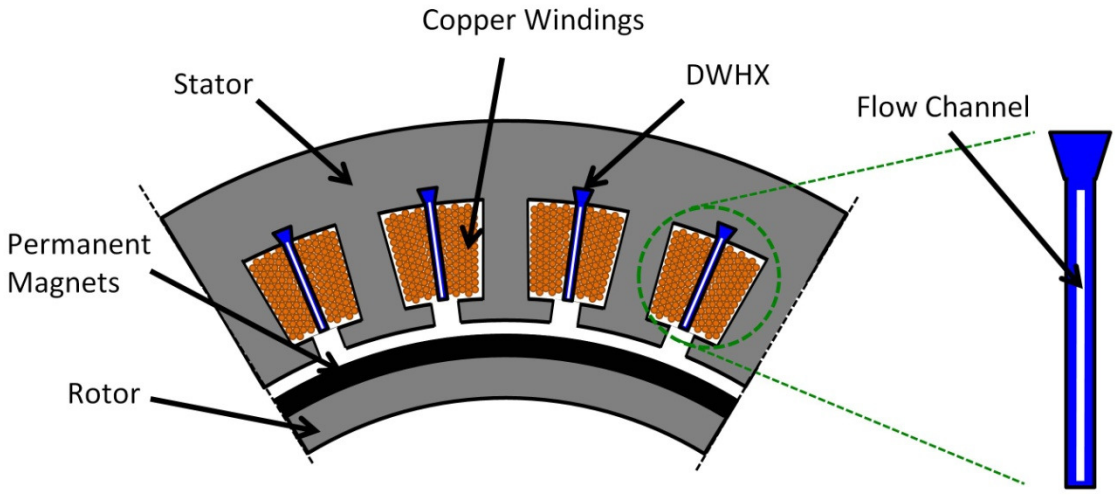

Figure 4.1 - Illustration of DWHX in stator

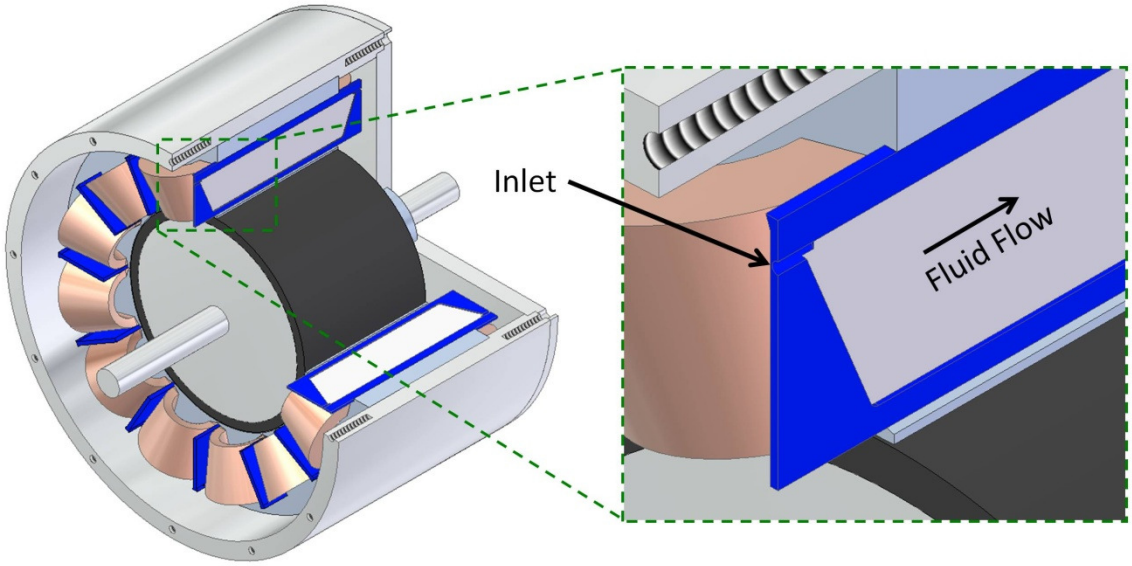

Figure 4.2 - Isometric view of an example DWHX electric machine with a close up of the DWHX internal flow channel

In high torque density machines, the majority of the losses are generated in the windings. In conventional machines, this heat is dissipated through the stator to the frame where it is rejected to the ambient. In DWHX's techniques, the heat generated by the windings is directly transferred into a passing fluid that is thermally connected either to an infinite thermal reservoir or rejects heat to ambient via an integral radiator. Consequently, the thermal resistance between the windings and the ambient rejection is significantly reduced. This allows a substantial increase in current density while maintaining thermal integrity of the winding insulation.

Several challenges must be overcome in the design of a DWHX electric machine. The first challenge is the sizing and internal channel design of the DWHX. A DWHX with a small micro-channel (hydraulic diameter between 0.1-0.5 mm) would have high heat transfer rates but significant pressure drop. This pressure drop requires more pumping power, which decreases overall system efficiency. A larger meso-channel (hydraulic diameter >0.5 mm) with reduced pressure drop would dramatically reduce the heat transfer rates. The optimal DWHX should exhibit a low pressure drop whilst providing the maximum amount of heat transfer. Peles [49] and Kosar [50] have shown that micro-features inside meso-channels achieve the best tradeoff between low pressure drop and high heat transfer. To assess the performance gains of micro-feature ehanced heat exchangers a thermal model of a DWHX electric machine must be developed.

4.4 Thermal Modeling of DWHX Electric Machines

The thermal model used for the DWHX electric machine is the same as presented in Chapter 2 with a slight modification. The modification to the model involves adding a new convective boundary condition as illustrated in Figure 4.3. The convective boundary

condition is added to the windings that will be in contact with the DWHX. The temperature of the fluid is set to be the maximum fluid temperature in the system. This model does not take into account the physical size of the DHWX. The DHWX is expected to be small in comparison to the winding and thus the conduction though it does not need to be considered.

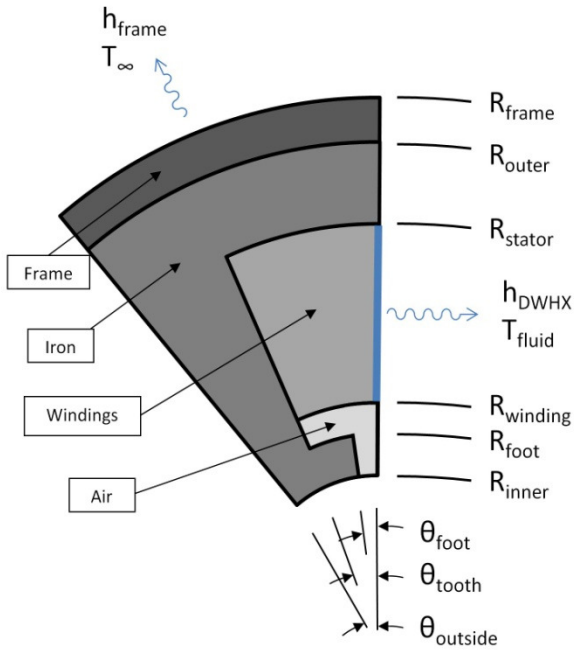

Figure 4.3 - Illustration of thermal modeling technique for the DWHX

The thermal conductivity of the windings needs to be considered when modeling a DWHX electric machine. Micro-feature enhanced heat exchangers have large heat transfer coefficients (~25,000 W/m-K). The typical effective thermal conductivity for the windings is < 1 W/m-K. Low thermal conductivity coupled with a high heat transfer coefficient leads to large temperature gradients in the windings. Increasing the effective thermal conductivity of the windings will reduce the temperature gradients and increase the effectiveness of the DWHX. Kanzaki et al [37] developed a correlation for effective

thermal conductivity of a wire bundle as a function of the filler materials and packing factor as shown in (4.1).

$$k_{eff} = \frac{k_x + k_y}{2} \tag{4.1}$$

where,

$$k_x = 2\sqrt{3}\left[\int_0^{1-F} \frac{k_1 k_2^{'}}{\left(k_2^{'} - k_1\right)\sqrt{F^2 - y^2} + \sqrt{3}k_1} dy \right.$$
$$\left. \int_{1-F}^{1/2} \frac{k_1 k_2^{'}}{\left(k_1 - k_2^{'}\right)\left(\sqrt{1}3 - \sqrt{F^2 - y^2} - \sqrt{F^2 - (y-1)^2}\right) + \sqrt{3}k_2^{'}} dy \right] \tag{4.2}$$

$$k_y = \frac{2}{\sqrt{3}}\left[\int_0^{\sqrt{3}-F} \frac{k_1 k_2^{'}}{\left(k_2^{'} - k_1\right)\sqrt{F^2 - x^2} + k_1} dx \right.$$
$$\left. \int_{\sqrt{3}-F}^{\sqrt{3}/2} \frac{k_1 k_2^{'}}{\left(k_1 - k_2^{'}\right)\left(1 - \sqrt{F^2 - x^2} - \sqrt{F^2 - \left(x - \sqrt{3}\right)^2}\right) + k_2^{'}} dx \right] \tag{4.3}$$

In (4.2) and (4.3), k_1 is the thermal conductivity of the conductor. F and $k_2^{'}$ are defined in (4.4) and (4.5) respectively.

$$F = \sqrt{2\sqrt{3}\phi_1 / \pi} \tag{4.4}$$

$$k_2^{'} = \frac{\phi_2 k_2 + \phi_3 k_3}{\phi_2 + \phi_3} \tag{4.5}$$

In (4.4), ϕ_1 is the packing factor of the conductor. In (4.5) ϕ_2 and ϕ_3 is the packing factor of the insulation and filler material respectively and k_2 and k_3 is the thermal conductivity of the insulation and filler material respectively. The filler material is typically air, but it can

be replaced with a higher thermal conductivity, such as thermal conductive epoxy, to increase the overall thermal conductivity of the windings.

4.5 Initial Case Studies

Initial DWHX electric machine thermal case studies were performed to assess the effectiveness of the proposed advanced cooling method. The motor geometries that were modeled were the same as presented in chapter 2 - figure 2.10b. The thermal properties were the same as those presented in chapter 2 - table 2.1. The heat transfer coefficient on the frame was set to natural convection conditions.

The first case study involved increasing the current inside the machine, thus increasing losses in the machine. Three different fluid temperatures were simulated under two different heat transfer coefficients. The heat transfer coefficients were 2,500 W/m^2-K and 25,000 W/m^2-K corresponding to a featureless mesochannel [51] and the average heat transfer coefficient measured by Kosar et al [50] for micro-feature enhanced meso-channels. The maximum winding temperature as a function of multiple over rated current from this case is presented in Figure 4.4. Notice that for this machine the current can be increased from 3.5 to 4.5 times the rated current without going past the thermal limits of the winding insulation. In addition, notice that the difference between the low heat transfer coefficient and high heat transfer coefficient is not large.

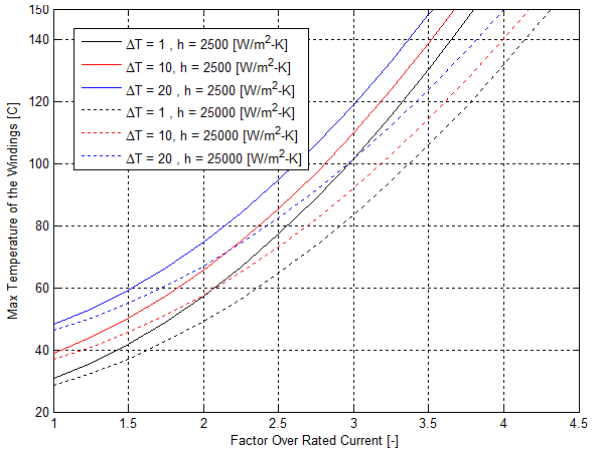

Figure 4.4 - Max winding temperature vs. factor over rated current for rejection to an infinite thermal reservoir at 20 C

The next case study was similar to the first case study, but the thermal conductivity of the windings was increased from 1 W/m-K to 10 W/m-K. The increase corresponds to a change in filler material of the windings. The maximum winding temperature as a function of multiple over rated current from this case is presented in Figure 4.5. The lower heat transfer coefficient only provides a six times increase in current over rated current. The high heat transfer coefficient provides an eight times increase in current over rated current. This shows how the thermal conductivity of the windings dramatically increases the effectiveness of the DWHX from 4.5 to 8 times over rated current. This also shows that increased heat transfer coefficient provides increased DWHX effectiveness with increased effective thermal conductivity.

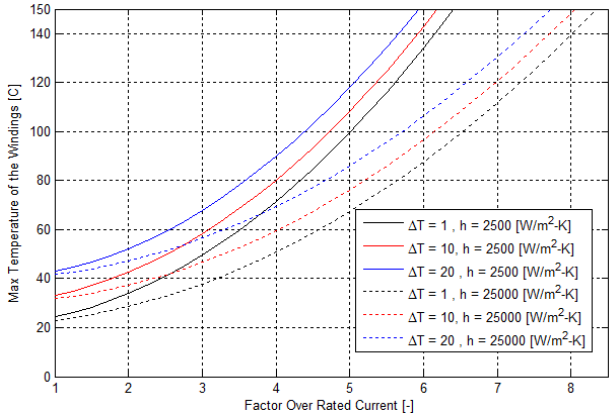

Figure 4.5 - Max winding temperature vs. factor over rated current for rejection to an infinite thermal reservoir at 20°C with increased winding thermal conductivity

The next case study preformed was a transient case study. The same machine was simulated as in the previous case studies. The transient response of the machine was simulated under rated current. Then the current in the machine was increased by a factor of three and the DWHX conditions were added. This simulates a machine running without DHWX cooling under normal load conditions and the response with DHWX cooling under overload conditions. The transient results of the DWHX electric machine rejecting to an infinite thermal reservoir at 20°C are presented in Figure 4.6. Notice that under the overload conditions the machine temperature actually decreases. This is because the DWHX provides such dramatic cooling as compared to the natural cooling through the stator frame. In addition, notice that the time constant of the machine significantly reduces when the DWHX is utilized. This is due to the increased heating load and cooling capability.

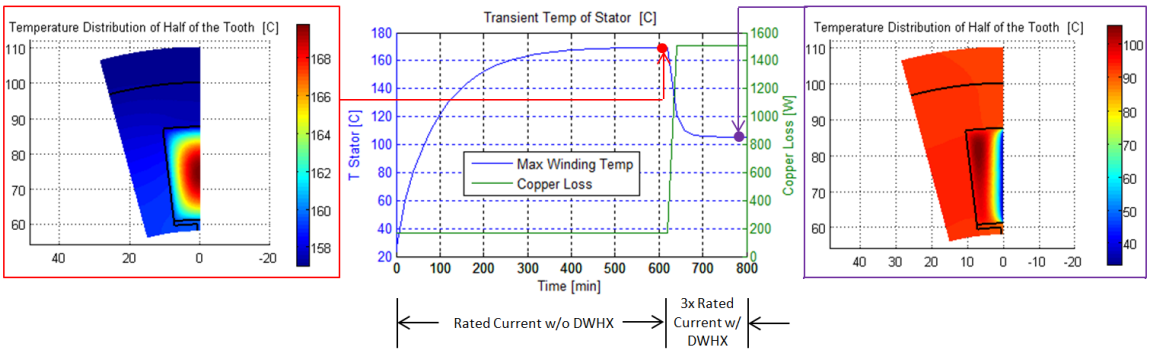

Figure 4.6 - Transient temperature with DWHX rejecting to an infinite thermal reservoir at 20°C

The same study was preformed but with heat rejection to infinite thermal reservoir at 90°C. The results are similar to the previous case and presented in Figure 4.7; however, the temperature is ~20°C higher than in the infinite reservoir case. This temperature is still lower than when that machine is at rated current and normal cooling conditions.

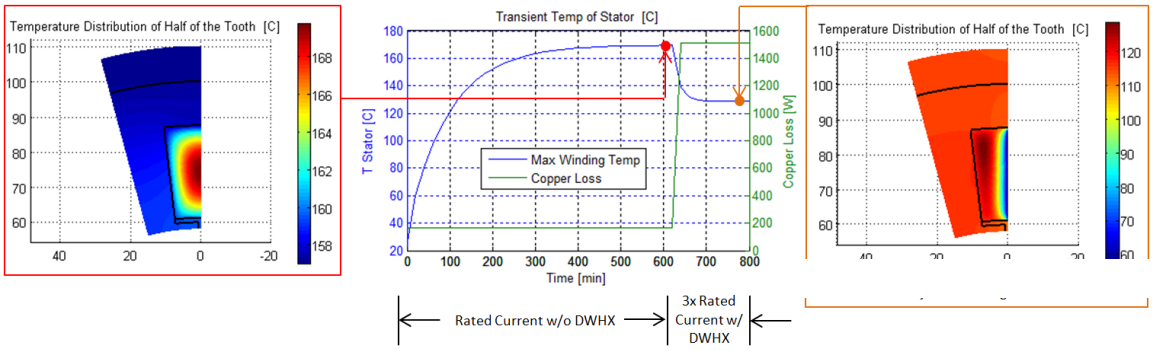

Figure 4.7 - Transient temperature with DWHX rejecting to an infinite thermal reservoir at 90°C

4.6 Discussion

This chapter has presented a significant advancement in cooling of electric machines. However, it must be noted that several other challenges exist in developing a DWHX electric machine. One such challenge is the potential for induced current in the DWHX. The DWHXs must be electrically insulated from each other or the changing magnetic

flux could induce current in the devices. Connecting the heat exchangers to a bulkhead that is non conductive presents challenges in joining and opens opportunities for leaks. Machine assemble is another challenge. The heat exchangers must be placed in after the machine is wound, but forcing the heat exchanger into place could damage the insulation. In addition, the heat exchangers must be attached to the stator. In Figure 4.1, the DHWX is attached through a dovetail joint, but this could affect the electromagnetics. These design challenges must be addressed before a DWHX electric machine can be manufactured.

It should be noted increasing the current in the machine does increase output torque until the machine saturates. An electromagnetic simulation is needed to verify the machine will produce the desired increased torque. Furthermore, the ohmic losses go up with current squared. This means that an eight times increase in current would result in sixteen times the copper loss. This significant increase in copper loss reduces the overall system efficiency. In addition, the copper loss is being absorbed by the fluid but ultimately must be rejected to the ambient environment. An integrated thermal-electromagnetic simulation that accounts for radiator and pump sizing is needed to design a DWHX electric machine to address these issues.

A high heat transfer coefficient has been shown to be desirable, but the increased pressure drop from micro-features could require significant pumping work. The tradeoff between high heat transfer and low pressure drop needs to be addressed. This could be done by developing heat transfer and pressure drop correlations for micro-features. The correlations could then be used to find the optimal tradeoff between thermal performance and flow losses.

4.7 Summary

This chapter presented a novel advanced cooling technique for electric machines termed the direct winding heat exchanger (DWHX). This technique places an advanced heat exchanger between the winding bundles on the stator. This cooling technique dramatically reduces the thermal resistance from the stator windings to the ambient. The cooling technique is explained in detailed and thermal modeling was addressed. An initial case study is presented to demonstrate the capabilities on this advanced cooling technique. It was shown that an eight times increase in stator current could be sustained with the advanced cooling technique without compromising the thermal integrity of the winding insulation. Finally, a discussion on manufacturability, DWHX electric machine design, and micro-feature enhanced meso-channels was presented.

CHAPTER 5

THERMAL PERFORMANCE OF ALIGNED MICRO-HYDROFOIL ARRAYS FOR SINGLE-PHASE HEAT EXCHANGERS

5.1 Introduction

This chapter presents an empirical approach to developing a Nusselt number correlation for aligned micro-hydrofoil arrays under single-phase cross flow with distilled water as the working fluid. The test pieces have a feature base area of 20 x 20 mm and the feature range from 375 μm to 563 μm. A test bench was developed to test the thermal performance of the micro-feature arrays. Tests were performed at two heat fluxes (37.5 W/cm^2 and 75 W/cm^2) and six Reynolds numbers (500 - 1000). The micro-hydrofoil array thermal performances ranged from 11,000 W/m^2-K to 13,000 W/m^2-K in the lowest case and 21,000 W/m^2-K to 25,000 W/m^2-K in the highest case. Two models were developed using multi-linear regression and compared to a well-known model. The final correlation was selected based a third model that reduced the number of terms as compared to the second model without reducing predictive power. The final Nusselt number correlation achieves an R^2 value of 0.99 with 95% of the data falling within ± 4.9%.

5.2 Review of Salient Literature

Microchannels and micro-feature enhanced surfaces under two-phase and single-phase flow have emerged as possible solutions to dissipating high heat fluxes. Two-phase flow in micro-channels has been well studied and several review papers on the subject are available [52-57]. The authors have noted that micro-channel flow boiling increases heat transfer and critical heat flux. The authors also note that significant challenges are still

present such as flow instability, manufacturing, large pressure drops, and accurate heat transfer coefficient correlations. These challenges, specifically high pressure drop and flow instability, limits the use of microchannels in two-phase cooling technology. Micro-feature enhanced surfaces under two-phase flow have also been well studied [58-61]. The authors noted a reduced pressure drop when compared to microchannels however the pressure instability issue remains. Pressure instability could be exacerbated in systems with unfavorable buoyancy fields thus limiting use in high heat flux applications. Single-phase flow does not suffer from these pressure instabilities thus increasing their appeal in high heat flux applications.

Tuckerman [62] was the first to suggest the use of liquid cooled microchannels for use in heat transfer applications. Since then there has been sizeable research into determining the fluid flow and heat transfer characteristics of microchannel heat exchangers [63-66]. Several reviews papers on the state of the art in microchannel heat exchanger have been published by Peng [67], Hassan [68], Morini [69], and Kandlikar [70]. Peles [49] and Kosar [50] have shown that micropin fins outperform microchannels in certain regimes. This improvement in performance has lead to an increased interest in micro-feature enhanced heat exchangers under single-phase flow for high heat flux applications.

Several shapes and patterns of micro-feature enhanced heat exchangers have been studied. Most studies have focused on either circular micropin-fins or square micro-studs in either a staggered or an aligned configuration. Micropin-fins in a staggered array made from a silicon substrate have been studied extensively [49, 50, 71, 72]. Moores et al. [73] studied staggered micropin-fins in a AlSiC metal matrix composite. Short et al. [74, 75]

studied staggered circular micropin-fins in an aluminum substrate. Chyu [76] studied aluminum diamond and square micro-studs in both staggered and aligned patterns. Siu-Ho [77, 78] studied copper micro-studs in a staggered pattern. The authors note that micro-feature enhanced heat exchangers provide dramatic heat transfer improvement, but also increase flow losses. Micro-hydrofoil arrays could provide the same heat transfer enhancement with reduced pressure drop as compared to micropin-fins and micro-studs. It should be also noted that

Kosar et al. [79, 80] presented the only reported study of micro-hydrofoil arrays. The micro-hydrofoils studied were in staggered arrays made from a silicon substrate. This study focused on two-phase flow characteristics of the micro-hydrofoil arrays. The authors provide a Nusselt number correlation for single-phase flow; however, they note that the correlation is not intended to provide a generic prediction correlation. A generic Nusselt number correlation is needed in the design of heat exchangers for use in high heat flux systems.

A geometric description of Nusselt number for aligned micro-hydrofoil arrays under single-phase flow does not exist. This chapter will present the empirical study of aligned micro-hydrofoil arrays in a copper substrate. High thermal conductivity substrates, such as copper, allow for improved fin efficiencies, which lead to lower overall thermal resistances of the array. Furthermore, the array to be studied is a doubled sided heat exchanger. This means that the micro-features extend from both base planes into the fluid, which allows for symmetric heating. This heat exchanger can be used in a variety of applications such as micro-reactors, battery cooling, and server cooling. The empirical study presented in this chapter has been augmented with a design of experiments (DOE)

approach. This DOE approach improves the statistical significance of the resulting Nusselt number correlation while reducing the number of test pieces needed.

5.3 Empirical approach

To develop an empirical Nusselt number correlation, the geometries that govern the problem must be identified. An array of micro features can be related to cross flow over tube banks. This comparison suggests that the transverse (S_t) and longitudinal (S_l) spacings are key geometric parameters. These spacings are typical non-dimensionalized by divided by the characteristic length. In micro-feature arrays, the height of the feature has been recognized as another important geometric parameter. This geometric parameter can also be non-dimensionalized by the characteristic length. Short et al. was the first to propose a Nusselt number correlation for micropin-fins that included all three of these non-dimensional geometric parameters [75]. This work will follow Short's work and utilize these three non-dimensionalized parameters to develop an empirical Nusselt number correlation.

In micropin-fins and micro-studs, the characteristic length is easily defined as the diameter of pin and length of the side respectively. Defining a characteristic length for micro-hydrofoil arrays is non-obvious. This work proposes to use the maximum thickness of the hydrofoil as the characteristic length as illustrated in Figure 5.1A. Figure 5.1A also illustrates all of the geometric dimensions for the micro-hydrofoil array.

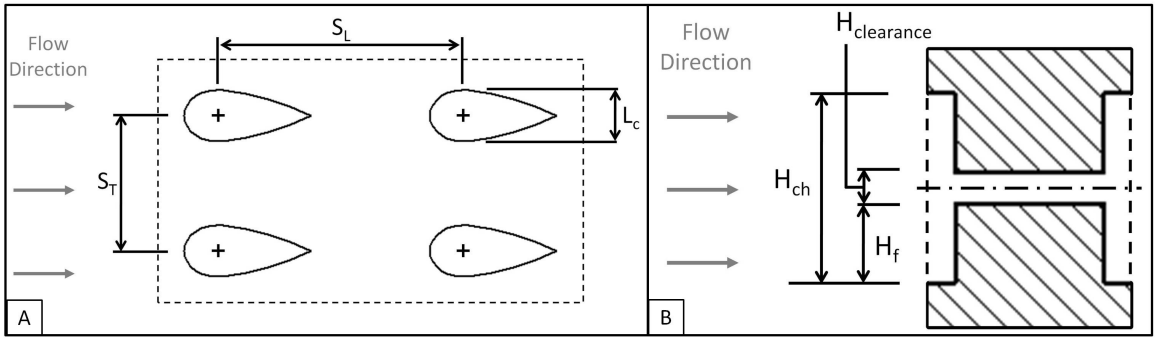

Figure 5.1 - Unit cell of micro-hydrofoil array (A). Cross section of micro-hydrofoil array height (B)

The height of the micro-hydrofoil features is illustrated in Figure 5.1B. Notice that in Figure 5.1B the features that protrude from either side do not touch in the center. This gap allows for tip clearance which has been shown to improve thermal performance [73, 81] of the array. For this study, the tip clearance was set to 10% of the feature height.

The shape of the micro-hydrofoil must also be defined. This work utilizes a standard NACA 00XX foil. This NACA four digit was selected because it is a symmetric foil with low drag coefficient thus reducing flow losses. The XX in the NACA 00XX stands for the percentage thickness to the chord. This is the ratio of characteristic length divided by the chord length as seen in (5.1).

$$r_t = \frac{L_c}{c} \tag{5.1}$$

The equation that defines this shape of the NACA 00XX foil is seen in (5.2).

$$Y(x) = \frac{r_t}{0.2} \cdot c \cdot \left[0.2969\left(\frac{x}{c}\right)^{1/2} - 0.126\left(\frac{x}{c}\right) - 0.3516\left(\frac{x}{c}\right)^2 + 0.2843\left(\frac{x}{c}\right)^3 - 0.1036\left(\frac{x}{c}\right)^4 \right] \tag{5.2}$$

Once the micro-hydrofoil shape is defined, the range of the non-dimensional parameters must be selected. This range was identified by constraining the problem with manufacturability and DOE constraints. The first constraint is tool size. 250μm is the

minimum tool size before tool breakage becomes a significant issue. Therefore the tool size were selected as an even spread of 250, 500, and 750μm. It should be noted that these tools have a standard cutting length aspect ratio of 3:1, which limits the micro-feature height. The next constraint introduced is the feature area size. Using the tool sizes defined it is possible to estimate machining time for a given feature area size. The machining time was estimated using typical micro-machining speeds, feeds, and depths of cut. It was found that a feature area size of 20 x 20 mm would lead to machining times of no more than 5 hours. Longer machining times would require tool changes, which ruin the precision of the workpiece. The final constraint was a DOE constraint that specified the ranges be an even spread across the range.

Using the constraints and the geometric definitions, a spreadsheet was created to calculate the characteristic length and height of the features. These dimensions are based on tool sizes selected and the three non-dimensional geometric parameters. The three non-dimensional parameters were varied until an even spread was indentified that satisfied the constraints. The range for each non-dimensional parameter is seen in Table 5.1. Notice that the S_l/L_c ratios are much larger than the S_t/L_c ratios. This is because hydrofoils are longer in the longitudinal direction. Thus, in an aligned pattern they can be stacked closer together in the transverse direction that in the longitudinal direction.

Table 5.1 - Values of the dimensionless ratios to be studied

	Low	Medium	High
S_t/L_c	1.8	2.2	2.6
S_l/L_c	3.5	4	4.5
H/L_c	1.33	1.67	2

A full factorial empirical study would necessitate the manufacture of twenty-seven test pieces. A design of experiments approach was taken to reduce the number of test pieces needed without losing valuable information about the testing matrix. A 3^3-1 orthogonal testing array was created as summarized in Table 5.2 denoted by tests one through nine. Also included in Table 5.2 are the dimensions for the micro-stud and featureless (blank) tests. The micro-stud and featureless tests were performed for comparison to the micro-hydrofoil arrays.

Table 5.2 - Dimensions for the test pieces

	Test 1	Test 2	Test 3	Test 4	Test 5	Test 6	Test 7	Test 8	Test 9	Studs	Blank
S_t/ L_c	1.8	2.2	1.8	2.2	2.6	1.8	2.6	2.6	2.2	2	0
S_l/ L_c	3.5	3.5	4	4	3.5	4.5	4.5	4	4.5	2	0
H/ L_c	2	1.33	1.33	1.67	1.67	1.67	1.33	2	2	1	0
L_c [μm]	375	500	375	500	562.5	375	562.5	562.5	500	500	0
H_f [μm]	750	666.7	500	833.3	937.5	625	750	1125	1000	500	0
H_{ch} [μm]	1650	1466.7	1100	1833.3	2062.5	1375	1650	2475	2200	1100	200
$N_{f,t}$	30	18	30	18	14	30	14	14	18	20	0
$N_{f,l}$	15	11	13	10	10	12	8	9	9	20	0
$N_{f,tot}$	900	396	780	360	280	720	224	252	324	400	0

5.4 Experimental Setup and Uncertainty Analysis

5.4.1 Test Piece

The micro-hydrofoil arrays were manufactured according to the testing matrix above. The arrays were machined from C145 (machinable copper) using in house advanced micro-machining technology. The solid model of one side of the micro-hydrofoil arrays is shown in Figure 5.2. A full heat exchanger is created by joining two mirror micro-hydrofoil arrays. This design allows the micro heat exchanger to be heated from both sides. The outer dimensions of the test piece are 34mm x 48mm x 3mm thick. The feature area (section containing the features) is 20mm x 20mm.

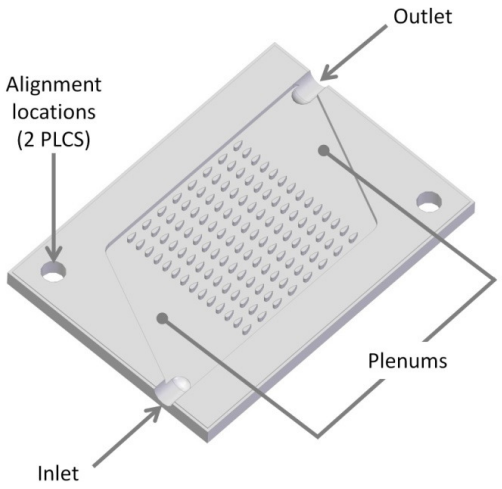

Figure 5.2 - Solid model of micro-hydrofoil test piece

5.4.2 Test Bench

The test bench utilizes copper heater blocks, with integral cartridge heaters, to symmetrically heat the test piece, as illustrated in Figure 5.3. Three 100W cartridge heaters were used in each copper heater block, which allowed from a maximum heat load of 600W.

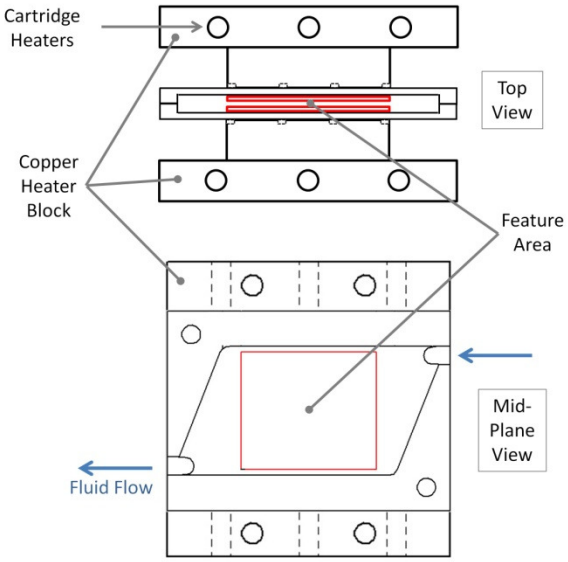

Figure 5.3 - Illustration of the symmetric heater blocks and test piece (Mid-Plane)

The test bench used to perform the experiments is illustrated in Figure 5.4. A sub cooler was used to dissipate the heat from the fluid to the environment. A 10μm filter before the pump was used to remove any particulate in the fluid. The pump was used to provide a continuous flowrate of distilled water to the system. The proportional control valve was used to control the flowrate through the test section. An exposed fluid thermocouple was used before and after the test section to measure the fluid temperature. The DC power supply was used to control the amount of heat dissipated in the test section. This power supply reports voltage and current to allow for power measurements. Twelve T-type micro-bead thermocouples were used to measure the surface temperature of the test piece. The instruments that were used as well as their uncertainties where applicable are detailed in Table 5.3.

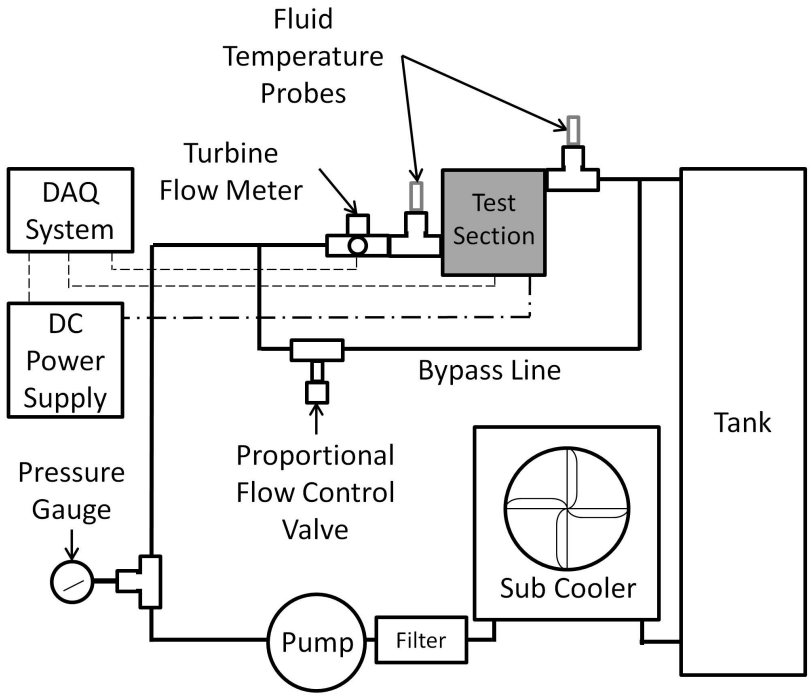

Figure 5.4 - Illustration of the test bench

Table 5.3 - Instrument list for thermal tests

Instrument	Manufacturer	Model Number	Uncertainty
Turbine Flow Meter	Flow Technology	FT4-8NEXW-LEEH4	10 cc/min
T-Type Fluid Thermocouple	Omega	TC-T-1/8NPT-E-72	0.5 °C
T-Type Micro Bead Thermocouples	Omega	COCO-001	0.5 °C
Power Supply	Acopian	Y0120LX600	4 W
Micro Gear Pump	GPM Inc	GB-P35.JVS.A	N/A
Proportional Control Valve	Omega	V516-S	N/A

Two heat fluxes, 37.5 W/cm^2 and 75 W/cm^2, along with six Reynolds numbers, 500 - 1000, were investigated resulting in twelve test conditions. Three replicates of each test condition were performed in a fully randomized test matrix. Therefore, thirty-six independent data sets were recorded for each test piece. The inlet and outlet ports of the test pieces were connected to their respective terminals on the test bench illustrated in Figure 5.4. Prior to conducting a flow test, the system was visually inspected for leaks with the fluid circulating. The heater blocks were then attached to the test section. Good contact with the surface of the test section was verified by ensuring no erroneous temperatures were recorded under full power conditions. Insulation was then added to ensure that all heat generated by the cartridge heaters was absorbed by the fluid. This was done by comparing the measured temperature rise to a temperature rise calculated through first law. Once all pretest checks were finished, the control system was activated to run the fully randomized testing matrix.

The control system first changed the proportional control valve to achieve the desired flowrate. Once a steady flowrate was achieved, power was applied to the cartridge heaters. The test continued until a steady state temperature distribution was achieved over

all thermocouples. The steady-state temperatures, power, and flowrate were then recorded. Next, the cartridge heaters were turned off and the test piece was cooled to room temperature before the next test began.

5.4.3 Data Reduction and Uncertainty Analysis

Four thermocouples were placed along the length of the micro-feature area and one thermocouple was placed in each plenum, as depicted in Figure 5.5. The thermocouples were placed on the outside surface of the heat exchanger. The thermal resistance between the thermocouple and internal surface temperature is 4.75E-6 m^2-K/W at the minimum (k = 400 W/m-k and L_{max} = 1.9 mm). The expected heat transfer coefficient is an order of magnitude less, therefore the conduction resistance is not considered. However, the conductive transport of the heat flux from the copper heater blocks to the plenums needs to be accounted for in calculating the thermal performance of the micro-features.

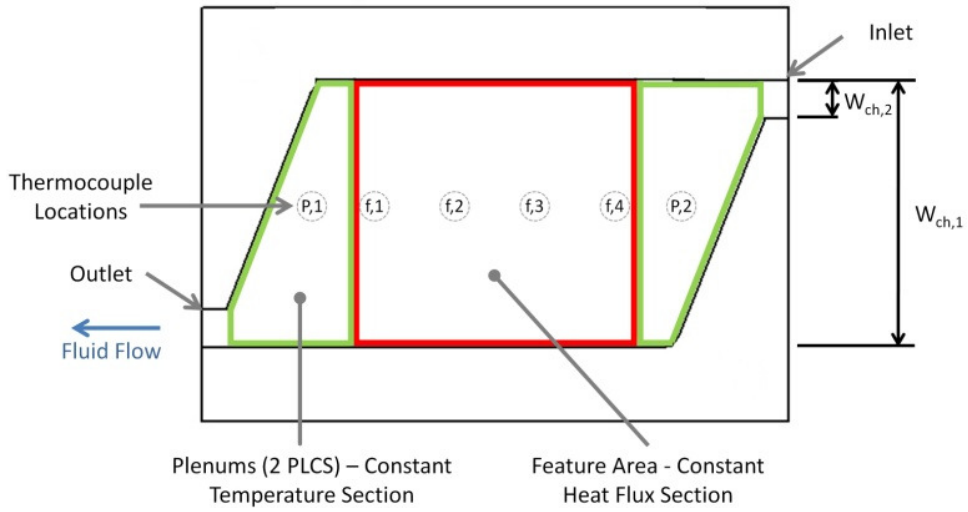

Figure 5.5 - Illustration of the thermocouple locations and modeling technique

Several assumptions were made to calculate the heat leaving through the plenums. First, the plenums were assumed to isothermal. Second, the heat transfer coefficient at that thermocouple location was assumed to be an average of the heat transfer coefficient

across the plenum. The average heat transfer coefficient in the plenum was calculated using (5.3) where L_p is the length of the plenum, $Nu(D_H)$ is the Nusselt number as a function of the hydraulic diameter, k_{fl} is the thermal conductivity of the fluid and $D_H(x)$.

$$h_{P,avg} = \frac{1}{L_p}\int_0^{L_p} Nu(D_H)\cdot\frac{k_{fl}}{D_H(x)}dx \tag{5.3}$$

The Nusselt number was obtained from correlations for fully developed internal flow through a rectangular cross section [51]. The hydraulic diameter as a function of the length through the plenum and is calculated using (5.4), where H_{ch}, is the channel height and $W_{ch,p}$ is the channel width in the plenum.

$$D_H(x) = \frac{4\cdot H_{ch}\cdot W_{ch,p}(x)}{2\cdot H_{ch} + 2\cdot W_{ch,p}(x)} \tag{5.4}$$

The channel width in the plenum varies along the length of the plenum as described in (5.5).

$$W_{ch,p}(x) = \frac{W_{ch,2} - W_{ch,1}}{L_p}\cdot x + W_{ch,1} \tag{5.5}$$

Assuming a constant heat-flux boundary, the fluid temperature is linearly dependent on flow length per (5.6), where T_O is the outlet fluid temperature, T_I is the inlet temperature, and L_{hx} is the length of the flow path in the heat exchanger.

$$T_{fl}(x) = \frac{T_0 - T_1}{L_{hx}}\cdot x + T_1 \tag{5.6}$$

The heat dissipated in each plenum is then calculated based on the plenum area, A_p, the average convection coefficient, $h_{p,avg}$, from (5.3), and the temperature difference between the plenum temperature and the fluid temperature at each plenum location, $T_{P,i}$ and $T_{fl,i}$ respectively.

$$Q_{P,i} = h_{P,avg} \cdot A_P \cdot \left(T_{P,i} - T_{fl,i}\right) \tag{5.7}$$

The total heat dissipated in the plenums is the sum of the heat from each plenum as seen in (5.8).

$$Q_{P,tot} = \sum_{i=1}^{4} Q_{P,i} \tag{5.8}$$

The feature area is assumed to be a constant heat flux section. Thus the heat transfer coefficient associated with the micro-features can be calculated using (5.9).

$$h_{f,i} = \frac{Q_m - Q_{P,tot}}{A_{base} \cdot \left(T_{f,i} - T_{fl,i}\right)} \tag{5.9}$$

In (5.9), Q_m is the measured power dissipated by the cartridge heaters, A_{base} in the base area of the micro features, and $T_{f,i}$ is the surface temperature of the features at a given location. The average feature heat transfer coefficient is calculated by average all eight calculated heat transfer coefficients as seen in (5.10).

$$h_{f,avg} = mean\left(h_{f,1-8}\right) \tag{5.10}$$

The average Nusselt number is then calculated using (5.11), where $D_{h,f}$ is the hydraulic diameter of the micro-feature array at the maximum occlusion as calculated in (5.12).

$$Nu_{f,avg} = \frac{h_{f,avg} \cdot D_{H,f}}{k_{fl}} \tag{5.11}$$

$$D_{H,f} = \frac{4 \cdot A_{c,f}}{P_f} \tag{5.12}$$

The hydraulic diameter at the maximum occlusion is calculated per classical definition in which the perimeter of the feature, P_f, is calculated per (5.13) and the cross sectional area of the feature in the flow direction, $A_{c,f}$ is calculated per (5.14).

$$P_f = 2 \cdot H_{ch} + 2 \cdot W_{ch,f} + 2 \cdot H_f \cdot N_{f,t} \tag{5.13}$$

$$A_{c,f} = H_{ch} \cdot W_{ch,f} - L_c \cdot H_f \cdot N_{f,t} \tag{5.14}$$

In (5.13), $W_{ch,f}$ is the width of the channel is the micro-feature area, H_f is the height of the feature, and $N_{f,t}$ is the number of features in the transverse direction. The width of the channel is the micro-feature area was 22 mm for every test piece. In (5.14), L_c is the characteristic length of the micro-feature.

The uncertainty of the Nusselt number calculation was determined using the Kline and McClintock method. The full uncertainty equation is shown in (5.15). The uncertainty of the length and width measurements is 0.01 mm.

$$\begin{aligned}\sigma_{Nu,avg} = \Bigg[& \left(\frac{\partial Nu_{avg}}{\partial T_1}\sigma_{T_1}\right)^2 + \left(\frac{\partial Nu_{avg}}{\partial T_0}\sigma_{T_0}\right)^2 + \left(\frac{\partial Nu_{avg}}{\partial H_{ch}}\sigma_{H_{ch1}}\right)^2 \\ & + \left(\frac{\partial Nu_{avg}}{\partial H_f}\sigma_{H_f}\right)^2 + \left(\frac{\partial Nu_{avg}}{\partial W_f}\sigma_{W_f}\right)^2 + \left(\frac{\partial Nu_{avg}}{\partial T_{P,1}}\sigma_{T_{P,1}}\right)^2 + \left(\frac{\partial Nu_{avg}}{\partial T_{P,2}}\sigma_{T_{P,2}}\right)^2 \\ & + \left(\frac{\partial Nu_{avg}}{\partial T_{P,3}}\sigma_{T_{P,3}}\right)^2 + \left(\frac{\partial Nu_{avg}}{\partial T_{P,4}}\sigma_{T_{P,4}}\right)^2 + \left(\frac{\partial Nu_{avg}}{\partial T_{f,i}}\sigma_{T_{f,i}}\right)^2 + \left(\frac{\partial Nu_{avg}}{\partial Q_m}\sigma_{Q_m}\right)^2 \Bigg]^{1/2}\end{aligned} \tag{5.15}$$

The maximum and minimum experimental uncertainties for the Nusselt number calculation were calculated to be 6.17% and 2.02% respectively. The average experimental uncertainty of the Nusselt number calculation for the entire data set was 3.67%. The calculated Nusselt numbers and the associated uncertainties are shown in Appendix C for the entire data set.

5.5 Experimental Results and Analysis

The thermal performance of each test piece was evaluated at twelve test conditions. Fourteen temperature data points were collected at each test condition. Displaying the

results for each of the test conditions for every test piece would be cumbersome and therefore characteristic results from two testing conditions are presented. The recorded temperatures from test piece three for two different heat loads, 300W and 600W, at a Reynolds number of 1000 are presented in Figure 5.6. Notice that the plenum temperatures are much lower than the feature temperatures, indicating that most of the heat is leaving through the features.

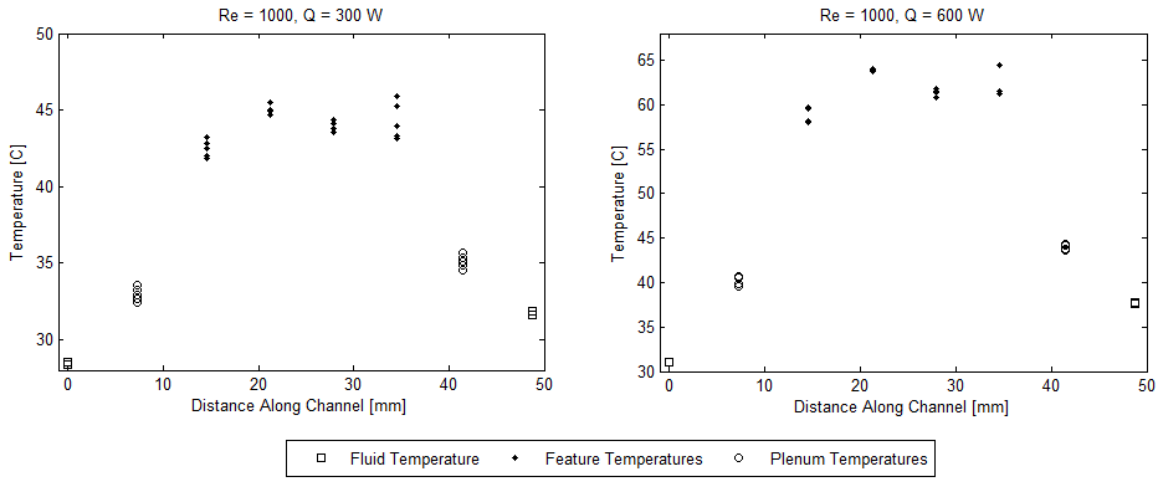

Figure 5.6 - Characteristic temperature result from Test 3 of the micro-hydrofoil arrays for Re = 1000 and Q = 300 W (left), Q = 600 W (right)

The calculated heat transfer coefficient versus Reynolds number for each of the hydrofoil tests are presented in Figure 5.7. The graphs are grouped by the same S_t/L_c ratios, which also have the same characteristics lengths. The darkened markers correspond to a heat flux of 75 W/cm^2 and the white markers correspond to a heat flux of 37.5 w/cm^2. Notice that for the S_t/L_c ratios of 2.2 and 2.6, the heat transfer coefficient is independent of the heat flux. For the S_t/L_c ratio of 2.6 the data is grouped closely together indicating high repeatability. For the S_t/L_c ratio of 1.8 the heat transfer coefficient has a

large spread. For this ratio, the volumetric flowrates were higher than for the other tests, which lead to more uncertainty thus accounting for the spread.

Test 7 performed the worst with a heat transfer coefficient ranging from 11,000 W/m^2-K to 13,000 W/m^2-K. Test 3 performed the best with a heat transfer coefficient ranging from 21,000W/m^2-K to 25,000 W/m^2-K. This is to be expected as test 7 has the fewest number of features and a larger hydraulic diameter. Conversely, test 3 has a large number of features and the smallest hydraulic diameter.

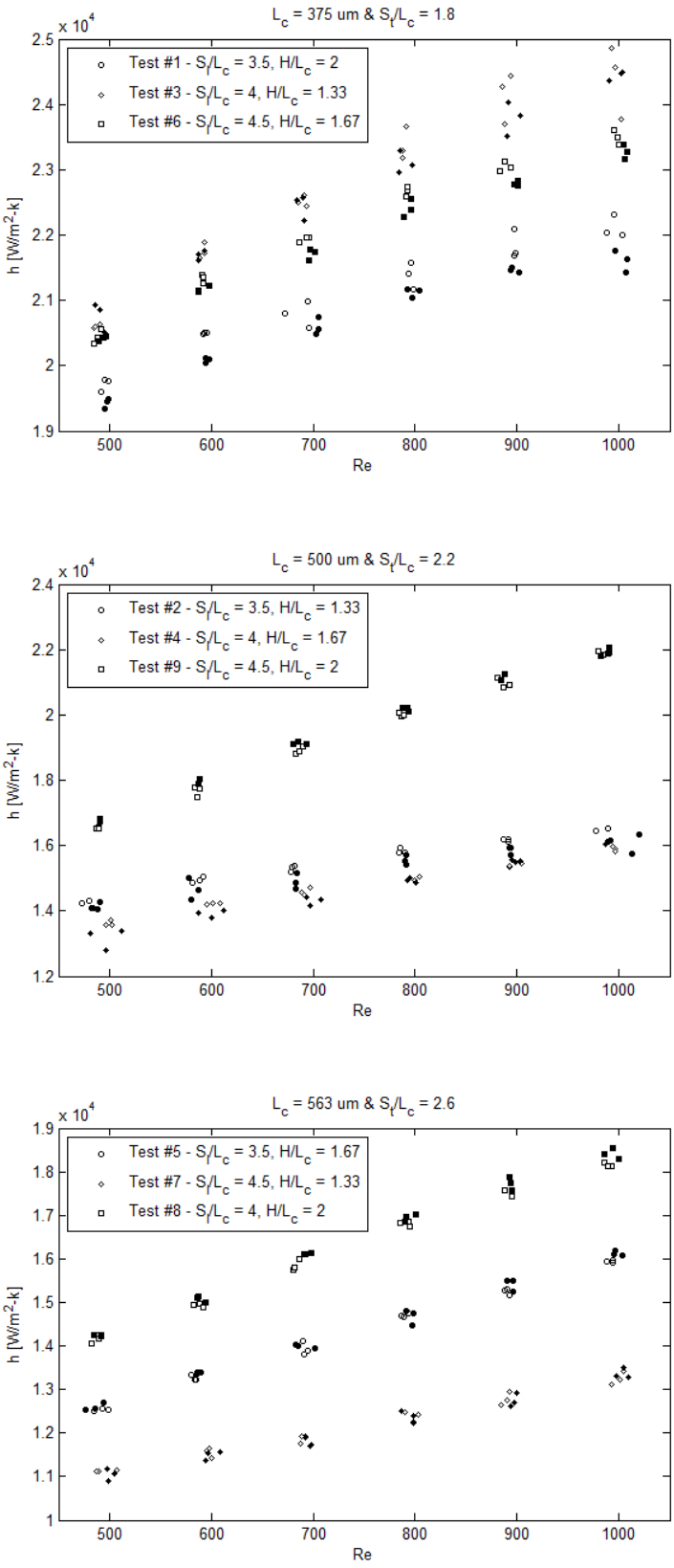

Figure 5.7 - Heat transfer coefficient vs. Re for all micro-hydrofoil tests

Three models were developed to correlate the geometries of the features and Reynolds number to the Nusselt number. The first model was presented by Short et al. [75] and is presented in (5.16).

$$Nu = C^*\left(\frac{S_t}{L_c}\right)^{\beta_1}\left(\frac{S_l}{L_c}\right)^{\beta_2}\left(\frac{H}{L_c}\right)^{\beta_3}\mathrm{Re}^n \tag{5.16}$$

The equation can be linearized by taking the natural logarithm of the entire equation. This allows for easy determination of the coefficients through linear regression. The linearized form of this equation is seen in (5.17).

$$\ln(Nu) = \beta_1 A + \beta_2 B + \beta_3 C + nD + C^*$$

where,

$$A = \ln\left(\frac{S_t}{L_c}\right),\ B = \ln\left(\frac{S_l}{L_c}\right),\ C = \ln\left(\frac{H}{L_c}\right),\ \textit{and}\ \ D = \ln(\mathrm{Re}) \tag{5.17}$$

The resulting coefficients of the linear regression are presented in (5.18).

$$Nu = 0.878\cdot\left(\frac{S_t}{L_c}\right)^{0.993}\left(\frac{S_l}{L_c}\right)^{0.232}\left(\frac{H}{L_c}\right)^{0.649}\mathrm{Re}^{0.265} \tag{5.18}$$

The second model takes into account all possible interactions between the experimental parameters. This can be done because of the 3^{3-1} orthogonal testing array allows information about the testing interaction terms to be extracted from the data. However, since the order of the testing array was reduced to second-order, only up to second-order interactions can be included in the model. The possible interaction terms are displayed in (5.19).

$$\ln(Nu) = f\left(A, B, C, D, AB, AC, AD, BC, BD, CD, A^2, B^2, C^2, D^2\right) \tag{5.19}$$

The resulting coefficients of the linear regression are presented in (5.20). Notice that the coefficient in front of the second term is zero. This means that in this model the second term in not significant, but rather its interaction with the other terms is significant.

$$\begin{aligned}\ln(Nu) = {} & 13.51 \cdot \ln\left(\frac{S_t}{L_c}\right) + 0 \cdot \ln\left(\frac{S_l}{L_c}\right) - 5.76 \cdot \ln\left(\frac{H}{L_c}\right) - 0.45 \cdot \ln(\mathrm{Re}) \\ & -6.17 \cdot \ln\left(\frac{S_t}{L_c}\right) \cdot \ln\left(\frac{S_l}{L_c}\right) + 0.51 \cdot \ln\left(\frac{S_t}{L_c}\right) \cdot \ln\left(\frac{H}{L_c}\right) + 0.33 \cdot \ln\left(\frac{S_t}{L_c}\right) \cdot \ln(\mathrm{Re}) \\ & +3.98 \cdot \ln\left(\frac{S_l}{L_c}\right) \cdot \ln\left(\frac{H}{L_c}\right) + 0.204 \cdot \ln\left(\frac{S_l}{L_c}\right) \cdot \ln(\mathrm{Re}) + 0.12 \cdot \ln\left(\frac{H}{L_c}\right) \cdot \ln(\mathrm{Re}) \\ & -3.41 \cdot \ln\left(\frac{S_t}{L_c}\right)^2 + 0.93 \cdot \ln\left(\frac{S_l}{L_c}\right)^2 - 0.39 \cdot \ln\left(\frac{H}{L_c}\right)^2 + 0.006 \cdot \ln(\mathrm{Re})^2 - 1.8\end{aligned} \tag{5.20}$$

The third model was developed by performing a multi-linear regression considering every possible combination of experimental factors and their interactions. This process is detailed in appendix B. The resulting fits were screened and reduced to the models that had percentage deviation from the actual data of less than 10%. The R^2/MSE value of all of the screened models was evaluated no significant variation in the value was observed. The final correlation was then selected based on the minimum number of parameters in the model. The resulting model contained seven parameters; all of the experimental factors, two interaction terms, and one squared term. The coefficients of the linear regression for the third model are presented in (5.21).

$$\ln(Nu) = 17.04 \cdot \ln\left(\frac{S_t}{L_c}\right) + 4.59 \cdot \ln\left(\frac{S_l}{L_c}\right) - 5.85 \cdot \ln\left(\frac{H}{L_c}\right) + 0.272 \cdot \ln(\mathrm{Re})$$
$$-7.17 \cdot \ln\left(\frac{S_t}{L_c}\right) \cdot \ln\left(\frac{S_l}{L_c}\right) + 4.53 \cdot \ln\left(\frac{S_l}{L_c}\right) \cdot \ln\left(\frac{H}{L_c}\right) - 3.15 \cdot \ln\left(\frac{S_t}{L_c}\right)^2 - 9.02 \quad (5.21)$$

The percentage error between the model and the actual data for each of the three models Figure 5.8. Notice that the model developed by Short captures much of the data, but has an R^2 value of 0.793 and 95% of the data falls within ± 21.2%. The second model has an R^2 value of 0.99 and 95% of the data falls within ± 3.8%. The third model has an R^2 value of 0.99 and 95% of the data falls within ± 4.9%. The third model offers the best tradeoff between accuracy and number of terms. A reduced number of interaction terms increases the model statistical significance.

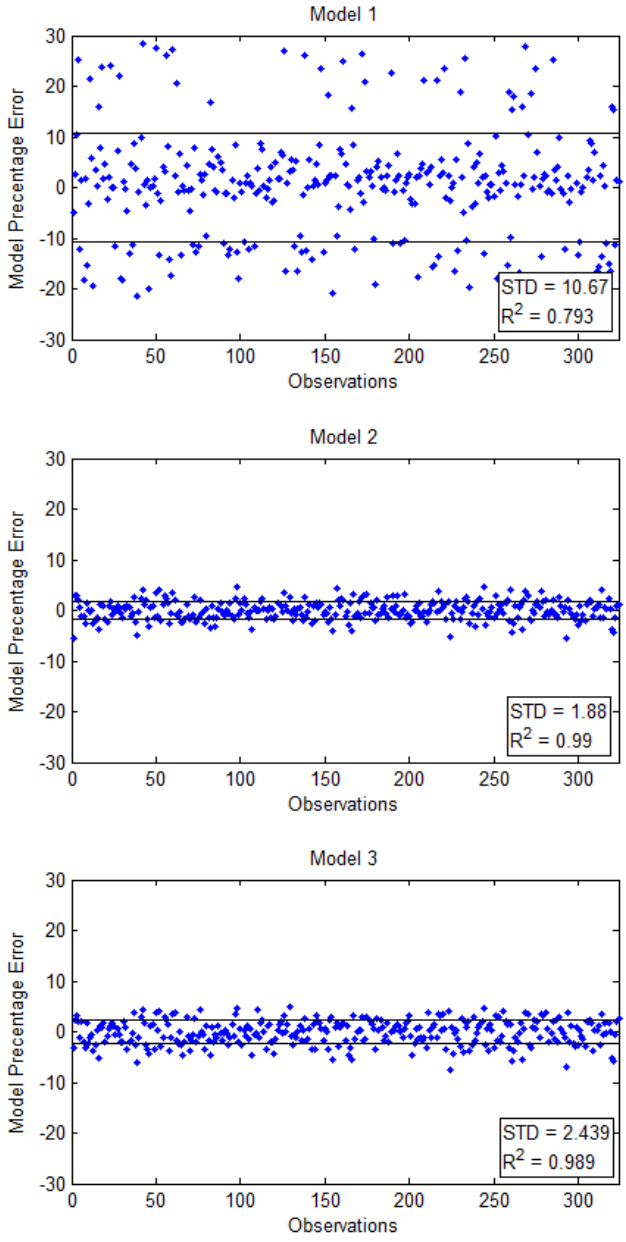

Figure 5.8 - Residuals plot for each Nusselt number model

The comparison between experimental Nusselt numbers to the third model prediction for all the micro-hydrofoil tests is presented in Figure 5.9 This confirms that model successfully represents the experimental data for each test.

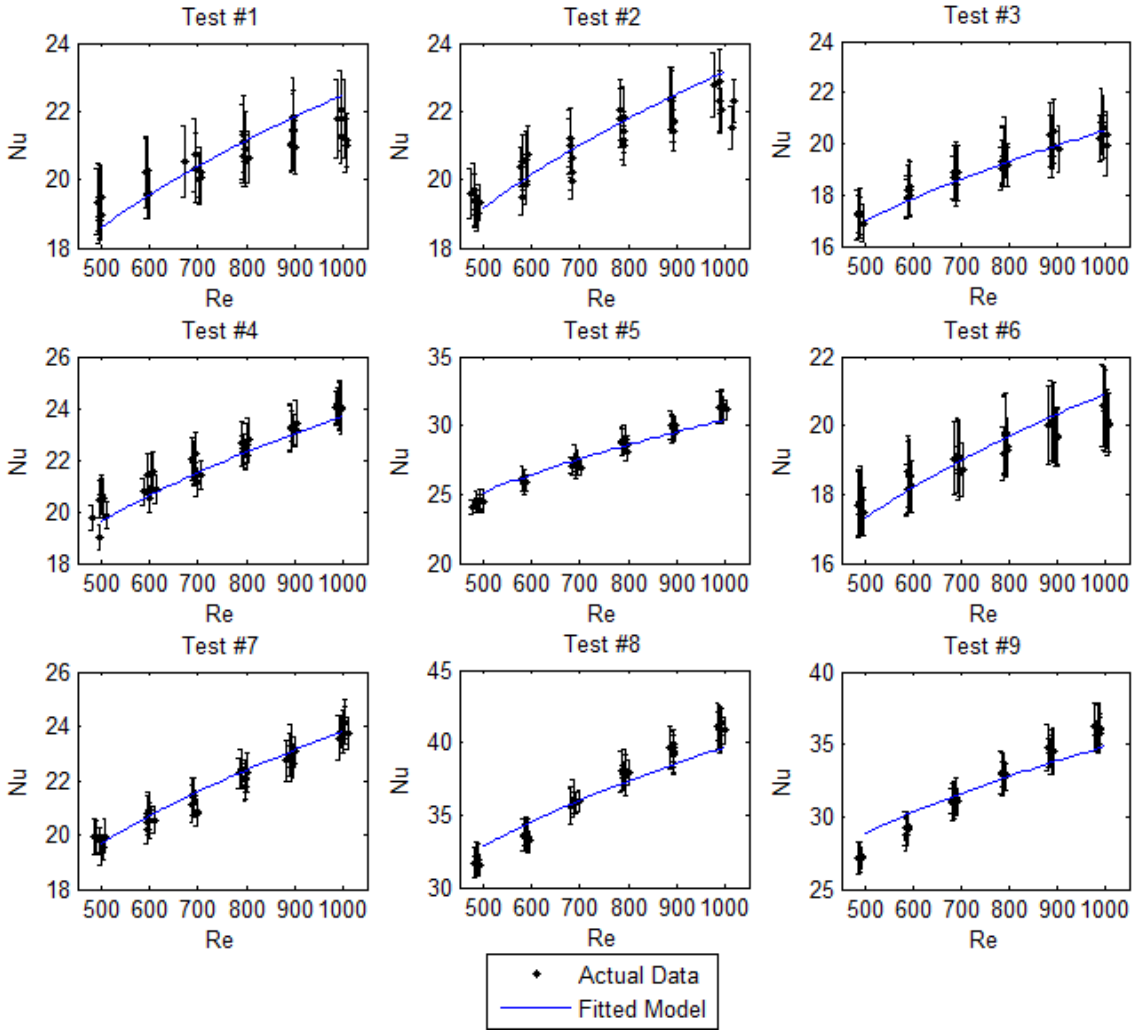

Figure 5.9 - Comparison between the fitted model and experimental data for all tests

The results from the micro-stud and featureless tests are presented in Figure 5.10. The micro-stud test piece heat transfer coefficient ranges from 17,000 to 22,000 W/m^2-K. The featureless test piece heat transfer coefficient ranges from 11,000 to 15,000 W/m^2-K. Also notice that the featureless test has data points do not group together well by Reynolds number. The featureless test piece required lower volumetric flowrates resulting in smaller intervals between investigated flowrates as compared to as the micro-feature test pieces. Observed pressure fluctuations during the testing of the featureless test piece limited the control of precise flowrates.

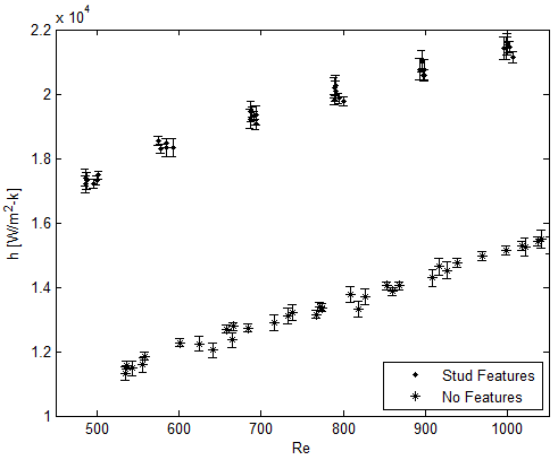

Figure 5.10 - A comparison of heat transfer coefficient between micro-stud test piece and featureless test piece at various Reynolds numbers

5.6 Discussion

A direct comparison between the micro-stud test piece and any of the micro-hydrofoil test pieces cannot be made because the S_t/L_c, S_l/L_c, H/L_c, and D_h are not consistent. A weak comparison can be drawn between the micro-stud and micro-hydrofoil shapes by utilizing the proposed model. For this comparison, the S_t/L_c, H/L_c, A_c, and D_h from the micro-stud array were used to calculate the convection coefficient for an equivalent micro-hydrofoil array using the proposed Nusselt number correlation. However, it must be noted that an identical S_l/L_c ratio for the micro-hydrofoil shape is not feasible due to the inherent feature length increase in the flow direction. The increase in feature length also precludes the consideration of identical feature densities for the micro-stud and micro-hydrofoil arrays resulting in different total heat transfer area. This effect can be reduced, but not eliminated, if the pattern of the feature array is staggered rather than aligned.

The comparison between the experimental micro-stud test piece and the predicted performance of a similar micro-hydrofoil array with equivalent S_t/L_c, H/L_c, and D_h values

and a S_l/L_c ratio of 3.5, is shown in Figure 5.11A. Notice that the micro-stud test piece outperforms the predicted micro-hydrofoil array. This can be attributed to the increased total heat transfer of the micro-stud test piece.

A comparison between the micro-stud piece and the hydrofoil array with the closest hydraulic diameter is shown in Figure 5.11 B. The hydraulic diameter of the micro-stud test piece is 0.66mm and the test 1 micro-hydrofoil piece is 0.57mm. Notice that the test 1 micro-hydrofoil slightly outperforms the micro-stud array. The comparison between the micro-stud piece and the hydrofoil array with the similar number of features is shown in Figure 5.11C. The number of features in the micro-stud test piece is 800 and in the test 3 micro-hydrofoil piece is 780. Notice that the test 3 micro-hydrofoil significantly outperforms the micro-stud array. These comparisons are incomplete in that they do not consider pressure drop. The advantage of micro-hydrofoil arrays should be good thermal performance with significant reduction in pressure drop. A complete comparison between a micro-stud array and micro-hydrofoil array must include pressure drop characteristics. A comparison of the thermal performance of the micro-stud array, the featureless test piece, test piece 3 and the predicted performance of the featureless test piece using a standard Nusselt number correlation for fully developed flow [51] is presented in Figure 5.11C. Notice that the heat transfer coefficient for the featureless test piece increases with Reynolds number indicating a developing flow. However, featureless experimental data is within ±20% of the standard fully developed full correlation. Both micro-feature enhanced test pieces significantly outperform the featureless test piece; a 51% increase in convection coefficient is achieved by the micro-stud and similarly a 91% increase is demonstrated by the micro-hydrofoil features. Furthermore, the data demonstrates a

~20% increase in thermal performance of the micro-hydrofoil array in test piece 3 over the micro-stud array.

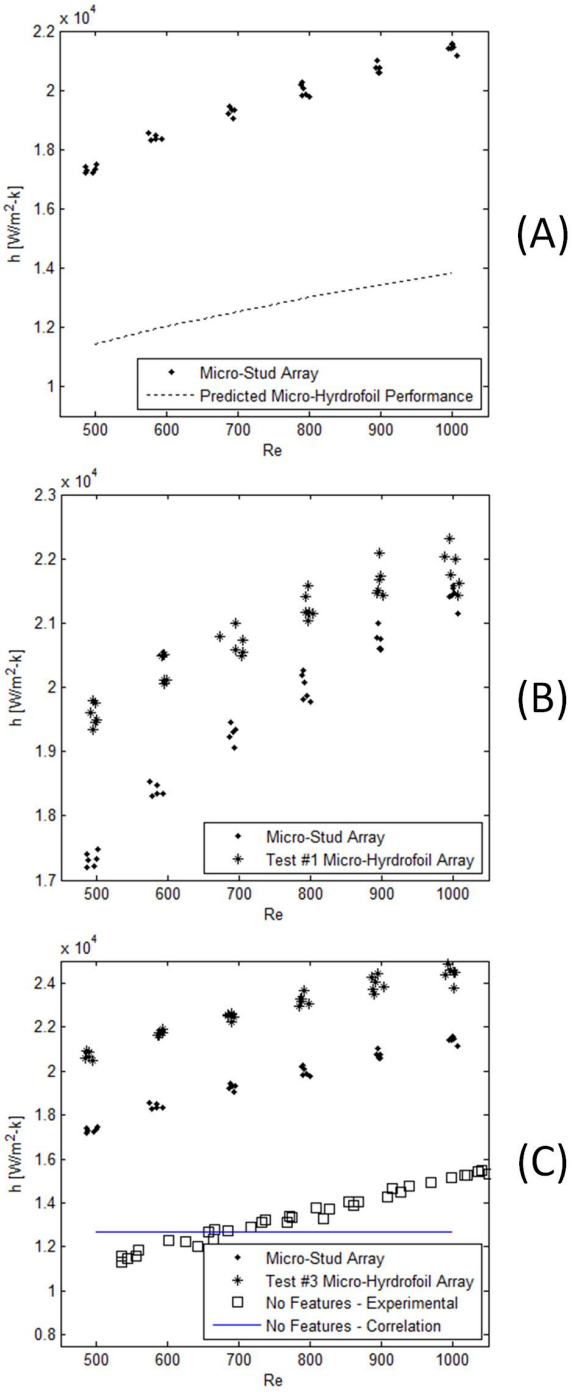

Figure 5.11 - Comparison of micro-stud experimental data to prediction of similar Hydrofoil (A). Comparison of micro-stud experimental data to micro-hydrofoil with similar hydraulic diameter (B). Comparison of micro-stud and micro-hydrofoil with similar number of features (C).

The definition for macro scale transition from laminar flow to turbulent flow is defined at a Reynolds Number of 2,300. In micro-feature enhanced meso-channels, the transition point is difficult to assess due to the complexities associated with average velocity descriptions. The highest Reynolds number tested in this study was 1,000. This indicates that the flow in this study was laminar if the macro scale definition is used. It should also be noted that the Reynolds number was calculated at the location of highest velocity and maximum occlusion. Therefore, it is expected that the average Reynolds number through the geometry would be lower. It is expected that the flow through the features in this study was laminar. Furthermore, the data does not show any evidence of a flow regime transition. It is expected that the region above the features would reach turbulence due to the small clearance. However, this would not affect the bulk flow transition. A high fidelity computational fluid dynamics simulation would provide further insight into the flow transition regions.

The maximum and minimum uncertainties for the Nusselt number calculation were 6.17% and 2.02% respectively. The average uncertainty of the Nusselt number calculation for the entire data set was 3.67%. The average uncertainty of this data set is smaller reported in [50, 73, 75]. Kosar et al. note that larger surface to fluid temperature differences would decrease uncertainty [50]. Larger temperature differences were achieved in this study because of the larger test section. The larger test sections allows for higher flowrates thus reducing the fluid temperatures. Furthermore, the surface temperatures in this study were much higher than reported by Kosar et al. The lowest surface temperature measured was 42°C while the highest surface temperature was 88°C. Lower fluid temperatures and higher surface temperatures result in larger temperature

differences, thus decreasing the uncertainty of the Nusselt number calculation. Lower uncertainty in the Nusselt number calculation allows for a precise correlation to be developed such as the one proposed in (5.21).

The proposed correlation was empirically developed; however, the proposed correlation still has a fundamental geometric foundation. The proposed Nusselt number correlation can be recast as shown in (5.22).

$$Nu = 1.21E-4\left(\frac{S_t}{L_c}\right)^{17.04}\left(\frac{S_l}{L_c}\right)^{4.59}\left(\frac{H}{L_c}\right)^{-5.85}(\mathrm{Re})^{0.272}\cdot e^{\left(-7.17\cdot\ln\left(\frac{S_t}{L_c}\right)\cdot\ln\left(\frac{S_l}{L_c}\right)+4.53\cdot\ln\left(\frac{S_l}{L_c}\right)\cdot\ln\left(\frac{H}{L_c}\right)-3.15\cdot\ln^2\left(\frac{S_t}{L_c}\right)\right)} \tag{5.22}$$

Notice that the correlation resembles Short's form multiplied by a correction factor. Short's form accounts for the dimensionless geometric parameters (S_t/L_c, S_l/L_c, and H_f/L_c) and the Reynolds number. Nusselt number correlations are fundamentally a function of Reynolds number, Prandtl number, and dimensionless geometric parameters. This study only considered one fluid; therefore, Prandtl number is not included in the correlation. The micro-feature arrays impart three-dimensional effects that can only be captured through the interactions of the dimensionless geometric parameters. The interactions of the dimensionless geometric parameters make up the correction term in the proposed correlation. Specifically, the interactions between the dimensionless transverse spacing and the dimensionless longitudinal spacing, the dimensionless longitudinal spacing and the dimensionless feature height, and the dimensionless transverse spacing with itself capture the three-dimensional effects in the Nusselt number calculation. Therefore, the proposed Nusselt number correlation is not a contrived form, but rooted in geometric and physical significance. If a different form is used to calculate the hydraulic diameter, such

as wetted volume divided by wetted surface area, it would possibly capture more of the three dimensional effects present in the array and reduce the interactions required in the correction term. A complete investigation of the effect of the form of the hydraulic diameter is beyond the scope of this study.

5.7 Summary

This chapter has detailed an empirical approach to developing a Nusselt number correlation for micro-hydrofoil arrays under single-phase cross flow. The test pieces were designed and manufactured in-house with advanced micro machining technology. The device design allowed for symmetric heating. A test bench was developed to test the thermal performance of the micro-feature arrays. Data reduction and uncertainty analysis was presented for the experimental data. The micro-hydrofoil array thermal performance ranged from 11,000 W/m^2-K to 13,000 W/m^2-K in the lowest case and 21,000 W/m^2-K to 25,000 W/m^2-K in the highest case. Two models were developed using a multi-linear regression and compared to an existing model. The existing model achieved an R^2 value of 0.793 with 95% of the data falling within ± 21.2% of the predicted performance. The final correlation was selected based a third model that reduced the number of terms as compared to the second model without reducing predictive power. The final Nusselt number correlation achieves an R^2 value of 0.99 with 95% of the data falling within ± 2.5%. The Nusselt number correlation developed in this study achieves a 4x reduction in prediction error for micro-hydrofoil arrays.

CHAPTER 6

FLOW PERFORMANCE OF ALIGNED MICRO-HYDROFOIL ARRAYS FOR SINGLE-PHASE HEAT EXCHANGERS

6.1 Introduction

This chapter presents an empirical approach to developing a friction factor correlation for aligned micro-hydrofoil arrays under single-phase cross flow with distilled water as the working fluid. The test pieces were designed and manufactured in-house using advanced high-speed high-precision micro-milling technology. The test pieces have a feature base area of 20 x 20 mm and the feature range from 375 μm to 563 μm. A test bench was developed to measure the pressure drop across the micro-feature arrays. Tests were performed at six Reynolds numbers (500 - 1000). The micro-hydrofoil array pressure drop ranged from 0.3 to 0.5 kPa in the lowest case measurable case and 2 to 7 kPa in the highest case. Two models were developed using multi-linear regression and compared to an existing model. The final correlation was selected based a third model that reduced the required number of terms as compared to the second model without sacrificing predictive power. The final friction factor correlation achieves an R^2 value of 0.92 with 95% of the data falling within ± 10.2%. A detailed literature review has been presented in the previous chapter and will not be repeated here

6.2 Empirical Approach

A detailed explanation of the empirical approach has been presented in the previous chapter. The illustration of the micro-hydrofoil array dimensions is presented in Figure 6.1. The dimension for the micro-hydrofoil arrays are presented in Table 6.1. Figure 6.1 and Table 6.1 are included in this chapter for reference.

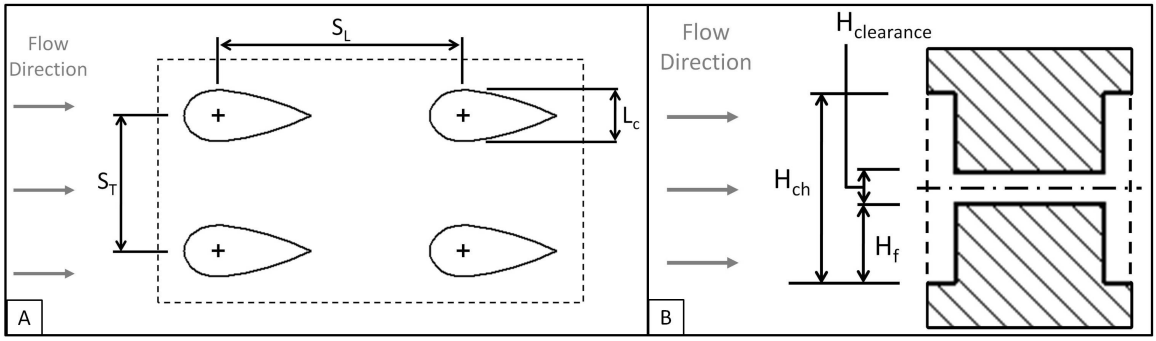

Figure 6.1 - Unit cell of micro-hydrofoil array (A). Cross section of micro-hydrofoil array height (B)

Table 6.1 - Dimensions for the test pieces

	Test 1	Test 2	Test 3	Test 4	Test 5	Test 6	Test 7	Test 8	Test 9	Studs	Blank
S_t/ L_c	1.8	2.2	1.8	2.2	2.6	1.8	2.6	2.6	2.2	2	0
S_l/ L_c	3.5	3.5	4	4	3.5	4.5	4.5	4	4.5	2	0
H/ L_c	2	1.33	1.33	1.67	1.67	1.67	1.33	2	2	1	0
L_c [μm]	375	500	375	500	562.5	375	562.5	562.5	500	500	0
H_f [μm]	750	666.7	500	833.3	937.5	625	750	1125	1000	500	0
H_{ch} [μm]	1650	1466.7	1100	1833.3	2062.5	1375	1650	2475	2200	1100	200
$N_{f,t}$	30	18	30	18	14	30	14	14	18	20	0
$N_{f,l}$	15	11	13	10	10	12	8	9	9	20	0
$N_{f,tot}$	900	396	780	360	280	720	224	252	324	400	0

6.3 Experimental Setup and Uncertainty Analysis

6.3.1 Test Piece

Micro-hydrofoil arrays were manufactured according to the testing matrix presented above. These test arrays were made from C145 (machinable copper) using in house advanced micro-machining technology. A solid model of one side of the micro-hydrofoil arrays is displayed in Figure 6.2. Notice in Figure 6.2 the pressure ports before and after the feature area (section containing the features). These were used to measure the differential pressure across the micro-feature array. A full heat exchanger is created by

joining two mirror micro-hydrofoil arrays. The dimensions of the test piece are 34mm x 48mm x 3mm thick. The feature area is 20mm x 20mm.

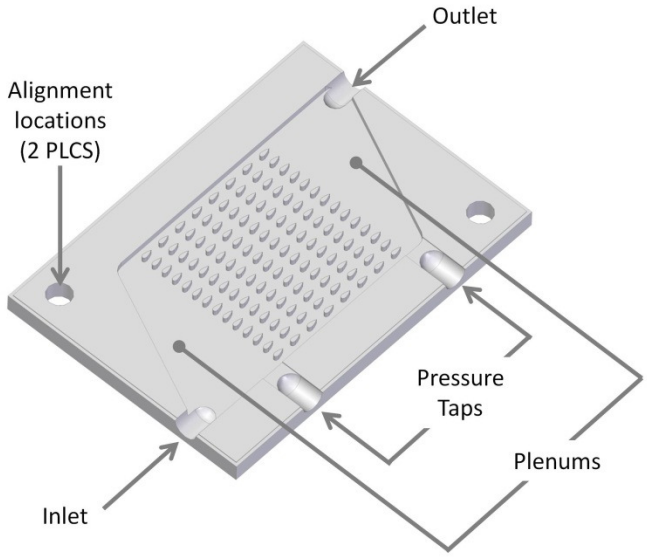

Figure 6.2 - Solid model of micro-hydrofoil test device

6.3.2 Test Bench

To evaluate the pressure drop across the micro-hydrofoil arrays a test bench was developed as illustrated in Figure 6.3. The test bench is similar to the one presented in the previous chapter. The only difference is the copper heater blocks were replaced with a differential pressure manometer. The differential pressure manometer was used to measure the pressure drop through the test section. The manometer was attached to the test section's pressure ports with flexible tubing.

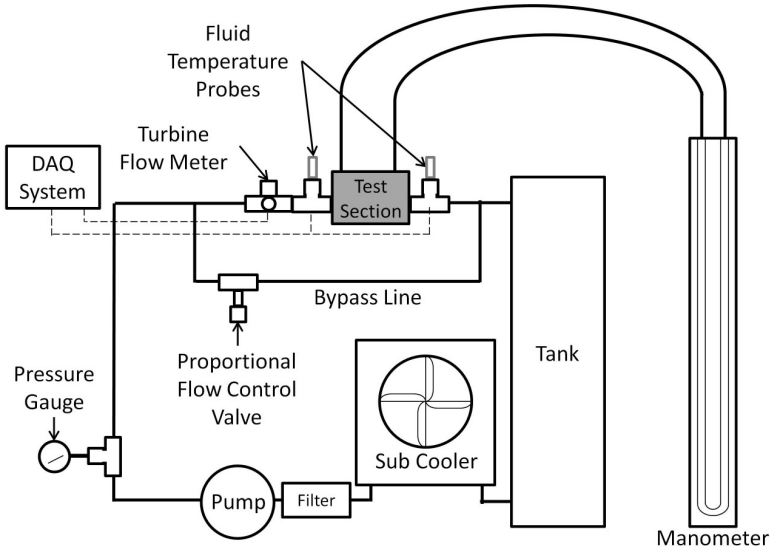

Figure 6.3 - Illustration of pressure drop test bench

The top section view of the test section is illustrated in Figure 6.4. Copper pipes were soldered to the inlet, outlet, and pressure ports. The pipes were then connected to the rest of the system with flexible tubing and hose clamps. The instruments used along with the manufacturer, model number, and uncertainty where applicable are presented in Table 6.2.

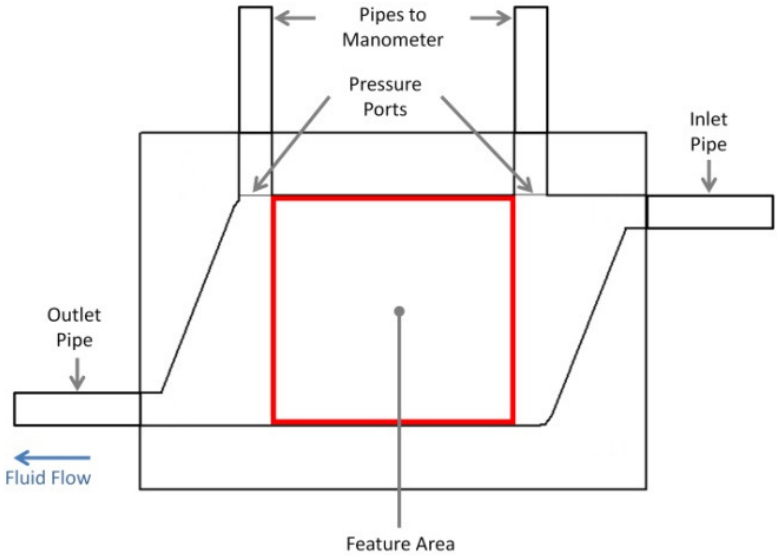

Figure 6.4 - Top section view of test section

Table 6.2 - Instrument list for pressure drop tests

Instrument	Manufacturer	Model Number	Uncertainty
Turbine Flow Meter	Flow Technology	FT4-8NEXW-LEEH4	9 cc/min
T-Type Fluid Thermocouple	Omega	TC-T-1/8NPT-E-72	0.5 °C
Manometer	Dwyer	1223-36-D	0.05 inH2O
Micro Gear Pump	GPM Inc	GB-P35.JVS.A	N/A
Proportional Control Valve	Omega	V516-S	N/A

Six Reynolds numbers were tested between 500 and 1000 at an interval 100. At each Reynolds number three replicate pressure drop measurements were taken. This results in eighteen tests per test piece. The eighteen tests were fully randomized to guarantee statistical independence thereby increasing significance of the correlation.

The individual test pieces, defined in Table 6.1, were tested in a random order. The inlet, outlet, and pressure ports of the test pieces were connected to their respective terminals on the test bench illustrated in Figure 6.3. Prior to conducting a flow test, the system was visually inspected for leaks with the fluid circulating. Next, the flowrate was manually varied using the proportional control valve to ensure each flowrate in the test could be achieved with the starting voltage set point for the pump. The low flowrates in the testing matrix required a reduction in pumping power due to the low pressure loss in test piece. Once all the pretest checks were completed, the control system was activated to run the fully randomized test for that particular test piece.

The control system first used the proportional control valve to achieve the desired flowrate. Once a steady flowrate was achieved, the user is prompted to enter the pressure drop displayed by the manometer. The system then records the flowrate and fluid

temperatures. The proportional control valve is then fully closed before continuing with the next test.

6.3.3 Data Reduction and Uncertainty Analysis

Once the tests were completed, data analysis was performed on the resulting data. First the actual Reynolds achieved during the tests is calculated using (6.1).

$$\mathrm{Re} = \frac{\dot{V} \cdot D_{h,f} \cdot \rho}{A_{c,f} \cdot \mu} \tag{6.1}$$

In (6.1), ρ is the density of the fluid, μ is the viscosity of the fluid, and $\dot{V}$ is the volumetric flowrate measured by the flowmeter. The hydraulic diameter is calculated at the maximum occlusion of the features as defined in (6.2).

$$D_{h,f} = \frac{4\left(H_{ch} \cdot W_{ch} - L_c \cdot H_f \cdot N_{f,t}\right)}{2 \cdot H_{ch} + 2 \cdot W_{ch} + 2 \cdot H_f \cdot N_{f,t}} \tag{6.2}$$

In (6.2), H_{ch} is the height of the channel, W_{ch} is the width of the channel, and $N_{f,t}$ is the number of features in the transverse direction. The width of the channel was 22 mm for every test piece. The cross sectional area is also defined at the maximum occlusion of the features as defined in (6.3).

$$A_{c,f} = H_{ch} \cdot W_{ch} - L_c \cdot H_f \cdot N_{f,t} \tag{6.3}$$

The friction factor is calculated based on the definition for flow over tube banks given by Zukauskas [82] and shown in (6.4).

$$f = \frac{2 \cdot \Delta P}{N_{f,l} \cdot \rho \cdot v_{\max}^2} \tag{6.4}$$

In (6.4), $N_{f,l}$ is the number of features in the transverse direction and ΔP is the pressure drop measured with the manometer. The maximum fluid velocity through the features is calculated using (6.5).

$$v_{\max} = \frac{\dot{V}}{A_{c,f}} \tag{6.5}$$

The uncertainty of the friction factor calculation is determined using the Kline and McClintock method. The full uncertainty equation is shown in (6.6). The uncertainty of length and width measurements is 0.01 mm. The maximum and minimum uncertainty for the friction factor calculation is 6.96% and 3.11% respectively. The average uncertainty is 5.16%.

$$\sigma_f = \left[\left(\frac{\partial f}{\partial H_{ch}} \sigma_{H_{ch}} \right)^2 + \left(\frac{\partial f}{\partial W_f} \sigma_{W_f} \right)^2 + \left(\frac{\partial f}{\partial H_f} \sigma_{H_f} \right)^2 + \left(\frac{\partial f}{\partial \dot{V}} \sigma_{\dot{V}} \right)^2 + \left(\frac{\partial f}{\partial \Delta P} \sigma_{\Delta P} \right)^2 \right]^{1/2} \tag{6.6}$$

6.4 Experimental Results

During the course of experimentation, it was discovered that tests eight and nine did not produce any measurable pressure drop across the features. These tests had the largest features and hydraulic diameter thus a small pressure drop is expected. However, the pressure drop was undetectable by the differential pressure manometer. In addition, the no-feature test piece had significant pressure drop that exceeded the limits of the differential pressure manometer. Therefore, test eight, test nine, and the no-feature test data was not recorded.

The measured pressure drop versus Reynolds number for each micro-hydrofoil array set for which data was available is presented in Figure 6.5. The graphs are grouped by the same S_t/L_c ratios, which also have the same characteristics lengths. Notice the tests with

the smallest characteristic lengths (which also corresponds to the smallest hydraulic diameter) have the largest pressure drop as expected. Test 6 had the largest pressure drop ranging from 2 to 7 kPa. Test 7 had the smallest measurable pressure drop ranging from 0.3 to 0.5 kPa.

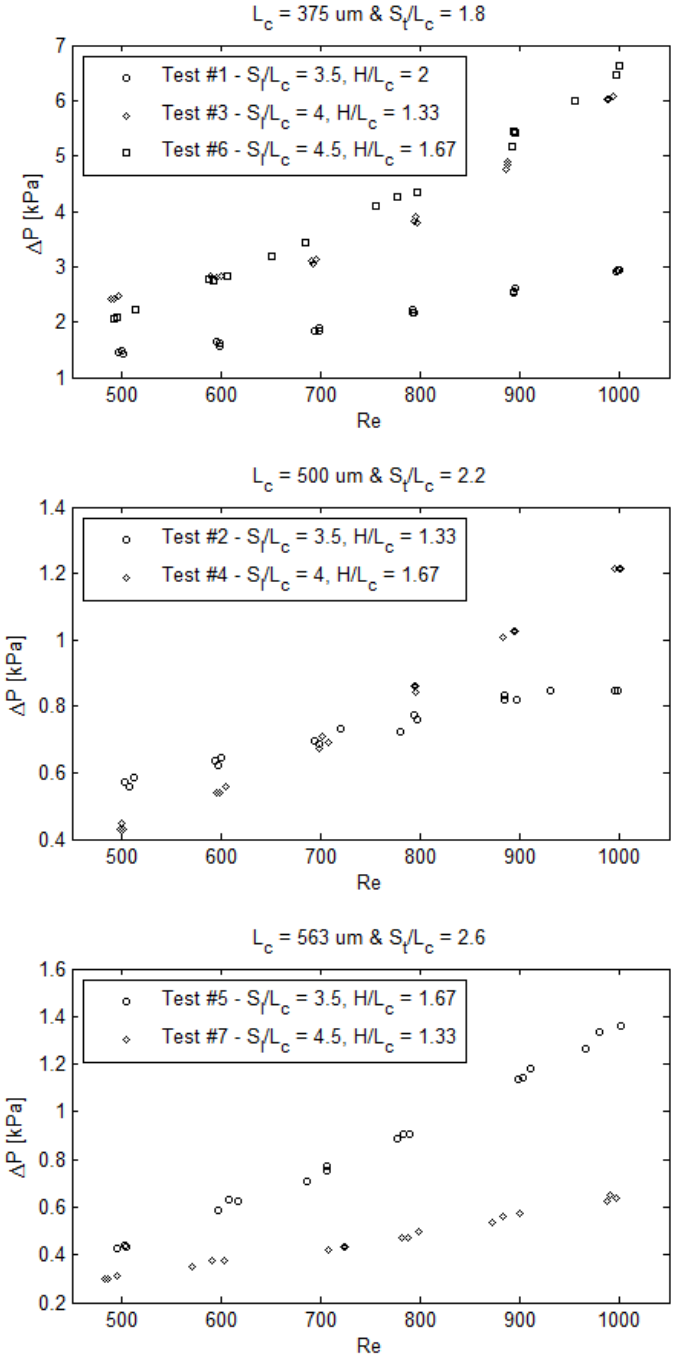

Figure 6.5 - Pressure drop vs. Re for all micro-hydrofoil tests

Three models were developed to correlate the geometries of the features and Reynolds number to the friction factor. The models were developed to compare the effectiveness of each model. The first model was presented by Short [74] and is presented in (6.7).

$$f = C\left(\frac{S_t}{L_c}\right)^{\beta_1}\left(\frac{S_l}{L_c}\right)^{\beta_2}\left(\frac{H}{L_c}\right)^{\beta_3}\mathrm{Re}^n \tag{6.7}$$

The equation can be linearized by taking the natural logarithm of the entire equation. This allows for easy determination of the coefficients through linear regression. The linearized form of this equation is seen in (6.8).

$$\ln(f) = \beta_1 A + \beta_2 B + \beta_3 C + nD + C^*$$

$$\textit{where,} \tag{6.8}$$

$$A = \ln\left(\frac{S_t}{L_c}\right),\ B = \ln\left(\frac{S_l}{L_c}\right),\ C = \ln\left(\frac{H}{L_c}\right),\quad \textit{and}\quad D = \ln(\mathrm{Re})$$

The resulting coefficients of the linear regression are presented in (6.9).

$$f = 2.8\left(\frac{S_t}{L_c}\right)^{0.52}\left(\frac{S_l}{L_c}\right)^{-0.58}\left(\frac{H}{L_c}\right)^{0.11}\mathrm{Re}^{-0.76} \tag{6.9}$$

The second model takes into account all possible interactions between the experimental parameters. This can be done because of the 3^{3-1} orthogonal testing array allows information about the testing interaction terms to be extracted from the data. However, since the order of the testing array was reduced to second-order, only up to second-order interactions can be included in the model. The possible interaction terms are displayed in (6.10).

$$\ln(f) = f\left(A, B, C, D, AB, AC, AD, BC, BD, CD, A^2, B^2, C^2, D^2\right) \tag{6.10}$$

The resulting coefficients of the linear regression are presented in (6.11). Notice that the coefficients in front of the first through third terms are zero. This means that in this model these terms are not significant, but rather the interaction terms are more significant.

$$\begin{aligned}\ln(f) = {} & 0 \cdot \ln\left(\frac{S_t}{L_c}\right) + 0 \cdot \ln\left(\frac{S_l}{L_c}\right) + 0 \cdot \ln\left(\frac{H}{L_c}\right) - 8.22 \cdot \ln(\mathrm{Re}) \\ & -8.84 \cdot \ln\left(\frac{S_t}{L_c}\right) \cdot \ln\left(\frac{S_l}{L_c}\right) + 7.16 \cdot \ln\left(\frac{S_t}{L_c}\right) \cdot \ln\left(\frac{H}{L_c}\right) - 0.016 \cdot \ln\left(\frac{S_t}{L_c}\right) \cdot \ln(\mathrm{Re}) \\ & -4.46 \cdot \ln\left(\frac{S_l}{L_c}\right) \cdot \ln\left(\frac{H}{L_c}\right) + 0.78 \cdot \ln\left(\frac{S_l}{L_c}\right) \cdot \ln(\mathrm{Re}) + 0.65 \cdot \ln\left(\frac{H}{L_c}\right) \cdot \ln(\mathrm{Re}) \\ & +6.17 \cdot \ln\left(\frac{S_t}{L_c}\right)^2 + 1.97 \cdot \ln\left(\frac{S_l}{L_c}\right)^2 - 2.78 \cdot \ln\left(\frac{H}{L_c}\right)^2 + 0.46 \cdot \ln(\mathrm{Re})^2 + 26.95\end{aligned} \tag{6.11}$$

The third model was developed using the same technique as the second model. A linear regression was run on every single possible combination of the testing parameters and their interactions. This process is detailed in appendix B. The results fits were screened and reduced to the models that had maximum percentage deviation from the actual data of less than 25%. The left over models were then screened for the fewest interactions while maintaining a low R^2/MSE value. The resulting model contained all of the experimental parameters and one interaction term. The coefficients of the linear regression for the third model are presented in (6.12).

$$\ln(f) = 37.84 \cdot \ln\left(\frac{S_t}{L_c}\right) + 23.36 \cdot \ln\left(\frac{S_l}{L_c}\right) + 0.57 \cdot \ln\left(\frac{H}{L_c}\right) - 0.75 \cdot \ln(\mathrm{Re}) - 24.95 \cdot \ln\left(\frac{S_t}{L_c}\right) \cdot \ln\left(\frac{S_l}{L_c}\right) - 31.51 \tag{6.12}$$

The percentage error between the model and the actual data for each of the three models is presented in Figure 6.6 Notice that the model developed by Short does not capture much of the data. This model has an R^2 value of 0.291 and 95% of the data falls within ± 33.4%. The second model has an R^2 value of 0.95 and 95% of the data falls within ± 8%. The third model has an R^2 value of 0.92 and 95% of the data falls within ± 10.2%. The third model offers the best tradeoff between accuracy and number of terms. A reduced number of interaction terms increases the model statistical significance.

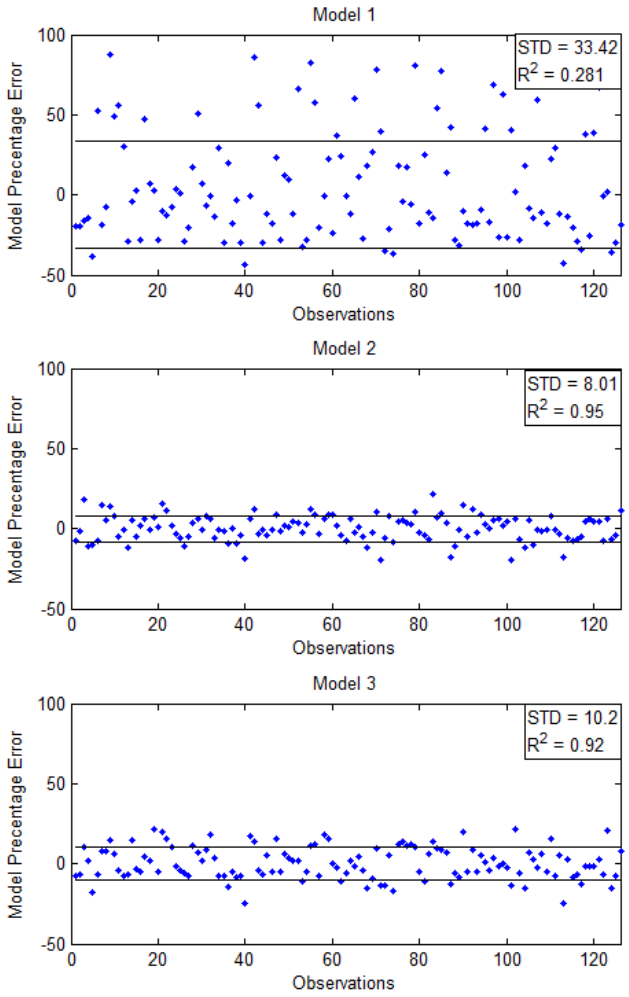

Figure 6.6 - Residuals plot for each friction factor model

The comparison of experimental friction factor to the third model prediction for all the hydrofoil tests is presented in Figure 6.7. This confirms that model successfully represents the experimental data for each test. Notice that the trends follow well for each test except for test 5 and 6. In addition, notice the test 6 has a lot of uncertainty. This uncertainty is due mostly to the low pressure drop through the test section and uncertainty in the flowmeter.

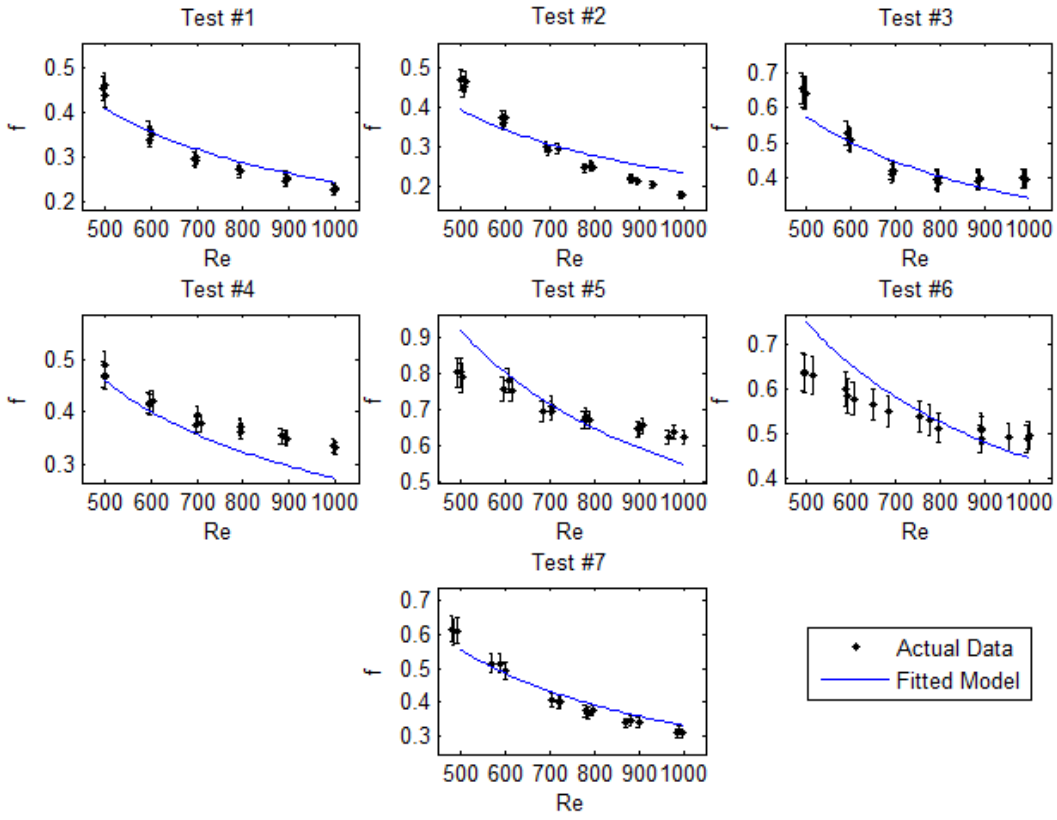

Figure 6.7 - Predicted model and experimental data for all tests

The pressure drop versus Reynolds number for the micro-stud test is presented in Figure 6.8. The pressure drop through this test section is higher than all the micro-hydrofoil tests except for test 3 and 6.

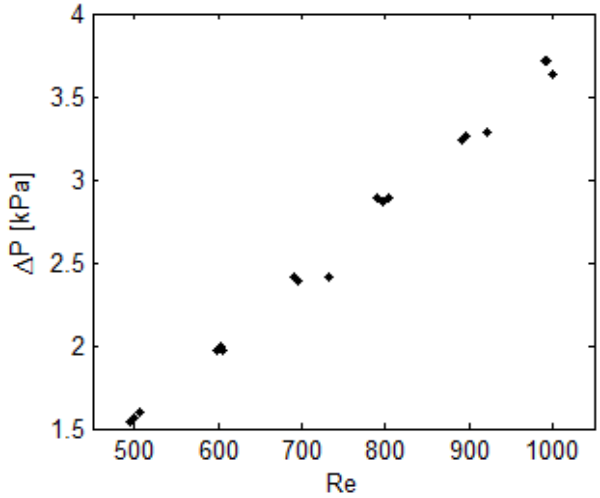

Figure 6.8 - Pressure drop for the micro-stud test

6.5 Optimal Design Methodology

A unified way of evaluating the tradeoffs between pressure drop and heat transfer in micro-feature enhanced heat exchangers (MFHX) does not exist. The significant pressure drop that accompanies the increase in heat transfer requires a larger pump and increased pumping power. In weight, volume, or power restricted applications a larger pump or increased pumping power is not acceptable. The authors provide a simple method for calculating the tradeoff between heat transfer and pressure drop. This method utilizes a MFHX "efficiency." This efficiency is based on the increase in heat transfer and pressure drop as compared to a baseline. The baseline is the heat transfer and pressure drop of a blank channel of the same base dimension as presented in (6.13).

$$\eta_{MFHX} = \frac{h_{MF}}{h_{blank}} + \frac{\Delta p_{blank}}{\Delta p_{MF}} \tag{6.13}$$

In (6.13), h_{MF} and Δp_{MF} is the heat transfer coefficient and the pressure drop of the MFHX. h_{blank} and Δp_{blank} is the heat transfer coefficient and pressure drop of a blank channel of the same base dimensions as the MFHX. The optimal MFHX will have a large heat transfer coefficient and comparable pressure drop as compared to a channel with no features. This methodology can be used to find the optimal feature geometries for a MFHX in any application. It should be noted that this formulation of the coefficient of performance places an equal importance of heat transfer gain and pressure drop loss. The formulation can be weighted to favor either the heat transfer or the pressure drop depending on the application.

6.6 Discussion

A direct comparison between the micro-stud test piece and any of the micro-hydrofoil test pieces is unfair, because the S_t/L_c, S_l/L_c, H/L_c, A_c, and D_h values do not equate. A weak comparison can be drawn between the micro-stud and micro-hydrofoil shapes by utilizing the proposed model. For this comparison the S_t/L_c, H/L_c, A_c, and D_h from the micro-stud array could be used to calculate the pressure drop for a micro-hydrofoil array using the proposed friction factor model. However, the same S_l/L_c between the micro-stud and the predicted micro-hydrofoil is not feasible due to the feature length increases in the flow direction. The reduced feature packing also precludes an equivalent total feature area between the micro-stud and micro-hydrofoil array. This effect can be reduced if the pattern was changed from aligned to staggered.

The comparison between the micro-stud test piece and predicted pressure drop for a micro-hydrofoil array with equivalent the S_t/L_c, H/L_c, A_c, and D_h is presented in Figure 6.9A. In this comparison, the Sl/Lc was set to 3.5, the lowest value from the testing matrix. Notice that the predicted micro-hydrofoil array has a ~7x reduction in pressure drop as compared to the micro-stud test piece at the highest Reynolds number. This can be attributed to the reduced feature packing of the predicted micro-hydrofoil array. The predicted featureless pressure drop is also included in Figure 6.9A. The featureless pressure drop was calculated using the standard pressure drop through a rectangular channel [23]. The featureless pressure drop is a 2.5x increase over the micro-stud test piece and a 20x increase over the predicted micro-hydrofoil array. Recall that this pressure drop could not be measured during the experimental because it exceeded the limits of the manometer.

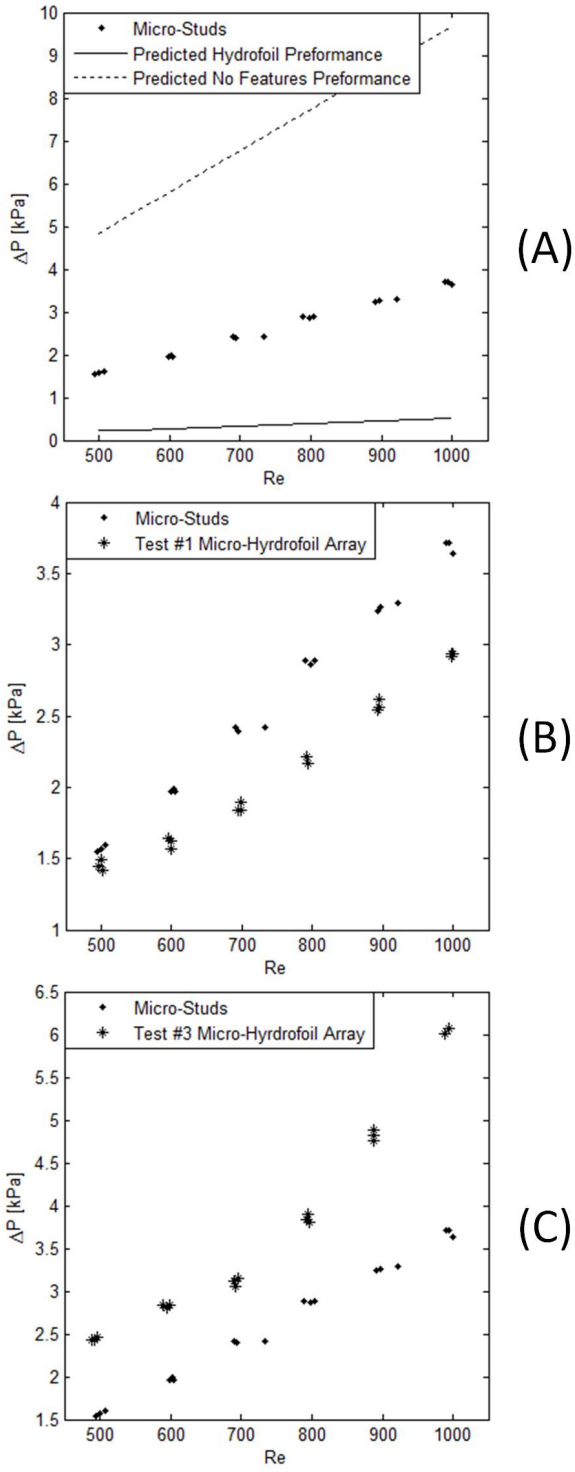

Figure 6.9 - Comparison of micro-stud experimental data to prediction of similar micro-hydrofoil including featureless prediction (A). Comparison of micro-stud and micro-hydrofoil with similar hydraulic diameter (B). Comparison of micro-stud and micro-hydrofoil with similar number of features (C)

A comparison between the micro-stud piece and the experimental data from the test with the closest hydraulic diameter can be made and is presented in Figure 6.9B. The hydraulic diameter of the micro-stud test piece is 0.66mm and the test 1 micro-hydrofoil piece is 0.57mm. Notice that even though test 1 has a smaller hydraulic diameter it has a lower pressure drop than the micro-stud piece. A comparison between the micro-stud piece and the experimental data from the test with the closest feature number of features can also be made and is presented in Figure 6.9C. The number of features in the micro-stud test piece is 800 and in the test 3 micro-hydrofoil piece is 780. Notice that even though test 3 has a lower number of features the micro-stud array has a lower pressure drop.

The proposed friction factor correlation can be recast as shown in (6.14).

$$f = 2.07E-14 \cdot \left(\frac{S_t}{L_c}\right)^{37.84} \left(\frac{S_l}{L_c}\right)^{23.36} \left(\frac{H}{L_c}\right)^{0.57} (\mathrm{Re})^{-0.75} e^{-24.95 \cdot \ln\left(\frac{S_t}{L_c}\right) \cdot \ln\left(\frac{S_l}{L_c}\right)} \tag{6.14}$$

Notice that, like in the proposed Nusselt number correlation, the correlation resembles Short's form multiplied by a correction term. Just as the proposed Nusselt number correlation, the correction term accounts for the three-dimensional effects present in the micro-feature array. However, the correction term in the friction factor correlation contains less geometric parameters than in the Nusselt number correlation. This is because the larger uncertainty and smaller data set does not allow for a more precise correlation by including more geometric interaction terms. However, the interactions terms that have been excluded and included do have fundamental significance. For instance, the interactions between the dimensionless feature height and the other dimensionless geometric parameters are accounted for in the hydraulic diameter. This

means the interactions that include the dimensionless feature height do not need to be included in the correction term. Furthermore, the interaction of the dimensionless transverse spacing and dimensionless longitudinal spacing could account for the continually converging and diverging flow associated with the varying hydraulic diameter along the length of the channel. More testing needs to be preformed to conclusively prove the impact of the interaction between dimensionless transverse spacing and dimensionless longitudinal spacing.

6.7 Summary

This chapter has detailed an empirical approach to developing a friction factor correlation for micro-hydrofoil arrays under single-phase cross flow. The test pieces were designed and manufactured in-house with advanced micro-milling technology. A test bench was developed to measure the pressure drop across the micro-feature arrays. Data reduction and uncertainty analysis was presented for the experimental data. Test 6 had the largest pressure drop ranging from 2 to 7 kPa. Test 7 had the smallest measurable pressure drop ranging from 0.3 to 0.5 kPa. Two models were developed using multi-linear regression and compared to an existing model. The existing model achieved an R^2 value of 0.291 with 95% of the data falling within ± 33.4%. The final correlation was selected based a third model that reduced the required number of terms as compared to the second model without sacrificing predictive power. The final friction factor correlation achieves an R^2 value of 0.92 with 95% of the data falling within ± 10.2%. The friction factor correlation developed in this study achieves a 3x reduction in prediction error for the micro-hydrofoil arrays.

CHAPTER 7

DESIGN AND OPTIMIZATION OF DIRECT WINDING COOLED SMPM ELECTRIC MACHINES

7.1 Introduction

This chapter details an integrated thermal-electromagnetic model for DWHX electric machines. This model is used in conjunction with particle swarm optimization (PSO) to perform initial sizing and infinite reservoir case studies. In the initial sizing case study, the torque density of the system was 23.2 N-m/L and the torque density based on electromagnetic volume was 66.8 N-m/L. In the infinite reservoir case study, the torque density based on motor volume was 48.9 N-m/L and 38.4 N-m/L for a fluid temperature of 20°C and 90°C respectively. The torque density based on electromagnetic volume was 105.7 N-m/L and 82.9 N-m/L for a fluid temperature of 20°C and 90°C respectively.

7.2 Review of Salient Literature

The coupling of thermal and electromagnetic simulations has not received significant attention in the reported literature to date. Lazarezic et al. [8] showed a coupling between magnetic equivalent circuit and a simplified thermal circuit. The magnetic circuit was used to calculate the losses that could then be simulated in the thermal circuit. Both circuits were calibrated using experimental data [8]. Similarly, Alberti et al. showed a coupled magnetic equivalent circuit and thermal circuit calibrated using FEA simulations [38]. Mezani et al. showed a combined approach that used an FEA electromagnetic simulation to calculate losses that were simulated in a thermal circuit [13]. Marignetti et al. used an FEA electromagnetic simulation to calculate losses that were then thermally simulated in an FEA simulation [31]. Dorrell et al. presented a combined analysis of an

induction machine using SPEED and MotorCAD [27]. SPEED [83] is an electromagnetic simulation software package that utilizes magnetic equivalent circuits. The authors simulated the induction machine in SPEED and through ActiveX were able to import the modeled machine directly into MotorCAD for thermal simulation. Most of these integrated models are empirically fit to the specific electric machine and are not useful is the design of advanced cooled electric machines.

An integrated thermal-electromagnetic design tool that accounts for advanced cooling technology does not exist. This chapter presents a novel advanced cooling technique. This chapter will use the methodology first proposed by Semidey, Mayor, Duan, and Harley that integrates an analytical electromagnetic design model with a parametric thermal model [84, 85]. The thermal model is updated to include the novel advanced cooling technology. This integrated advanced thermal-electromagnetic model is used in conjunction with an optimization technique to gain insights into the design of electric machines equipped with the novel cooling technique. The advanced cooling technology presented in this chapter represents an evolutionary leap forward in electric machine thermal management and design. This chapter describes the design challenges associated with the proposed advanced cooling technology as well as the integrated thermal-electromagnetic model. The integrated model, in conjunction with an optimization technique, is used in two case studies to access the system sizing.

7.3 DWHX Electric Machine Design Challenges

The DWHX electric machine was introduced in chapter 4 and some design challenges were identified. There are additional design challenges when the entire cooling system is considered such as dissipating the heat collected in the fluid to the ambient. This heat

rejection is typically done with a radiator. The size of the radiator depends on the temperature of the fluid, the temperature of the ambient, and the flowrate of the fluid. Increasing the fluid temperature and dropping the flowrate decreases the size of the radiator. If the fluid temperature is too high, the fluid could begin to boil and create system instabilities. The effects of radiator sizing must be included in the design of a DWHX electric machine.

Pump sizing is also an important design issue. A lower flowrate requires less pumping power leading to a small pump. Under these conditions, the system could potentially fail thermally. Conversely, a large flowrate reduces system temperatures but requires a larger pump thus increasing system size. The issues of DWHX feature design, radiator sizing, and pump sizing are addressed in the integrated thermal-electromagnetic model.

7.4 Integrated Thermal-Electromagnetic Simulation

An integrated thermal-electromagnetic design model was developed to meet the challenges of designing a DWHX electric machine. The design model consists of four modules. The first module is the electromagnetic module.

7.4.1 Electromagnetic Module

A detailed description of the proposed analytical design model has been presented in [86] by Duan et al. and the main idea is summarized here.

The analytical design model starts from the analytical calculation of the magnetic field solution in the air gap region. The radial component of the magnetic field in the air gap produced by the permanent magnet can expressed in a Fourier series as follows:

$$B_{gap-mag}(\theta, r) = \sum_{n=1,3,5...}^{\infty} B_n(r)\cos(\frac{np}{2}\theta) \tag{7.1}$$

where B_n is the n-th spatial harmonic component of the air gap flux density distribution, r is the air gap radius, θ is the angular position with reference to the center of a magnet pole and p is the number of poles.

After the stator bore diameter D, the machine axial length L, the air gap length g, the magnet thickness h_m, pole coverage and the magnetization are selected, magnitudes of the B_n (n=1,3,5…) in (2.1) can be calculated based on the analytical equations provided in [87]. The pole coverage and magnetization are selected to minimize the torque ripples and cogging torques, which is described in [88].

When the air gap flux density is calculated and the winding topology is determined, the back emf at rated condition can be calculated. Assuming the SMPM machines are designed to be inverter-driven and field-oriented control is applied, the rated current can be calculated for the specified output power.

With flux densities in the stator and rotor steel specified and current density in the winding coils chosen, the machine geometries as described in Figure 7.1 can all be calculated.

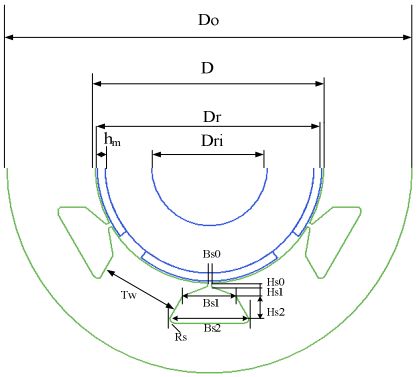

Figure 7.1 - SMPM machine geometry parameters[85]

In summary, the analytical design model requires only four input design parameters: the stator bore diameter D, the machine axial length L, the magnet thickness h_m, and the winding current density J. With the specified machine output power, the rated speed, rated frequency, excitation voltage and material information, the electromagnetic part of a SMPM machine can be fully designed. The machine performance is also calculated, including the active weight, volume and efficiency.

7.4.2 Thermal Module

A detailed description of the numerical thermal design module has been presented in chapter 2 and continued in chapter 4. A brief description is given here for reference. A parametric, self-meshing finite-difference (FD) technique has been constructed to model the spatial thermal response of electrical machines. The parametric technique calculates, numerically, the temperature distribution throughout a one-half slot model of the stator. This technique begins by distributing calculation nodes throughout the simplified stator geometry as seen in Figure 7.2 using a "center node" distribution approach expressed in polar coordinates. An automated segmentation approach then captures the geometry of the stator teeth, back iron, windings and estimated air resulting from under fill in the windings. However, many stator geometries have features that do not correspond to either a radius or an angle in polar coordinates. To create a generic model the technique therefore represents the actual slot geometry by features that correspond to either a radius or an angle. This allows any slot geometry to be fully described in a parametric manner using only the nine dimensions as shown in Figure 7.2. The model mesh can then be generated and segmented according to the parametric parameters that describe the actual

stator slot geometry. The method of conversion between actual stator slot geometry and the parametric parameters can been seen in chapter 2.

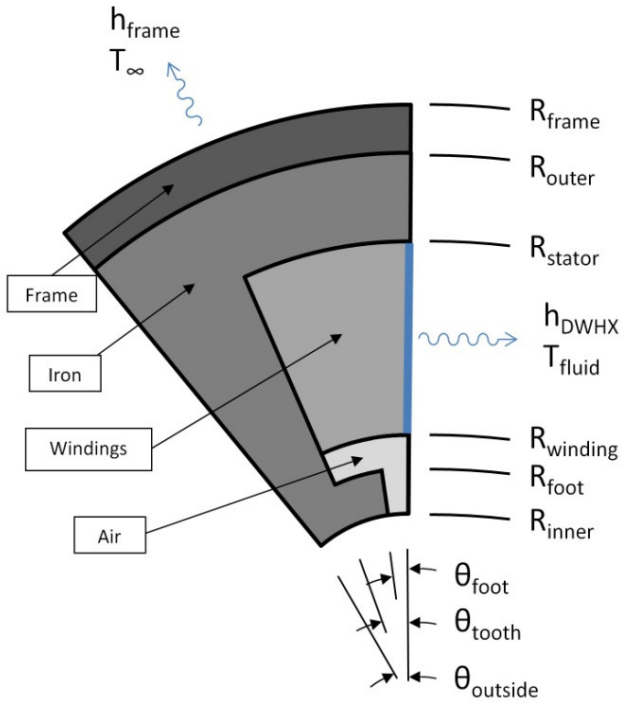

Figure 7.2 - The thermal modeling approach considers a parametric half-slot model of the stator that is fully described by nine geometric parameters: six radii and three angles, and four thermal boundary conditions.

Next, an energy conservation equation is written for each node that accounts for all energy entering, exiting, generated, and stored in the node. These equations can then be solved simultaneously using matrix inversion to determine the temperature at each node. The DWHX heat exchanger is modeled as a convective boundary condition. The convective is applied at the boundary of the windings in the half slot model as illustrated in Figure 7.2. The temperature of the fluid is assumed to be the maximum temperature is the fluid loop. The heat transfer coefficient of the DHWX is calculated using the correlation developed in chapter 5 and detailed in the next section.

In Chapter 2 a mesh convergence study was presented demonstrating that a 100,000 node mesh minimizes numerical errors as compared to an ultra-fine mesh baseline solution. The computational time at 100,000 nodes is 1.1s. A PSO optimization using 32 particles for 250 epochs requires 8,000 discrete simulations. The optimization would take 2.2 hours to compute just the thermal simulation with 100,000 nodes. To reduce the computational time, a similar convergence study to the one presented in Chapter 2 was performed to investigate reducing computational time. In this convergence study, the difference in maximum winding temperature between the course mesh solution and fine mesh solution was investigated under the same cases. The thermal performance of the electric machine is characterized solely by insulation life determined by the maximum winding temperature. The results from the study are display in Figure 7.3. The maximum temperature is within ±0.5°C at 25,000 nodes as compared to the fine mesh solution. This reduces the computation time to 0.27s as compared to a mesh with 100,000 nodes. For 8,000 simulations, the computation time for the thermal simulations reduces to 36 minutes without sacrificing maximum winding temperature accuracy.

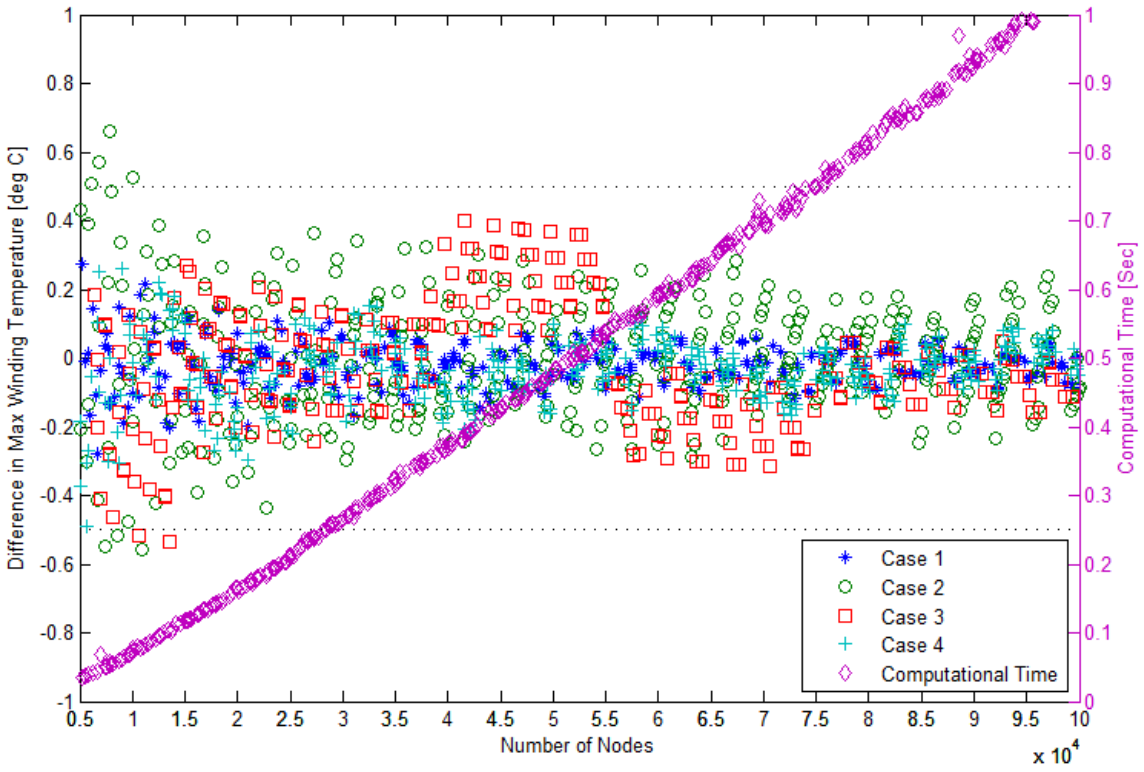

Figure 7.3 - Difference in maximum winding temperature between course mesh solutions and a fine mesh solution with two million nodes along with computation time

7.4.3 DWHX selection Module

The selection of the DWHX geometries is a critical part in the design of a DWHX electric machine. In this study, the micro-hydrofoils are NACA 0040 hydrofoils and are described by the characteristic polynomial for the hydrofoil. The hydrofoil array is described by the transverse spacing (S_t), longitudinal spacing (S_l), characteristic length (L_f), feature height (H_f), and channel height (H_{ch}) as illustrated in Figure 7.4. These geometric relationships have a direct impact on thermal performance. For instance, a dense packing of features would have high heat transfer characteristics but significant pressure drop. Conversely, scarce packing of features would not improve the heat transfer as compared to a meso-channel with no features.

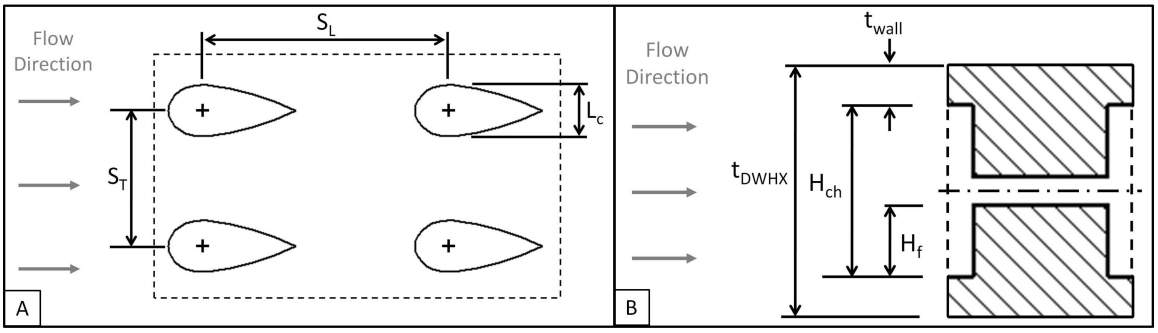

Figure 7.4 - Unit cell of micro-hydrofoil array (A). Cross section of micro-hydrofoil array height (B)

To assess the tradeoff of between heat transfer and pressure drop the authors have developed a definition of DWHX efficiency as presented in chapter 6. This efficiency compares the thermal and flow performance of a micro-hydrofoil enhanced DWHX to a DWHX with a blank (no micro features) meso channel of the same dimensions. This formulation is shown in (7.2).

$$\eta_{DWHX} = \frac{h_{hydrofoil}}{h_{blank}} + \frac{\Delta p_{blank}}{\Delta p_{hydrofoil}} \tag{7.2}$$

In (7.2), $h_{hydrofoil}$ and h_{blank} are the heat transfer coefficients of the micro-hydrofoil array and the blank meso-channel respectively. Δp_{blank} and $\Delta p_{hydrofoil}$ are the pressure drops of the micro-hydrofoil array and the blank meso-channel respectively. The convective heat transfer coefficient for the nominal black mesochannel, h_{blank}, is calculated using the standard Nu correlation for rectangular flow geometries [34] using (7.3).

$$h_{blank} = \frac{Nu \cdot k_{fluid}}{D_{h,blank}} \tag{7.3}$$

In (7.3), Nu is the Nusselt number for the meso channel [34], k_{fluid} is the thermal conductivity of the fluid and $D_{h,blank}$ is the hydraulic diameter of the meso-channel. The hydraulic diameter of the meso-channel is shown in (7.4).

$$D_{h,blank} = \frac{4 \cdot H_{ch} \cdot W_{ch}}{2 \cdot H_{ch} + 2 \cdot W_{ch}} \tag{7.4}$$

In (7.4), H_{ch} is the height of the meso-channel (smaller dimension in the flow direction) and W_{ch} is the width of the meso-channel. The height of the meso-channel is calculated from (7.5).

$$H_{ch} = t_{DWHX} - 2 \cdot t_{wall} \tag{7.5}$$

In (7.5), t_{DWHX} is the overall thickness of the DWHX and t_{wall} is the wall thickness of the DWHX. Both of these values must be specified by the designer. The pressure drop of the blank meso-channel is calculated using the Hagen–Poiseuille description of pressure drop through a rectangular channel as shown in (7.6).

$$\Delta p_{blank} = \frac{L \cdot 12 \cdot \mu \cdot \dot{V}}{H_{ch}^3 \cdot W_{ch}} \tag{7.6}$$

In (7.6), L is the length of the flow channel in the flow direction, μ is the dynamic viscosity, and $\dot{V}$ is the volumetric flowrate through the channel. The heat transfer coefficient for the micro-hydrofoil arrays is calculated with (7.7).

$$h_{hydrofoil} = \frac{Nu_{hydrofoil} \cdot k_{fluid}}{D_{h,hydrofoil}} \tag{7.7}$$

The Nusselt number associated with the micro-hydrofoil arrays is calculated using the correlation developed in chapter 5 and presented in (7.8).

$$\begin{aligned} Nu_{hydrofoil} = \exp\Bigg(& 17.04 \cdot \ln\left(\frac{S_t}{L_c}\right) + 4.59 \cdot \ln\left(\frac{S_l}{L_c}\right) - 5.85 \cdot \ln\left(\frac{H_f}{L_c}\right) + 0.272 \cdot \ln(\mathrm{Re}) \\ & - 7.17 \cdot \ln\left(\frac{S_t}{L_c}\right) \cdot \ln\left(\frac{S_l}{L_c}\right) + 4.53 \cdot \ln\left(\frac{S_l}{L_c}\right) \ln\left(\frac{H_f}{L_c}\right) - 3.15 \cdot \ln\left(\frac{S_t}{L_c}\right)^2 - 9.02 \Bigg) \end{aligned} \tag{7.8}$$

In (7.8), S_t, S_l, H_f, and L_c were defined previously and illustrated in Figure 7.4 and Re is the Reynolds number for the micro-hydrofoil array as defined in (7.9).

$$\mathrm{Re} = \frac{\dot{V} \cdot D_{h,hydrofoil} \cdot \rho_{fluid}}{A_{c,features} \cdot \mu_{fluid}} \tag{7.9}$$

In (7.9), ρ_{fluid} is the density of the fluid. The hydraulic diameter of the micro-hydrofoil array is defined in (7.10) and the cross sectional area of the micro-hydrofoil arrays in the flow direction is defined in (7.11).

$$D_{h,hydrofoil} = \frac{4\left(H_{ch} \cdot W_{ch} - L_c \cdot H_f \cdot N_f\right)}{2 \cdot H_{ch} + 2 \cdot W_{ch} + 2 \cdot H_f \cdot N_{f,t}} \tag{7.10}$$

In (7.10), $N_{f,t}$ is the number of micro-hydrofoil features in the transverse direction.

$$A_{c,features} = H_{ch} \cdot W_{ch} - L_c \cdot H_f \cdot N_{f,t} \tag{7.11}$$

The pressure drop across the micro-hydrofoil array is shown in (7.12).

$$\Delta p_{hydrofoil} = \frac{L \cdot f^*}{D_{h,hydrofoil}} \cdot \frac{1}{2} \cdot \rho_{fluid} \cdot v^2 \tag{7.12}$$

In (7.12), v is the mean velocity defined as the volumetric flowrate divided by the cross sectional area of the micro-hydrofoil array in the flow direction. The friction factor, f^*, is calculated using the correlation developed in chapter 6, defined in (7.13).

$$\begin{aligned} f^* = \exp\Bigg(& 37.84 \cdot \ln\left(\frac{S_t}{L_c}\right) + 23.36 \cdot \ln\left(\frac{S_l}{L_c}\right) + 0.57 \cdot \ln\left(\frac{H_f}{L_c}\right) - 0.75 \cdot \ln(\mathrm{Re}) \\ & - 24.95 \cdot \ln\left(\frac{S_t}{L_c}\right) \cdot \ln\left(\frac{S_l}{L_c}\right) - 31.51 \Bigg) \end{aligned} \tag{7.13}$$

The optimal set of micro-hydrofoil array geometries (S_t/L_c, S_l/L_c, H_f/L_c) maximizes the DWHX efficiency defined in (7.2). These geometries are obtained by first evaluating the efficiency of all geometry sets that are feasible. Feasibility of a geometry set is first defined by the feasible ratios of S_t/L_c, S_l/L_c, and H_f/L_c. The feasible ratios are defined as the applicable range of the correlations. The applicable ranges are shown in Table 7.1.

Table 7.1 - Feasible micro-hydrofoil array geometric ratios

Ratios	Min Value	Max Value
S_t/L_c	1	3
S_l/L_c	3	5
H_f/L_c	1	2.5
L_c [mm]	0.2	1

Second, the feasibility is of the feature height and longitudinal spacing is accessed. The height of the features can never be larger the half of the channel height. In addition, the longitudinal spacing, S_l, has to be large enough so the hydrofoils do not overlap in the longitudinal direction. These two constraints are defined in (7.14) and (7.15) respectively.

$$H_f < \frac{H_{ch}}{2} \tag{7.14}$$

$$S_l > c + S_t - L_c \tag{7.15}$$

In (7.15), c is the length of the chord of the hydrofoil, which is defined as the characteristic length divided by the thickness ratio. The thickness ratio for the defined hydrofoils is 0.4. The efficiency of each feasible geometry set is then calculated. Following this calculation, the maximum efficiency from the all feasible geometry sets is identified. The geometry set with the maximum efficiency is then reported. The thickness of the DHWX, t_{DWHX} , and the thickness of the wall, t_{wall} , are determined by the designer.

7.4.4 Radiator and Pump Sizing Module

The volume of the radiator and the pump is another critical system design component. The temperature drop across the radiator is illustrated in Figure 7.5. The fluid temperature approaches the ambient temperature as the fluid travels along the length of the radiator. At steady state, the temperature drop across the radiator is equal to the temperature rise across the DWHXs in the machine. The temperature rise across the DWHXs in the machine is a function of the loss in the machine and the flowrate through the system. The maximum fluid temperature in the DWHXs is considered the inlet temperature to the radiator.

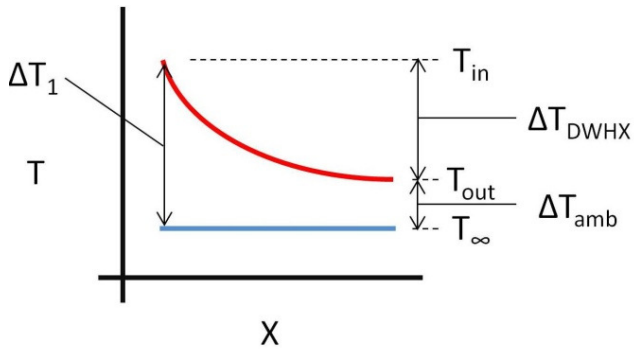

Figure 7.5 - Fluid temperature profile across a radiator with a fixed ambient temperature

The simplest way to define the radiator sizing is by specifying two temperature differences. The first is the temperature difference from the outlet of the radiator to the ambient temperature, ΔT_{amb}. The second is the temperature increase across the DWHXs, ΔT_{DWHX}. The mass flowrate through the system is calculated from ΔT_{DWHX} using (7.16).

$$\dot{m} = \frac{P_{copper}}{C_{p,fluid}\Delta T_{DWHX}} \tag{7.16}$$

In (7.16), $C_{p,fluid}$ is the specific heat of the fluid. This formulation assumes that all of the copper loss, P_{copper}, goes into heating the fluid. Using manufacturer's data the thermal resistance per unit volume of the radiator can be calculated from mass flowrate as shown in (7.17).

$$R'''_{rad} = 0.0199 \cdot \exp\left(-21.437 \cdot \dot{m}\right) + 0.03898 \tag{7.17}$$

(7.17) was derived by collapsing manufacturer's data from [89]. This type of radiator is a forced cooled air exchanger. The volume of the radiator is then calculated using (7.18).

$$V_{rad} = \frac{P_{copper} \cdot R'''_{rad}}{\Delta T_{lm}} \tag{7.18}$$

where the log mean temperature is defined in (7.19),

$$\Delta T_{lm} = \frac{\left(T_{out} - T_{\infty}\right) - \left(T_{in} - T_{\infty}\right)}{\ln\left(\left(T_{out} - T_{\infty}\right) \Big/ \left(T_{in} - T_{\infty}\right)\right)} \tag{7.19}$$

In (7.19), the inlet and the outlet temperatures are defined in (7.20) and (7.21) respectively. In these equations T_{∞} is the ambient temperature.

$$T_{in} = T_{\infty} + \Delta T_{DWHX} \tag{7.20}$$

$$T_{out} = T_{\infty} + \Delta T_{amb} \tag{7.21}$$

The size of the pump is a linear function of the required pumping power as defined in (7.22).

$$V_{pump} = 8.8642e-4 \cdot P_{pump} \tag{7.22}$$

(7.22) was derived by collapsing the manufacturer's data from [89]. The pumping power is calculated using (7.23).

$$P_{pump} = \frac{\dot{V} \cdot \Delta p}{\eta_{pump}} \tag{7.23}$$

In (7.23), Δp is the pressure drop through the system and η_{pump} is the efficiency of the pump. The pressure drop through the system in calculated using (7.24).

$$\Delta p = \left(\Delta p_{rad} + \Delta p_{DWHX} \cdot Nm\right) \cdot \eta_{\min or} \tag{7.24}$$

In (7.24), Δp_{rad} is the pressure drop through the radiator, Nm is the number of stator slots, and $\eta_{\min or}$ is the minor loss coefficient. The coefficient accounts for all minor pressure losses through the system. The pressure drop through the radiator is calculated using (7.25).

$$\Delta p_{rad} = \left(0.1314 \cdot \left(60.3 \cdot \dot{m}\right)^2 + 0.501\right) \cdot V_{rad} \tag{7.25}$$

(7.25) was derived by again collapsing the manufacturer's data from [89]. These equations show that the volume of the radiator and pump are functions of ΔT_{amb}, ΔT_{DWHX} and T_∞. T_∞ is a constraint based on the specification of the designer.

7.5 Integrated Simulation and Optimization Function

The electromagnetic module requires the selection of many design parameters such as stator bore diameter, air gap length, slot fill factor, etc. However, four parameters have been previously identified as the parameter to optimize. These parameters are the stator bore diameter, D_{ag}, the machine active length, L_{active}, the magnet thickness h_m, and the current density J. All other parameters are selected based on recommendations from the electromagnetic design team.

The thermal module requires the selection of ambient temperature, thickness of DWHX, DWHX wall thickness, and the temperature differences ΔT_{amb}, and ΔT_{DWHX}. The ambient temperature is selected by the designer based on desired operating conditions. The selection of DHWX thickness and wall thickness is based on the manufacturability of the heat exchanger. Electromagnetically, the optimal DHWX would have minimal thickness. Therefore, the thicknesses need to be selected based on the minimum size manufacturable. ΔT_{amb} and ΔT_{DWHX} are parameters that drastically affect system size; therefore, these parameters are to be optimized.

The integrated thermal-electromagnetic simulation is illustrated in Figure 7.6. The red boxes correspond to the inputs and outputs from the integrated model. The green boxes correspond to optimization constraints that are determined by the designer. The orange box corresponds to the DWHX, radiator, and pump sizing module. The purple box

corresponds to the DWHX electric machines thermal simulation. The sections within the dotted line correspond to the thermal simulations.

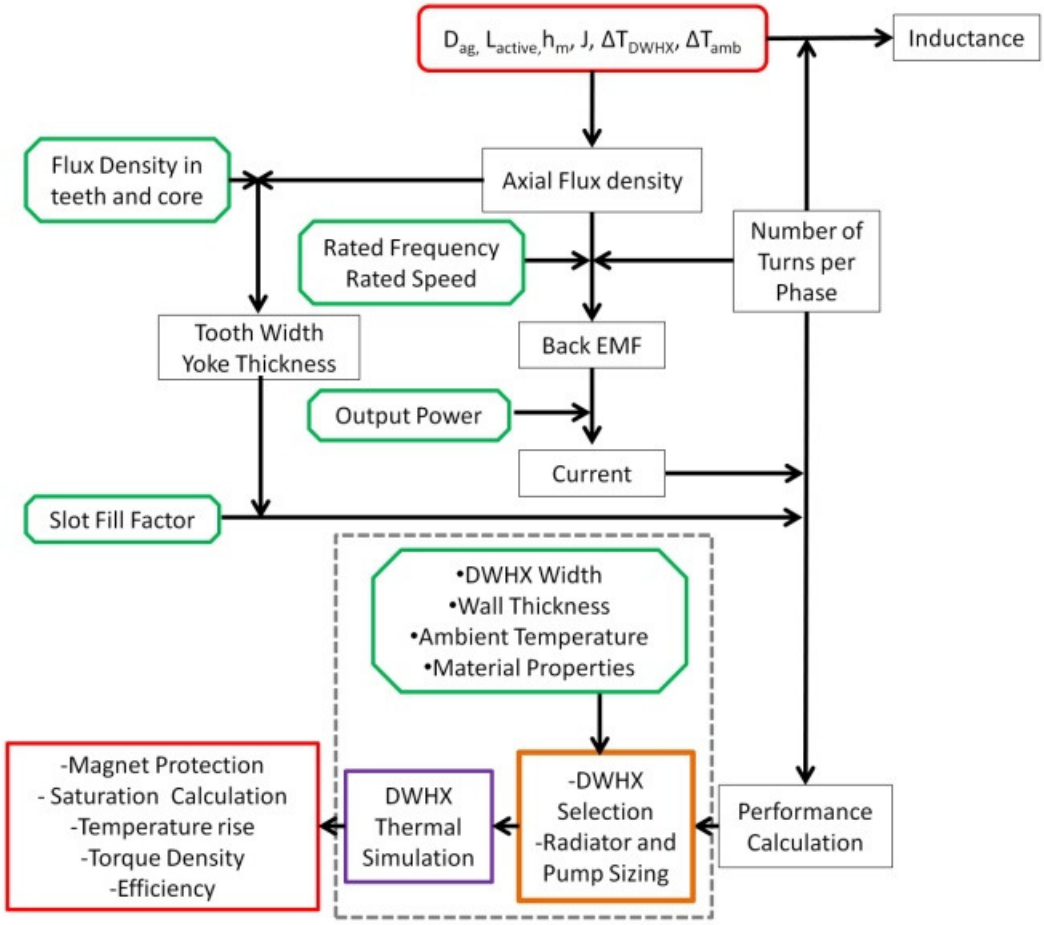

Figure 7.6 - Integrated thermal-electromagnetic simulation flow chart

7.5.1 Formulation of Objective Function

An objective function must be formulated before the optimization can begin. The fitness function, f, defined by the authors is shown in (7.26). This formulation considers the tradeoff between torque density (Nm/L) versus system efficiency.

$$f = \left(1 - \frac{\rho_{torque}}{\rho^{*}_{torque}}\right) \cdot 100 + \left(1 - \eta_{system}\right) \cdot 100 + \phi_{tot} \tag{7.26}$$

In (7.26), ρ^{*}_{torque} is a desired torque density, ρ_{torque} is the torque density if the system, η_{system} is the system efficiency, and ϕ_{tot} is the sum of all penalties. The torque density of the system is defined in (7.27).

$$\rho_{torque} = \frac{T}{V_{rad} + V_{pump} + V_{motor}} \tag{7.27}$$

In (7.27), T is the torque produced by the machine. The system efficiency is calculated using (7.28).

$$\eta_{system} = \frac{P_{out}}{P_{out} + P_{pump} + P_{core} + P_{copper}} \tag{7.28}$$

In (7.28), P_{out} is the designed output power and P_{core} is the core loss. The penalties are calculated using (7.29).

$$\phi_{tot} = 10{,}000\left(\phi_{sat} + \phi_{dmgr} + \phi_{dmgs} + \phi_{temp}\right) \tag{7.29}$$

In (7.29), ϕ_{sat} is the penalty for armature reaction, ϕ_{dmgr}, is the penalty for demagnetization at rated condition, ϕ_{dmgs} is the penalty for demagnetization at shorted condition, and ϕ_{temp} is the penalty for insulation life. The formulation of these penalties are detailed in [85]. The thermal penalty is detailed here for completeness. The penalty function for temperature rise is defined as

$$\phi_{temp} = \max\left(\frac{L_{EX} - L_T}{L_{EX}}, 0\right) \tag{7.30}$$

In (7.30), L_{EX} is the expected winding insulation life. For example, if a class B winding insulation is used and the expected insulation life is 20,000 hours, the value of ϕ_{temp} is

plotted in Figure 7.7 where L_T is defined by (7.31). In (7.31), T is the maximum insulation temperature for the thermal simulation.

$$L_T = 10000 \cdot 10^{-0.03(T-140)} \tag{7.31}$$

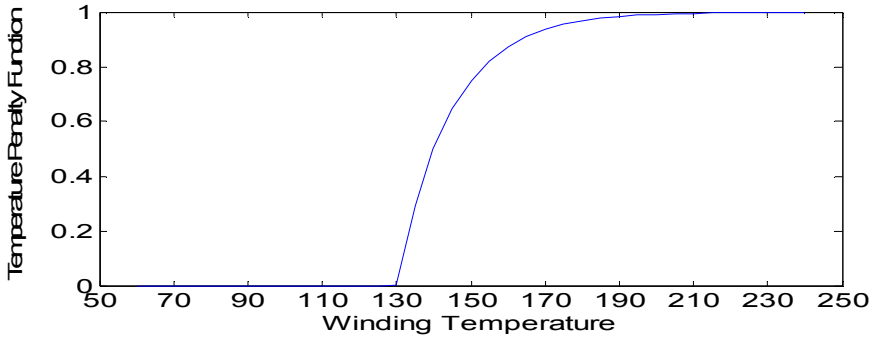

Figure 7.7 - Plot of ϕ_{temp} for insulation class B and L_{EX} = 20000 hours[85]

7.6 Optimization Case Studies

Two case studies were preformed to assess sizing of a DWHX electric machine. The first case study was used to understand the tradeoffs between motor sizing and radiator sizing. The second case study was performed to assess the size of the DWHX electric machine when considering an infinite thermal reservoir.

7.6.1 Implementation of Optimization Technique

The integrated thermal-electromagnetic model was combined with an optimization technique to perform the case studies. There are several nonlinear global optimization techniques that could be utilized to find the optimal DWHX electric machine geometries such as Simulated Annealing, Evolutionary Algorithms, Branch and Bound etc [90]. The non-linearity and some discontinuous variables in the electromagnetic module limit the potential optimization techniques to particle swarm optimization (PSO) and genetic

algorithms (GA) [91, 92]. It has been shown in that PSO outperforms GA in [92] and a separate study is detailed in Appendix D.

PSO was first introduced by Kennedy and Eberhart and is based on swarm theory that mimics the movement of a flock of birds or a school of fish [93, 94]. The movement of the particle through the solution hyperspace is governed by a stochastic weighted sum of the previous velocity, velocity to the local best solution, and velocity to the global best solution. This technique has recently gained popularity due to its speed, accuracy, and ease of implementation.

The PSO algorithm was implemented in Matlab R2009b using the formulation given in [95]. A constriction method was used for the inertia-weighting coefficient. The inertia-weighting coefficient began at 0.8 and reduced by 0.1, every 50 epochs, culminating at 0.4. The convergence criterion in this study was set such that the standard deviation of the particle locations was less than 0.1. The algorithm utilized the built-in Matlab parallel computing toolbox. The parallel computing toolbox in Matlab uses each core as a separate processor allowing for parallel computing leading to faster computation times. The computer used had an AMD Phenom Quad-Core 2.3 GHz processor with 8 GB of RAM. The PSO algorithm was implemented using 32 particles and typically converged after 250 epochs taking 1.5 hours to complete.

7.6.2 Optimization Specs

The specifications for the DWHX electric machine in each case study are summarized in Table 7.2. The key specifications are 20 kW of power at 53 N-m with an ambient temperature of 25°C.

Table 7.2 - DWHX electric machine specification list

Specification	Value	Units
Power	20	kW
Speed	3600	RPM
Torque	53	N-m
Voltage	240	VAC
T_{inf}	25	C
Desired Torque Density	10	N-m/L
Frame Material	Aluminum	-

Several key parameters must be determined by the designer as previously identified. The constraints used in the case studies are presented in Table 7.3. The first five constraints are thermal-mechanical constraints. The wall and overall thickness of the DWHX were set based on micro-manufacturing limits determined through the authors' experience. The thickness of the frame is typically used to increase the ambient rejection area of the machine. In a DWHX electric machine, this extra area is not needed, so the frame thickness is set by manufacturing limits determined by the authors. The effective thermal conductivity of the windings is normally low (<1 W/m-k) because of a low thermal conductivity filler material (typically air). However this study uses a correlation developed by Kanzaki et al [37] and shown in chapter 4. The correlation was used with a packing factor of 0.75 and thermally conductive epoxy as the filler material. The thermal conductivity of the thermally conductive epoxy is 5 W/m-k. The contact resistance is set as a conservative estimate from typical values [34].

Table 7.3 - DWHX electric machine optimization constraints

Constraints	Value	Units
t_{wall}	0.5	mm
t_{DWHX}	2	mm
t_{frame}	3	mm
$k_{windings}$	32.5	W/m-k
Contact Resistance	0.001	m^2-K/W
Fill Factor	0.75	-
Number of Poles	4	-
Slots per phase per pole	1	-
Air Gap Length	0.4	mm
Saturation	2.4	T

The optimization variables have been presented in Figure 7.6. The optimization variable domains used in the case studies are presented in Table 7.4. Note that the typical current densities range for 3-12 A/mm^2, but the DWHX cooling technique could allow for much higher current densities. The domain for the height of the magnets was set based on typical magnet sizes.

Table 7.4 - DWHX electric machine optimization domain

Variable	Domain	Units
D	30 - 100	mm
L	30 - 100	mm
h_m	5 - 15	mm
J	5 - 30	A/mm^2
ΔT_{DWHX}	.1 - 110	°C
ΔT_{amb}	10 - 110	°C

7.6.3 Initial Sizing with Integrated Radiator Case Study

In many applications, the total system volume is critical. One can just not consider the electromagnetic volume, but must consider the total motor, radiator, and pump volume. This case study was performed to understand the tradeoffs between total motor volume, radiator volume, and total system volume. In this case study the temperature difference

from the outlet of the radiator to the ambient (ΔT_{amb}) was fixed. An optimization was performed at the fixed ΔT_{amb} and the other optimization variables were optimized. This was performed for a range of ΔTamb starting at 10°C and ending at 110°C. The optimization was replicated three times to ensure the optimal solution was found at each ΔTamb. The results from the case study are displayed in Figure 7.8. The figure shows the volume of the left hand axis and the efficiency on the right hand axis for each fixed ΔT_{amb}.

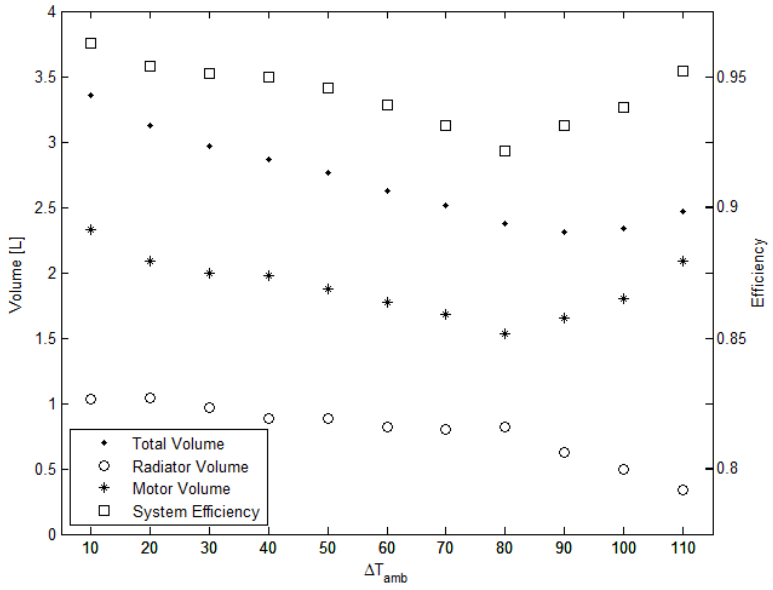

Figure 7.8 - Volume and efficiency vs. ΔT_{amb} for the initial sizing case study

Several trends can be inferred from the results of this case study. First as ΔT_{amb} increases the system volume gets smaller until the ΔT_{amb} reaches 100°C. At 100°C, the system volume begins to increase. The driving force for radiator heat rejection is ΔT_{lm}, which was defined in (7.19). The inlet temperature to the radiator is limited by the thermal limit of the windings. As ΔT_{amb} increases, ΔT_{lm} increases until the thermal limit of the winding is reached leading to the inflection at 100°C. Also, notice the radiator

volume is a weak function of ΔT_{amb} between 10°C and 80°C. The efficiency of the machine trends with the volume of the motor, which is to be expected.

The fitness function values for each of the optimization trials are shown in Table 7.5. The optimization was run several times to ensure the global minimum was reached. For each of the optimization trials the fitness function was within 5% of the other trials.

Table 7.5 - Fitness Function values for each trial in initial sizing with radiator case study

	ΔT_{amb}										
	10	20	30	40	50	60	70	80	90	100	110
Trial #	Fitness Function Value										
1	-55.8	-66.6	-75.9	-83.0	-88.4	-97.1	-107.8	-112.7	-124.9	-123.1	-112.8
2	-55.1	-66.7	-75.9	-83.1	-88.4	-98.3	-104.8	-117.4	-124.9	-123.1	-110.5
3	-55.7	-66.7	-75.8	-82.1	-88.4	-98.3	-107.3	-117.4	-123.9	-123.1	-111.8

The result from each optimization for the best case for each is displayed in Table 7.6. The optimal DWHX electric machine based on the constraints and fitness function previously defined is located at a ΔT_{lm} of 90°C. At this condition, the torque density of the system is 23.2 N-m/l and the torque density based on electromagnetic volume is 66.8 N-m/L. Note that the maximum torque density based on electromagnetic volume is 72.5 N-m/L and happens at a ΔT_{lm} of 80°C. The radiator is 33% larger than at the optimal condition. Also, notice that the current densities range from 6.7 to 14.1 A/mm2. It was expected that the current densities in the DWHX electric machine would be much higher. However, the optimization found high torque dense solutions at normal current densities thus increases efficiencies. This happened because decreasing the efficiency increases thermal losses thus increasing radiator volume. It should be noted that for all optimizations the optimal magnet thickness was 15mm. This suggests that the magnet thickness could increase, but this would bring into question manufacturing limits.

Table 7.6 - Optimization Results for all cases from the ΔT_{amb} initial sizing case study

	ΔT_{amb} [°C]										
	10	20	30	40	50	60	70	80	90	100	110
D [mm]	87.9	85.6	86.1	86.2	87.2	87.7	84.6	85.9	88.5	81.1	83.5
L [mm]	38.9	40	37.5	36.6	33.5	30.8	34.5	30	27.7	40	40.9
J [A/mm2]	6.7	9.1	8.7	10	10.1	10.4	13.5	14.1	9.6	12.7	10
ΔTDWHX	104.3	89.1	76.6	65.8	52.2	2	2.2	2.6	2.2	1.7	1.2
EM Torque Density [N-m/L]	47.4	53.1	55.4	55.9	59.0	62.5	66.1	72.5	66.8	61.6	53.2
Total Torque Density [N-m/L]	15.9	17.1	18.1	18.7	19.4	20.4	21.3	22.5	23.2	22.9	21.8
Efficiency	0.96	0.95	0.95	0.95	0.95	0.94	0.93	0.92	0.93	0.94	0.95
Fitness Value	-55.8	-66.6	-75.9	-83.0	-88.4	-98.3	-107.8	-117.4	-124.9	-123.1	-112.8

The optimal micro-hydrofoil array characteristic dimensions for the optimal DWHX electric machine in this case study are presented in Table 7.7. These geometries should be used to make the optimal micro-hydrofoil array for this specific machine indentified by the optimization.

Table 7.7 - Optimal micro-hydrofoil geometries from best case in initial sizing case study

ΔT_{amb} [°C] = 90			
S_t/L_c	2.3	L_c [mm]	0.2
S_l/L_c	5	$N_{f,t}$	61
H/L_c	2.5	$N_{f,l}$	27

7.6.4 Infinite Reservoir Case Study

Some applications have an infinite thermal reservoir built into the system. An example of such an application would be an IC engine coolant system or fluid from a large body of water that are found on a ship. This case study aims to optimize a DWHX electric machine for these infinite reservoir applications. The infinite thermal reservoir is modeled simply by fixing the fluid temperature of the DWHX to the temperature of the infinite reservoir. The objective function is then changed to only consider the volume of

the motor and ignore the pump and radiator. The two temperatures that were simulated are 20°C and 90°C. These temperatures correspond to a large body of water and engine coolant respectively.

The results for each trial of the infinite reservoir study are shown in Table 7.8. Again, the optimization was performed three times to ensure the global minimum was reached. In this case study, the fitness function was within 1% of the other trials.

Table 7.8 - Fitness function values for each trial in infinite reservoir case study

	T_{fluid} [°C]	
	20	90
Trial #	Fitness Function Value	
1	-381.0	-289.1
2	-377.5	-289.5
3	-377.3	-288.7

The results from this case study are presented in Table 7.9. The torque density based on motor volume is 48.9 N-m/L and 38.4 N-m/L for a fluid temperature of 20°C and 90°C respectively. The torque density based on electromagnetic volume is 105.7 N-m/L and 82.9 N-m/L for a fluid temperature of 20°C and 90°C respectively. Notice that the current density is 25.9 and 20 A/mm^2 respectively. This is significantly higher than typically current densities. Also, notice that the efficiencies are much lower at 83.2 and 88.7 respectively. The optimization finds these higher current densities because it does not consider the extra heat rejection required by the resulting inefficiencies.

Table 7.9 - Optimization results for infinite reservoir case study

	T_{fluid} [°C]	
	20	90
D [mm]	72.6	70.4
L [mm]	27.6	34
J [A/mm^2]	25.9	20
EM Torque Density [N-m/L]	105.7	82.9
System Torque Density [N-m/L]	48.9	38.4
Efficiency	83.2	88.7
Fitness Value	-376.62	-289.67

The optimal micro-hydrofoil array characteristic dimensions in this case study are presented in Table 7.10. The difference only differences between these characteristic dimensions and the ones previously reported are the S_t/L_c ratio and number of features.

Table 7.10 - Optimal micro-hydrofoil geometries for infinite reservoir case study

T_{fluid} [°C]							
20				90			
S_t/L_c	2.2	L_c	0.2	S_t/L_c	2.2	L_c	0.2
S_l/L_c	5	$N_{f,t}$	47	S_l/L_c	5	$N_{f,t}$	51
H/L_c	2.5	$N_{f,l}$	27	H/L_c	2.5	$N_{f,l}$	33

7.7 Discussion

In the case studies presented, the form factor of the electric machine was a "pancake style". This means that the length of the machine was much smaller than its diameter. Also in the infinite reservoir study, the machine efficiencies for the optimal concepts were much lower than in the initial sizing case study. The lower efficiencies are expected for the infinite reservoir study. The idea of the DWHX electric machines is that you trade machine efficiency for torque density. However, in the initial sizing case studies the optimization found solutions that were much more efficient which is counter intuitive. The reason for the higher efficiencies is the radiator sizing. Lower efficiencies produce

more heat that the radiator must reject. More heat leads to larger radiators. To satisfy the tradeoff between motor volume and radiator volume the optimization found motors with higher efficiencies than expected. The fitness can be revised if a smaller motor is desired as compared to the radiator volume.

In the initial sizing study the radiator volume was a weak function of ΔT_{amb} between 10°C and 80°C. The results are replotted and normalized against total system volume and displayed in Figure 7.9. Notice that the percentage volume of total system volume is a weak function of ΔT_{amb} between 10°C and 80°C. It seems like the there is an optimal ratio of motor volume to radiator volume for ΔT_{amb} between 10°C and 80°C. Above 80°C, the radiator can get much smaller because of the increased driving force, but the motor must get larger as to not exceed the thermal limits.

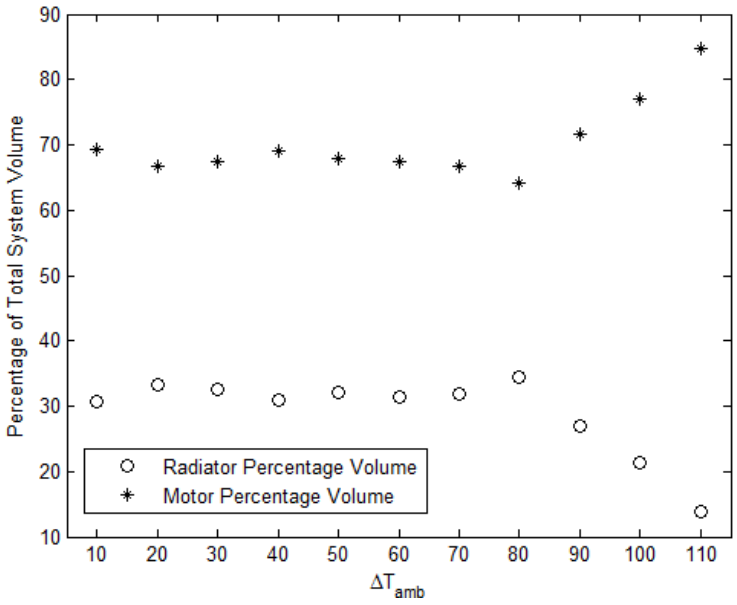

Figure 7.9 - Percentage motor and radiator volume of total system volume against ΔT_{amb} for the initial sizing case study

The trends presented in the initial sizing study are expected hold for various are power of machines. This is because the power of an electric machine is proportional to

the volume of the machine. Also the trends shown here have applicability to other types of machine that do not have a rotor heat source; such as interior permanent magnet and switched reluctance. The trends shown here do not have applicable when the speed of the machine changes. Increases in speed increase the core loss, which changes the location of maximum heat flux. In this case, another cooling technique needs to be used. Furthermore, the trends do not have applicable when the class of radiator, type of pump, or fitness function changes. Variations in these machine type, speed, radiator class, pump type, and fitness function are beyond the scope of this work.

It cannot be stated with ultimate certainty that the global minimum was located unless a full search of the entire hyperspace is performed. However, it should be noted that the results from the case studies are not expected to have been impacted by numerical failures in the particle swarm optimization. The PSO was performed three times for each test case. This diminishes the risk that the optimization was stuck in a local minimum. Furthermore, the large number of particles (32) along with the constriction method ensures the hyperspace was sufficiently explored.

The increased thermal conductivity of the windings combined with the proposed advanced cooling technology allows for high heat transfer rates without reaching the thermal limits of the wire insulation. The increased effective thermal conductivity of the windings, utilizing thermally conductive epoxy as the filler material, is on the same order as the thermal conductivity of the core. While most of the heat from the machine is transferred into the DWHX, some of the heat still travels to the frame. The increased thermal conductivity of the system means there is reduced temperature drop from the windings to the frame. This results in drastically increased frame temperatures. The frame

temperatures from the case studies presented above were ~140°C. 140°C far exceeds the typical safe touch limit and must be considered when packaging a DWHX electric machine. In traction drive applications the DWHX electric machine would not be touch accessible but would require a hot surface hazard label.

7.8 Summary

This chapter has presented a novel advanced cooling technique termed the direct winding heat exchanger (DWHX). This technique places an advanced heat exchanger between the winding bundles on the stator. This cooling technique dramatically reduces the thermal resistance from the stator windings to the ambient. An integrated thermal-electromagnetic model was detailed. This model was used in conjunction with particle swarm optimization to perform initial sizing and infinite reservoir case studies. In the initial sizing case study, the torque density of the system was 23.2 N-m/l and the torque density based on electromagnetic volume is 66.8 N-m/L. In the infinite reservoir case study, the torque density based on motor volume was 48.9 N-m/L and 38.4 N-m/L for a fluid temperature of 20°C and 90°C respectively. The torque density based on electromagnetic volume was 105.7 N-m/L and 82.9 N-m/L for a fluid temperature of 20°C and 90°C respectively.

CHAPTER 8

CONCLUSIONS

8.1 Summary and Conclusions

This work has addressed the design of next-generation, high torque density electrical machines through numerical optimization using an integrated thermal-electromagnetic design tool that accounts for advanced cooling technology. This was accomplished by first developing a parametric thermal model of electric machines. The thermal model includes a slot transformation technique that transforms typical slot geometries into polar coordinates for computational efficiency. This technique was validated to within 2% of high-fidelity FEA thermal analysis of the actual slot geometries. In addition, the thermal model includes frame modeling technique that accounts for the three-dimensional conduction within the frame. Similarly, this technique was validated to within 5% error as compared to a three-dimensional FEA of an electric machine. The parametric model was implemented using a finite difference technique, which aids in computational efficiency. The algorithm used to implement the FD parametric thermal model was detailed. This parametric model was also implemented in a transient model. The transient model utilized a frame capacitance technique that accounts for the three-dimensional frame capacitance. The frame capacitance technique was validated to within 5% and 6.5% for the quasi and fully-transient cases as compared to a three-dimensional FEA of an electric machine. An initial experimentation was preformed and the results showed the thermal model was within +5°C of the experimental results.

An advanced cooling technique, termed a direct winding heat exchanger, was presented. This technique involves placing a heat exchanger directly next to the windings

in the stator. The parametric thermal model was extended to include the advanced cooling technique. Initial case studies were performed to assess the effectiveness of the advanced cooling method. The case studies showed the possibility of an 8x increase in torque density over naturally cooled machines. This increase was obtained due to the marked increase in the convective heat transfer to the heat transfer fluid achieved by the micro-feature enhanced meso-channels. This lead to a need for Nusselt number and friction factor correlations to assess the optimal tradeoff between heat transfer and pressure drop in micro-feature enhanced channels.

This work identified micro-hydrofoil arrays as a solution to the tradeoff between heat transfer and pressure drop. Subsequently, an empirical approach to developing Nusselt number and friction factor correlations for aligned micro-hydrofoil arrays under single-phase cross flow was presented. The approach involved the testing of a 3^{3-1} orthogonal testing matrix of micro-hydrofoil arrays. The test pieces were manufactured using in house micro-milling technology. A test bench was developed to assess the thermal and flow performance of the micro-feature arrays. Data reduction and uncertainty analysis was performed for the Nusselt number and friction factor data. Two models were developed using a multi-linear regression and compared to an existing model. The existing model achieved an R^2 value of 0.793 with 95% of the data falling within ± 21.2% of the predicted performance for the Nusselt number correlation. The existing model achieved an R^2 value of 0.291 with 95% of the data falling within ± 33.4% for the friction factor correlation. The final Nusselt number correlation achieves an R^2 value of 0.99 with 95% of the data falling within ± 4.9% resulting in a 4x reduction in prediction error for micro-hydrofoil arrays. The final friction factor correlation achieves an R^2 value

of 0.92 with 95% of the data falling within ± 10.2% resulting in a 3x reduction in prediction error for the micro-hydrofoil arrays. Finally, a methodology for determining the optimal micro-feature enhanced heat exchanger was presented. This methodology allows the designer to assess the tradeoffs between heat transfer and pressure drop of micro-feature enhanced heat exchangers.

The parametric thermal model, advanced cooling technique, Nusselt number correlation and friction factor correlation were combined with an electromagnetic model. This resulted in an integrated thermal-electromagnetic model capable of simulating DWHX electric machines. The integrated thermal-electromagnetic model included a module for radiator and pump sizing. The model was then used with particle swarm optimization to quickly determine the optimal conceptual design. Initial sizing studies were preformed to assess the sizing of an optimal DWHX electric machine. The first case study was used to understand the tradeoffs between motor sizing and radiator sizing. The second case study was performed to assess the size of the DWHX electric machine when considering an infinite thermal reservoir. In the initial sizing case study, the torque density of the system was 23.2 N-m/l and the torque density based on electromagnetic volume is 66.8 N-m/L. In the infinite reservoir case study, the torque density based on motor volume was 48.9 N-m/L and 38.4 N-m/L for a fluid temperature of 20°C and 90°C respectively. The torque density based on electromagnetic volume was 105.7 N-m/L and 82.9 N-m/L for a fluid temperature of 20°C and 90°C respectively.

Pursuant to the work summarized above, and presented in the preceding chapters, the following conclusions can be drawn:

1. Transformation of typical slot geometries into polar coordinates predicts maximum winding temperature in 1.1s to within 2% of an FEA prediction of actual slot geometries.
2. Modeling three-dimensional frame conduction with an equivalent thermal resistance predicts maximum windings temperatures in 1.1s to within 5% of a three-dimensional FEA prediction of an electric machine.
3. Modeling three-dimensional frame capacitance with an equivalent frame density predicts maximum temperatures in 41.5s to within 5% accuracy for the quasi-transient cases and 6.5% accuracy for the fully-transient cases of an three-dimensional FEA prediction of an electric machine.
4. The parametric thermal model of an electric machine achieves +5°C accuracy when compared to experimental data.
5. The developed Nusselt number correlation achieves an R^2 value of 0.99 with 95% of the data falling within ± 2.5% resulting in a 4x reduction in prediction error for micro-hydrofoil thermal performance over an existing model.
6. The developed friction factor correlation achieves an R^2 value of 0.92 with 95% of the data falling within ± 10.2% resulting in a 4x reduction in prediction error for micro-hydrofoil thermal performance over an existing model.
7. DWHX cooling technology achieves current densities of 14.1 and 25.9 A/mm^2 leading to torque densities based on system volume of 23.2 and 105.7 N-m/L for heat dissipation to a radiator and infinite thermal reservoir respectively.

8.2 Contributions

Pursuant the work summarized above and presented in the preceding chapters the following contributions were made:

- A parametric half slot model of an electric machines was developed and implemented using a finite difference approach
- A slot transformation technique that transforms typical slot geometries into polar coordinates for calculation simplicity was developed
- A frame modeling technique that accounts the three dimensional conduction of the frame within the two dimensional parametric thermal model was developed
- A frame capacitance technique that accounts for the three dimensional frame capacitance through the use of an effective frame density was developed
- A novel advanced cooling technology for electric machine, termed the DWHX, which places an advanced heat exchanger between the winding bundles on the stator, was developed.
- An empirically based Nusselt number correlation for micro-hydrofoil arrays was developed.
- An empirically based friction factor correlation for micro-hydrofoil arrays was developed.
- A methodology for determining the optimal micro-feature heat exchanger through tradeoffs between heat transfer and pressure drop was developed
- A method for accelerated optimal conceptual designs for electric machines was developed.

- The following papers have been published or are currently under review:

1. S. A. Semidey and J. R. Mayor, "Parametric Fin Array Optimization for Radial Flux Machines Considering Time Varying Loads," *ASME Conference Proceedings,* vol. 2011, pp. T10062-T10062-7, 2011.
2. S. A. Semidey, D. Yao, J. R. Mayor, R. G. Harley, and T. G. Habetler, "Optimal Electromagnetic-Thermo-Mechanical Integrated Design Candidate Search and Selection for Surface-Mount Permanent-Magnet Machines Considering Load Profiles," Industry Applications, IEEE Transactions on, vol. 47, pp. 2460-2468, 2011.
3. J. R. Mayor and S. A. Semidey, "Generic electric machine thermal model development using an automated finite difference approach," in 2009 IEEE International Electric Machines and Drives Conference, IEMDC '09, May 3, 2009 - May 6, 2009, Miami, FL, United states, 2009, pp. 137-143.
4. S. A. Semidey and J. R. Mayor, "Steady-State Parametric Thermal Model of Electric Machines using a Finite Difference Approach" submitted for inclusion in IEEE Transactions on Industrial Applications, 2012.
5. S. A. Semidey and J. R. Mayor, "Transient Parametric Thermal Model of Electric Machines using a Finite Difference Approach" submitted for inclusion in IEEE Transactions on Industrial Applications, 2012.
6. S. A. Semidey and J. R. Mayor, "Design and Optimization of Direct Winding Cooled SMPM Electric Machines" Submitted for inclusion in IEEE Transactions on Industrial Applications, 2012.

7. S. A. Semidey and J. R. Mayor, "Empirical Investigation of Aligned Micro-Hydrofoils under single-phase Cross Flow Part 1 - Nusselt Number Correlation" Submitted for inclusion in Journal of Thermal Science and Engineering Applications, 2012.
8. S. A. Semidey and J. R. Mayor, "Empirical Investigation of Aligned Micro-Hydrofoils under single-phase Cross Flow Part 2 - Friction Factor Correlation" Submitted for inclusion in Journal of Thermal Science and Engineering Applications, 2012.

- A Provisional Patent for the DWHX advanced cooling technology has been filed under “Direct Winding Heat Exchanger” (GTRC ID 5536) serial number 61/536,326.

8.3 Recommendations and Future Work

During the course of this study several additions and extensions to the work were considered. These additions and extensions are presented here as recommendations for future work.

- Thermal Model Additions and Considerations

The parametric thermal model for electric machines that has been developed could be expanded further. For instance the typical cooling methods described only considered external air cooling. The thermal model could be extended to include internal air cooling and possibly water jackets. Furthermore the model contains provision for a finned frame. However an FEA validation must be completed for the finned framed modeling technique.

The initial experimental validation was performed on one machine. Experimental validation of electric machines is an expensive venture. A 10kW permanent magnet machine can cost anywhere from $1000 to $5000, depending on the manufacturer. Furthermore, manufacturers are reluctant to divulge machine geometries. Therefore an experimental validation requires two machines. One needs to be disassembled and measured while the other can be thermal tested. To further prove the accuracy of the thermal model, more experimentation is required, other power levels and machine geometries should be tested. The thermal model is not expected to fail at other power levels or machines geometries, but a conclusion statement of the general applicability of the model cannot be made without extra experimentation.

- Thermal Model Extensions

The parametric thermal model has been demonstrated on one electric machine topology, Surface Mount Permanent Magnet. The parametric thermal model can be extended to include other topologies such as, interior permanent magnet, induction, and switched reluctance. These topologies have some heat generation in the rotor. This heats leaves through the shaft and through the stator. A method for accounted for this addition heat transfer could be developed. This would increase the abilities of the thermal model and lead to optimal design studies considering multiple topologies.

- Effective Thermal Conductivity Verification

The effective thermal conductivity model used to model the wire bundles was verified using standard materials. It would interesting to assess the validity of the model when considering advanced materials such as those mentioned in the DWHX optimization study. Furthermore the effective thermal conductivity study only considered round wire.

A similar study could be performed for square wire. Square wire allows for higher packing factors and could result in much higher effective thermal conductivities.

- Micro-Hydrofoil Extensions

The presented Nusselt number and friction factor correlations for micro-hydrofoil arrays needs to be extended. This can be done is several ways. First the Reynolds number range could be increased. Also the fluid could be changed and a Prandtl number included in the Nusselt number correlation. The ranges for S_t/L_c, S_l/L_c and H_f/L_c could be increased, but would require the manufacture of more micro-hydrofoil test arrays.

The micro-hydrofoil study could also be extended to include staggered arrays. Staggered arrays would increase the feature density of the micro-hydrofoil arrays leading to increased heat transfer. It would be interesting to see how the feature density influences pressure drop as compared to micro-studs.

A more complete comparison between micro-hydrofoil and micro-stud arrays needs to be made. This can be done by performing a similar empirical study as performed in chapters 5 and 6 for the micro-stud arrays. The comparison should also include consideration of the machining time required to produce the arrays.

- DWHX Electric Machine Optimization Extensions

This study has introduced a novel advanced cooling technique termed the DHWX. The technique was simulated based on the thermal model developed in chapter 2. An optimization method was developed and performed to produce an optimal conceptual design. Before this design can be manufactured, a design finalization must be performed. This design finalization involves an electromagnetic FEA, DWHX validation, and mechanical designs. The electromagnetic FEA must be preformed to ensure the

miniaturization of the DWHX electric machine is electromagnetically possible. The DWHX thermal model needs to be experimentally validated to ensure the expected thermal performance is achievable. The mechanical design must be performed on the frame, end caps, and rotor. Once design finalization is completed, a test machine can be built and evaluated.

APPENDIX A

SLOT TYPE 3 TRANSFORMATION

This appendix details the slot transformation technique for slot type 3 that was first introduced in chapter 2. Many stator geometries have features that do not correspond to either a radius of an angle in polar coordinates. To simplify the proposed algorithm the actual slot geometry was modeled with features that correspond to either a radius or an angle. While the authors recognize that there are multiple variations of stator slot geometries currently utilized in practice, this study has chosen a specific slot geometry to demonstrate the proposed modeling technique. The development of the transformation of real stator slot geometries into a polar coordinate form is demonstrated below. Figure A.1 shows the definition of the actual slot dimensions that were used to calculate the radii and angles of the modeled slot geometry.

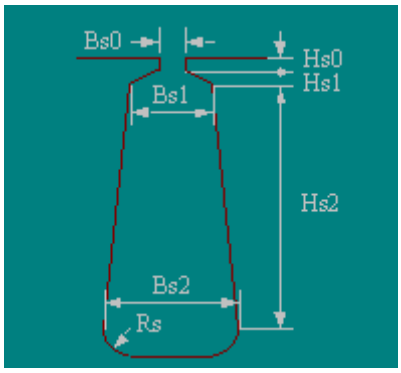

Figure A.1 - Slot Type 3 geometric definitions

Using (1) through (10) the actual slot dimensions were transformed into the modeled slot geometry polar dimensions.

$$A_{slot\,total} = \frac{Bs1 + Bs2}{2} \cdot \left(Hs2 + Rs\right) + \frac{Bs0 + Bs1}{2} \cdot Hs1 \tag{1}$$

Equation (1) is the approximate cross sectional area of the actual slot. This area was used to ensure the modeled slot winding area is the same as the actual slot.

$$R_{inner} = \frac{DiaSGap}{2} \tag{2}$$

In (2) *DiaSGap* is the diameter of the air gap.

$$\theta_{foot} = \cos^{-1}\left(\frac{2 \cdot R_{foot\ inner}^2 - Bs0^2}{2 \cdot R_{foot\ inner}^2}\right) / 2 \tag{3}$$

Equation (3) is the angle corresponding to the edge of the foot.

$$R_{foot\ outer} = \frac{DiaSGap}{2} + Hs0 + \frac{Hs1}{2} \tag{4}$$

Equation (4) is the radius that corresponds to outside of the foot.

$$R_{windings} = \frac{DiaSGap}{2} + Hs0 + Hs1 \tag{5}$$

Equation (5) is the radius that corresponds to the bottom of the windings.

$$R_{avg} = R_{foot\ inner} + Hs0 + Hs1 + \frac{Hs2}{2} \tag{6}$$

Equation (6) is the average radius of the slot, which is used to calculate the angle of the tooth.

$$\theta_{tooth} = \tan^{-1}\left(\frac{Bs1 + Bs2}{R_{avg}}\right) \tag{7}$$

Equation (7) is the angle that corresponds to the tooth.

$$R_{stator\ inner} = \sqrt{\frac{A_{slot\ total}}{\theta_{tooth}} + R_{foot\ outer}^2} \tag{8}$$

Equation (8) is the radius that corresponds to the top of the slot.

$$R_{stator\ outer} = \frac{DiaSYoke}{2} \tag{9}$$

In (9), *DiaSYoke* is the diameter of the yoke.

$$\theta_{outer} = \frac{\pi}{Nm} \tag{10}$$

In (10), *Nm* is the number of slots. Equation (10) is the angle that corresponds to half of the tooth. Figure A.2 shows the modeled slot geometry on top of the actual slot geometry for comparison.

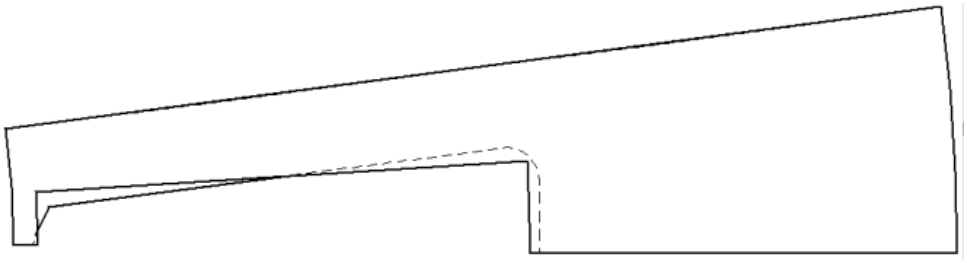

Figure A.2 - Overlay of actual slot geometry and modeled slot geometry

APPENDIX B

FULL FACTORIAL MULTI-LINEAR REGRESSION ALGORITHM

This appendix will detail the algorithm used to perform linear regressions of every possible combination of interactions. The flowchart for the algorithm is illustrated in Figure B.1. The algorithm begins with the interactions matrix. The columns of this matrix are all of the interactions to be correlated. For instance, if the data consisted of only two parameters, A and B, then there would be five possible interactions (A, B, AB, A^2, and B^2) when only second-order interactions are considered. The rows consist of the data for each interaction. The total number of possible combinations corresponds to the total number of possible combinations of interaction. This is calculated by raising 2 to the power of the number of interactions. The algorithm then enters a for loop. At each iteration, the iteration number is converted to a binary vector whose length is equal to the number of possible interactions. This vector is then repeated into a matrix whose number of rows corresponds to the number of data points. The element wise matrix multiplication between the resulting matrix and the interactions matrix is calculated. A linear regression is then performed on the resulting matrix. The residuals from the regression are then recorded. The loop continues until linear regression has been performed on all possible combinations of the interactions. The residuals from each linear regression are reported for determination of the best combination of interactions for the correlation.

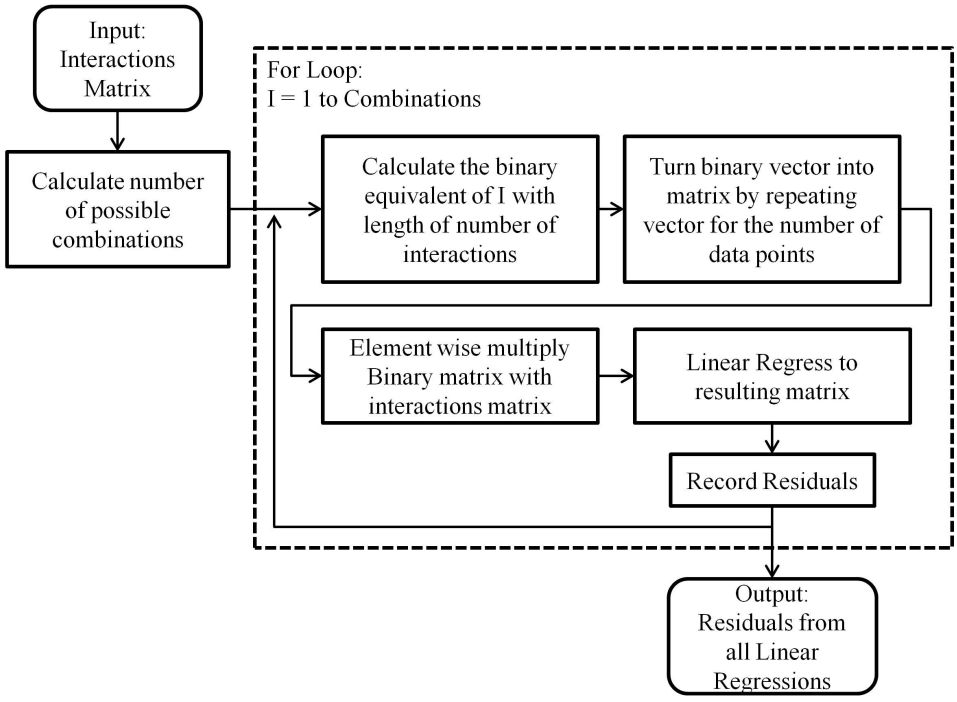

Figure B.1 - Flow chart for performing linear regression on all possible combinations of interaction

APPENDIX C

TABLE OF NUSSELT NUMBER AND UNCERTAINTY FOR ALL DATA POINTS

This appendix shows the Nusselt number for every data point used in the multi-linear regression. The uncertainty at each data point is presented in the table. The maximum and minimum percentage uncertainty errors are highlighted in red and green respectively. The average percentage uncertainty error is 3.67%.

Data Point Number	Nu	σ_{Nu}	Avg Error	Data Point Number	Nu	σ_{Nu}	Avg Error	Data Point Number	Nu	σ_{Nu}	Avg Error
1	20.35	1.03	5.06%	37	21.52	0.60	2.81%	73	19.52	0.86	4.41%
2	21.00	0.77	3.68%	38	19.97	0.55	2.76%	74	16.90	0.72	4.28%
3	21.16	0.78	3.68%	39	22.29	0.91	4.08%	75	18.39	0.80	4.35%
4	20.00	0.73	3.63%	40	20.24	0.56	2.77%	76	19.90	1.19	6.00%
5	20.90	1.08	5.15%	41	20.97	0.83	3.94%	77	19.14	0.84	4.38%
6	20.05	0.73	3.63%	42	19.40	0.74	3.81%	78	19.03	0.83	4.39%
7	21.41	1.12	5.21%	43	19.48	0.54	2.75%	79	17.21	0.96	5.59%
8	21.76	1.14	5.26%	44	22.30	0.91	4.06%	80	18.22	1.05	5.74%
9	18.81	0.67	3.58%	45	22.06	0.62	2.83%	81	18.86	1.10	5.85%
10	20.72	1.06	5.11%	46	21.20	0.84	3.96%	82	17.30	0.97	5.61%
11	19.34	0.95	4.93%	47	21.01	0.59	2.80%	83	19.49	1.16	5.94%
12	19.54	0.71	3.61%	48	19.85	0.55	2.76%	84	17.26	0.97	5.60%
13	19.58	0.71	3.61%	49	21.82	0.88	4.03%	85	17.95	0.78	4.32%
14	21.28	0.79	3.69%	50	21.23	0.84	3.97%	86	20.63	1.26	6.12%
15	20.51	1.04	5.10%	51	19.59	0.75	3.83%	87	18.16	1.04	5.73%
16	20.96	0.77	3.68%	52	21.81	0.88	4.04%	88	17.98	0.78	4.33%
17	19.58	0.71	3.62%	53	22.87	0.94	4.12%	89	19.53	1.16	5.95%
18	21.76	1.15	5.27%	54	22.76	0.94	4.13%	90	19.79	0.88	4.43%
19	21.49	1.13	5.24%	55	19.71	0.76	3.85%	91	18.86	1.10	5.84%
20	20.25	1.02	5.04%	56	21.44	0.60	2.81%	92	17.84	0.77	4.33%
21	18.91	0.68	3.58%	57	18.99	0.52	2.73%	93	17.27	0.74	4.29%
22	18.94	0.68	3.59%	58	20.51	0.80	3.91%	94	19.94	0.88	4.43%
23	20.20	1.02	5.05%	59	22.02	0.89	4.04%	95	18.95	1.11	5.86%
24	20.55	0.75	3.66%	60	20.60	0.81	3.92%	96	20.24	0.90	4.45%
25	20.21	1.02	5.06%	61	22.37	0.91	4.09%	97	20.87	1.29	6.17%
26	19.48	0.97	4.96%	62	22.39	0.92	4.09%	98	18.69	0.82	4.37%
27	20.99	0.77	3.68%	63	20.76	0.82	3.94%	99	20.35	1.24	6.08%
28	21.13	1.10	5.19%	64	22.32	0.63	2.84%	100	20.33	0.91	4.46%
29	21.33	1.11	5.20%	65	20.61	0.57	2.78%	101	19.95	1.20	6.01%
30	20.23	0.74	3.65%	66	21.17	0.59	2.80%	102	18.34	1.06	5.76%
31	21.81	1.15	5.27%	67	19.10	0.52	2.74%	103	18.67	0.82	4.37%
32	20.68	0.76	3.67%	68	21.70	0.61	2.82%	104	20.50	1.25	6.10%
33	19.49	0.97	4.96%	69	21.72	0.61	2.82%	105	19.86	1.19	6.00%
34	21.04	0.78	3.68%	70	21.41	0.60	2.81%	106	20.34	0.91	4.46%
35	22.04	1.17	5.31%	71	20.38	0.57	2.77%	107	17.19	0.74	4.29%
36	20.66	0.76	3.67%	72	19.34	0.53	2.74%	108	19.29	0.85	4.40%

Data Point Number	Nu	σ_{Nu}	Avg Error	Data Point Number	Nu	σ_{Nu}	Avg Error	Data Point Number	Nu	σ_{Nu}	Avg Error
109	20.51	0.74	3.61%	145	27.30	0.93	3.40%	181	18.65	1.03	5.53%
110	21.13	0.54	2.54%	146	28.07	0.62	2.20%	182	20.42	1.18	5.80%
111	21.90	0.82	3.74%	147	27.05	0.92	3.39%	183	17.70	0.95	5.39%
112	19.78	0.50	2.51%	148	26.95	0.58	2.17%	184	18.60	0.77	4.14%
113	20.47	0.74	3.62%	149	29.53	0.66	2.24%	185	19.62	0.82	4.19%
114	20.78	0.53	2.54%	150	29.78	1.07	3.59%	186	19.18	0.80	4.16%
115	21.54	0.55	2.56%	151	27.11	0.59	2.17%	187	20.08	0.85	4.21%
116	23.23	0.89	3.85%	152	24.51	0.79	3.23%	188	19.09	1.07	5.60%
117	22.63	0.86	3.80%	153	31.28	1.15	3.68%	189	19.69	0.83	4.19%
118	22.02	0.83	3.75%	154	30.01	1.08	3.60%	190	19.03	1.07	5.61%
119	21.40	0.55	2.56%	155	25.86	0.55	2.14%	191	18.74	0.78	4.15%
120	24.01	0.63	2.64%	156	28.78	1.01	3.51%	192	20.19	0.85	4.22%
121	23.24	0.89	3.85%	157	30.03	1.08	3.60%	193	17.50	0.72	4.09%
122	22.77	0.87	3.82%	158	25.76	0.55	2.14%	194	19.41	0.81	4.18%
123	18.99	0.47	2.49%	159	27.04	0.59	2.18%	195	17.84	0.97	5.44%
124	22.42	0.58	2.59%	160	25.89	0.86	3.32%	196	17.50	0.71	4.08%
125	24.14	0.95	3.94%	161	31.31	1.16	3.70%	197	18.23	0.75	4.12%
126	21.53	0.80	3.72%	162	28.57	0.63	2.22%	198	19.74	1.13	5.73%
127	23.31	0.61	2.62%	163	24.48	0.79	3.23%	199	19.81	1.13	5.72%
128	20.66	0.75	3.64%	164	24.47	0.52	2.11%	200	20.50	1.20	5.84%
129	22.33	0.58	2.59%	165	27.67	0.95	3.44%	201	19.14	1.08	5.63%
130	24.14	0.64	2.65%	166	31.25	0.72	2.29%	202	19.71	1.12	5.70%
131	19.85	0.50	2.51%	167	31.17	0.72	2.29%	203	20.09	1.16	5.77%
132	21.45	0.80	3.71%	168	28.62	0.63	2.22%	204	18.52	1.02	5.53%
133	21.42	0.79	3.71%	169	25.82	0.55	2.14%	205	19.64	0.82	4.20%
134	22.17	0.57	2.59%	170	28.82	1.01	3.52%	206	18.57	1.03	5.53%
135	24.05	0.95	3.93%	171	24.18	0.51	2.10%	207	19.29	0.80	4.17%
136	24.05	0.64	2.65%	172	24.58	0.79	3.23%	208	20.57	1.20	5.85%
137	23.17	0.61	2.62%	173	31.40	1.16	3.71%	209	19.99	0.84	4.22%
138	23.17	0.61	2.61%	174	31.41	0.72	2.30%	210	17.44	0.71	4.09%
139	23.94	0.94	3.94%	175	26.14	0.87	3.32%	211	18.69	0.78	4.15%
140	23.39	0.91	3.88%	176	28.96	1.02	3.52%	212	20.13	1.16	5.78%
141	22.23	0.84	3.78%	177	24.12	0.51	2.10%	213	18.14	0.75	4.12%
142	20.51	0.52	2.54%	178	30.05	0.68	2.26%	214	18.14	0.75	4.12%
143	22.58	0.86	3.81%	179	25.87	0.86	3.32%	215	20.01	1.16	5.77%
144	20.86	0.53	2.54%	180	30.02	0.68	2.25%	216	17.76	0.96	5.43%

Data Point Number	Nu	σ_{Nu}	Avg Error	Data Point Number	Nu	σ_{Nu}	Avg Error	Data Point Number	Nu	σ_{Nu}	Avg Error
217	22.63	0.55	2.44%	253	32.12	1.07	3.33%	289	29.08	0.75	2.58%
218	20.82	0.50	2.38%	254	35.57	1.27	3.56%	290	32.76	0.89	2.72%
219	23.57	0.80	3.40%	255	31.70	1.05	3.31%	291	31.06	0.82	2.65%
220	22.02	0.72	3.28%	256	33.63	0.70	2.08%	292	28.77	1.16	4.04%
221	22.72	0.76	3.33%	257	39.66	1.52	3.84%	293	34.43	1.56	4.54%
222	22.49	0.55	2.44%	258	37.85	0.83	2.20%	294	34.40	0.96	2.78%
223	21.13	0.68	3.24%	259	33.64	1.15	3.43%	295	34.35	0.95	2.78%
224	21.79	0.53	2.41%	260	38.00	1.41	3.72%	296	35.58	1.01	2.83%
225	20.50	0.65	3.19%	261	33.55	0.70	2.07%	297	27.11	0.68	2.52%
226	23.73	0.59	2.48%	262	35.82	0.77	2.14%	298	29.33	0.76	2.59%
227	20.84	0.50	2.39%	263	33.73	1.16	3.44%	299	27.14	1.06	3.89%
228	19.32	0.45	2.34%	264	41.13	1.62	3.93%	300	29.20	1.19	4.07%
229	23.77	0.59	2.48%	265	38.07	1.42	3.72%	301	27.25	1.06	3.89%
230	21.41	0.70	3.26%	266	35.65	1.27	3.57%	302	32.92	1.45	4.40%
231	23.80	0.81	3.42%	267	41.43	0.95	2.29%	303	31.10	0.83	2.66%
232	20.17	0.48	2.37%	268	39.91	0.90	2.25%	304	32.98	1.45	4.40%
233	19.95	0.63	3.17%	269	31.89	1.06	3.33%	305	31.02	1.31	4.24%
234	20.53	0.49	2.37%	270	31.49	0.64	2.02%	306	31.39	1.33	4.25%
235	22.94	0.77	3.36%	271	31.60	0.64	2.02%	307	36.14	1.69	4.69%
236	23.06	0.57	2.46%	272	41.12	0.94	2.28%	308	27.21	1.06	3.90%
237	20.80	0.67	3.22%	273	37.79	1.40	3.71%	309	34.54	1.57	4.56%
238	21.41	0.70	3.26%	274	37.95	0.83	2.19%	310	36.05	1.69	4.69%
239	24.16	0.83	3.44%	275	39.59	0.89	2.24%	311	31.15	1.32	4.24%
240	22.08	0.54	2.43%	276	36.10	1.29	3.58%	312	35.80	1.02	2.84%
241	22.29	0.74	3.31%	277	39.43	1.50	3.81%	313	27.25	0.69	2.52%
242	19.55	0.46	2.34%	278	35.98	0.77	2.14%	314	31.14	0.83	2.66%
243	19.91	0.63	3.16%	279	37.57	0.82	2.18%	315	29.22	1.19	4.07%
244	20.46	0.49	2.38%	280	33.21	0.69	2.07%	316	32.95	0.90	2.73%
245	22.42	0.74	3.32%	281	39.34	1.50	3.81%	317	34.65	0.97	2.79%
246	20.89	0.67	3.21%	282	33.53	1.15	3.42%	318	29.26	0.76	2.60%
247	19.93	0.63	3.16%	283	31.58	0.64	2.02%	319	33.04	1.46	4.42%
248	19.78	0.47	2.36%	284	40.84	0.93	2.28%	320	36.20	1.70	4.71%
249	24.15	0.60	2.50%	285	35.81	0.76	2.13%	321	36.04	1.03	2.85%
250	21.16	0.51	2.40%	286	39.19	0.88	2.24%	322	34.81	1.59	4.57%
251	22.27	0.54	2.44%	287	40.93	1.60	3.92%	323	32.92	0.90	2.73%
252	23.26	0.79	3.39%	288	40.94	1.61	3.92%	324	27.12	0.68	2.52%

APPENDIX D

INITIAL PARTICAL SWARM OPTIMIZATION VS GENETIC ALGORITHM STUDY FOR FIN ARRAY OPTIMIZATION

D.1 Introduction

Over the years, there has been a push to produce smaller and more efficient electric machines. Thermal effects are the limiting factor for higher power density electric machines. Therefore, a tool that can optimize the motor's cooling geometries is desirable. This tool could also be integrated with electromagnetic design to enable closed loop design of electric machines considering thermal effects.

Traditional thermal modeling of electric machines involves approximating the machine as a simple cylinder with internal heat generation [96]. This conservative model is not applicable to state of the art machine design due because it cannot predict winding temperatures. Thermal circuits (TC) [9, 20, 25, 97, 98] and finite element analysis (FEA) [32] are the two current advanced numerical thermal modeling approaches of electric machines. Boglietti et al found TC could predict winding temperature to within ± 5° C using a so called lumped parameter method [20]. Even though this technique requires little computational time, it requires an experimental fit of the lumped parameters and therefore cannot be used effectively in the design process. Moreover, TC is not a true 2-D heat transfer model and it accounts for spatial effects through experimental compensation. FEA is accurate and generic and therefore can be used to optimize selected final designs. However, FEA requires large setup and computational time, therefore limiting the use of FEA in the optimal design selection process.

There are many nonlinear global optimization techniques that could be utilized to optimize the motor cooling geometries such as Simulated Annealing, Evolutionary Algorithms, Branch and Bound etc [90]. This appendix will focus on a relatively new global optimization technique called particle swarm optimization. This technique was first introduced by Kennedy and Eberhart and is based on swarm theory that mimics the movement of a flock of birds or a school of fish [93, 94]. The movement of the particle through the solution hyperspace is governed by a stochastic weighted sum of the previous velocity, velocity to the local best solution, and velocity to the global best solution. This technique has recently gained popularity due to its speed, accuracy, and ease of implementation.

Each particle position represents a possible solution in the problem hyperspace. The position of the particles is governed by Eqn. (1).

$$\vec{x}_i(t) = \vec{x}_i(t-1) + \vec{v}_i(t) \tag{1}$$

There are many versions of the particle velocity equation including the original formulation [93], constriction method [99], fully informed method [100], and inertia weight method [101]. This work utilizes the inertia weight method as seen in Eqn. (2).

$$\vec{v}_i(t) = \varphi_{ic} \cdot \vec{v}_i(t) + \varphi_1 \cdot \overrightarrow{rand} \cdot \left(\vec{p}_i - \vec{x}_i(t-1)\right) + \varphi_2 \cdot \overrightarrow{rand} \cdot \left(\vec{p}_g - \vec{x}_i(t-1)\right) \tag{2}$$

The inertia weight method utilizes a weighted sum between the pervious particle velocity, distance to the local best solution and distance to the global best solution.

Pursuant to the study by Shi [102], the procedure adopted to implement the PSO algorithm in this study is listed below:

1. Initialize the particle positions in the solution hyperspace

2. Evaluate the fitness function for each particle

3. Evaluate the local best solution and the global best solution and their respective locations $\vec{p}_i$

and $\vec{p}_g$

4. Update each particles velocity and position based on the (3) and (2)

5. Repeat steps two through four until the convergence criterion is meet.

The evaluation of the global best solution and local best solution involves the selection of a swarm topology. Many swarm topologies exist including the global best, ring, wheel, pyramid, and Von Neumann [95]. This study utilizes the global best topology in which every particle communicates with each other and is not limited to communicating with its nearest neighbors. The local best solution is evaluated by keeping track of where each particle has been and determining its best previous position.

D.2 Thermal Modeling Description

Figure D.1a illustrates the thermal problem for electric machines depicting the classical cylinder with internal heat generation using a first law formulation. However the electric machines internal complexities increase the difficulty of the problem. The electric machine has complex internal geometries and is made up of several different materials including copper, lacquer, slot liner paper, magnetic steel, aluminum, etc. The machine heats loads come from losses which include copper loss (ohmic heating), $\dot{E}_{copper}$, core loss (electromagnetic hysteresis), $\dot{E}_{core}$, windage loss (drag), and frictional loss. Windage and frictional losses are typically neglected because of their relative small values when compared with copper and core loss. The machine also has heat dissipation through either

active or passive cooling, which is typically in the form of a convective load ($Q_{convection}$). An analytical solution to the transient temperature distribution is difficult to obtain due to the complexities of the geometry, materials, and heating and cooling loads.

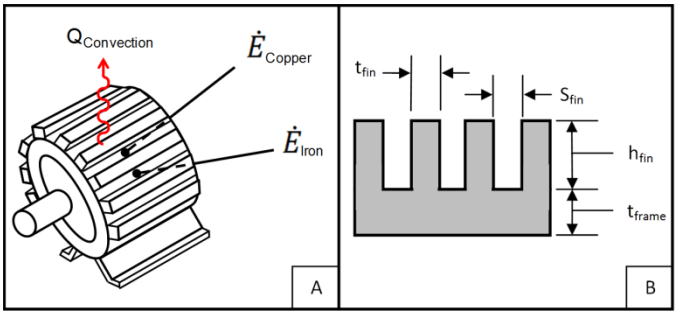

Figure D.1 - Illustration of thermal problem in electric machines (A) and illustration of fin array (B)

Figure D.1b illustrates the geometries of the fin array considered in this study. This illustration is a linear representation of the actual radial fin array shown on the motor in Figure D.1a.

The majority of electric machine applications are fixed speed and load. However the increasing use of speed control leads to some applications in which the speed and torque of the electric machine vary with time such as in HEVs, vertical shaft wind generators, or variable speed HVAC fans. These transient variations lead to time varying losses. This appendix will consider three different transient load-cycles representative of constant speed, constant torque and mixed load scenarios, illustrated in Figure D**.2**. Notice that for the third load case, the core loss increases to twice the rated value for a short period of time. This would occur if an electric machine were to suddenly increase speed $\sqrt{2}$ times rated speed (core loss is proportional to speed squared). These cases are contrived and are only used to test the performance of the optimization technique.

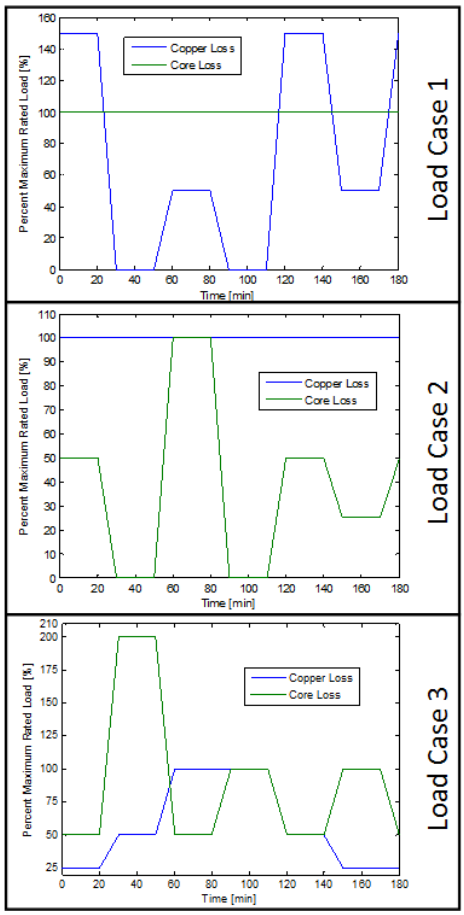

Figure D.2 - Transient load cycles used in case study

D.3 Summary of Thermal Modeling Approach

A generic thermal model that can be integrated with a nonlinear global optimization technique is needed to optimize electric machine cooling geometries under time varying loads. The generic thermal model used is this study utilizes a parametric finite difference approach to numerically calculate the temperature distribution within the stator of the electric machine. The model utilizes several simplifying assumptions reduce the complex nature of the thermal problem in order to decrease computational time without sacrificing accuracy. The thermal model ignores radiation, axial thermal transport, and thermal

transport to the rotor. The thermal model also treats the windings as one material with an effective thermal conductivity.

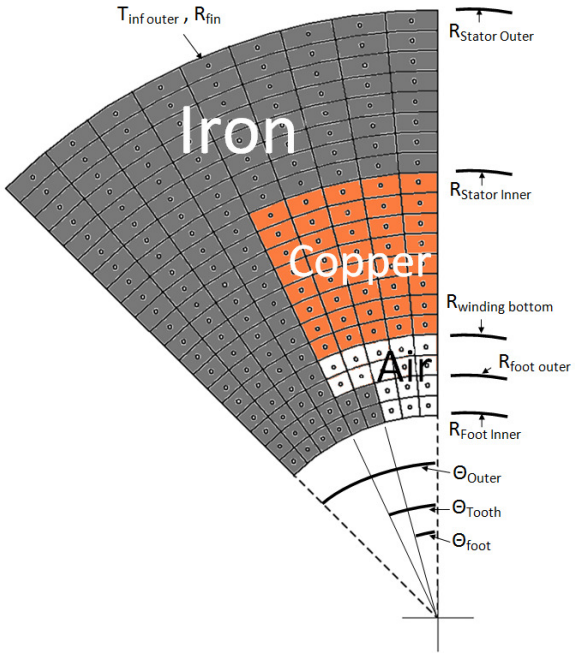

Figure D.3 - Segmented half slot model

The thermal model uses the symmetry of stator to simply the modeled geometry. This is known as a half slot model. The thermal model has an automated mesh generation and segmentation that accounts for the different materials in the geometry. Figure D.3 shows the segmented half slot model used in the thermal model. The details of the model are presented in [39, 103].

The frame of the electric machine is modeled using classical fin resistance theory. As a preliminary investigation, this study only considers radial fins in a vertical orientation under buoyancy driven flow. The vertical orientation, natural convection problem has been well documented and the traditional Nusselt number correlation, presented in Eqn. (3), is adopted [34].

$$\overline{Nu}_s = \left[\frac{576}{\left(Ra_s S_f / L_{fr}\right)^2} + \frac{2.97}{\left(Ra_s S_f / L_{fr}\right)^{1/2}} \right]^{-1/2} \tag{3}$$

The heat transfer coefficient is calculated using this Nusselt number correlation. The heat transfer coefficient is then used to calculate the thermal resistance of the entire fin array. The thermal resistance is then applied the boundary of the half slot model illustrated in Figure D.3 as R_{fin}. The maximum winding temperature is then calculated by solving the linear system of equations from the finite difference formulation.

D.4 Fin Array Optimization

The design of the fin array is a tradeoff between the mass of the fin array, containing volume, aspect ratio of the fins, and cooling rates. It is desired to have a light and small fin array that is easy to manufacture, but provides sufficient cooling. Therefore, the fitness function for the problem, as seen in Eqn. (4), was formulated as a weighted sum of the fin array mass, the containing volume, and a penalty function. The constants C_{m} and C_{v} account for the differences in order of magnitude between the mass and volume of the fin array. The mass and volume of the fin array are calculated using Eqn. (5) and Eqn. (6) respectively. The penalty function, Eqn. (6), is the sum of the penalties for temperature and additional-cost, presented in Eqn. (7) and Eqn. (8) respectively. The temperature penalty, Φ_t, penalizes fin array designs that allow the winding temperature to increase past an allowable temperature which could damage the motor windings. This temperature in most cases is 150°C. The additional-cost penalty, Φ_{a-c}, accounts for the additional cost of manufacturing a fin array high aspect ratio fin arrays. Assuming a nominal aspect ratio of 3:1, the penalty was formulated as a piecewise function with a linearly increasing penalty above the nominal value.

$$F = C_m \cdot m + C_v \cdot V + \Phi \tag{4}$$

$$m = \rho_f \cdot L_{fr} \cdot \left(N_f \cdot h_f \cdot t_f + 2\pi t_f\right) \tag{5}$$

$$V = \pi L_{fr} \cdot \left(R_{st} + t_f + h_f\right)^2 \tag{6}$$

$$\Phi = \Phi_t + \Phi_{a-c} \tag{7}$$

$$\Phi_t = \begin{cases} 0 & if\ T_w < T_a \\ \left(T_w - T_a\right)^2 & if\ T_w \geq T_a \end{cases} \tag{8}$$

$$\Phi_{a-c} = \begin{cases} 0 & if\ AR < 3 \\ 5\left(AR - 3\right) & if\ AR \geq 3 \end{cases} \tag{9}$$

The population size used for the PSO is a critical parameter for convergence. Reported typical values for population size range from 5-50 [95, 104]. If the number of particles is too low the PSO will not find the global minimum and will not converge to the same solution over several trials. If the number of particles is too large the PSO will have a longer convergence time and subsequently a large computational time. A study was performed to assess the fewest number of particles needed for consistent convergence. The initial distribution of particles must also be considered. In traditional PSO the particles are randomly distributed throughout the space. This study looks at setting an ordered initial distribution to increase convergence consistency.

Figure D.4 shows the three ordered initial distributions that were tested. Figure D.4a shows an eight particle population in a cubic distribution. Figure D.4b shows a twelve particle population in a three plane configuration. Figure D.4c shows a twenty particle in a four plane configuration.

Typical values for the weighting coefficients (φ_{ic}= 0.9, φ_1= 2, φ_2= 2) [95] did not lead towards convergence. These high values would make the particles oscillate around

the global optima. Lower values (φ_{ic} = 0.2, φ_1=.5, φ_2=.5) would converge quickly to a non-optimal solution. Therefore moderate values (φ_{ic} = 0.5, φ_1= 1.2, φ_2= 1.2) for the weighting coefficients were used.

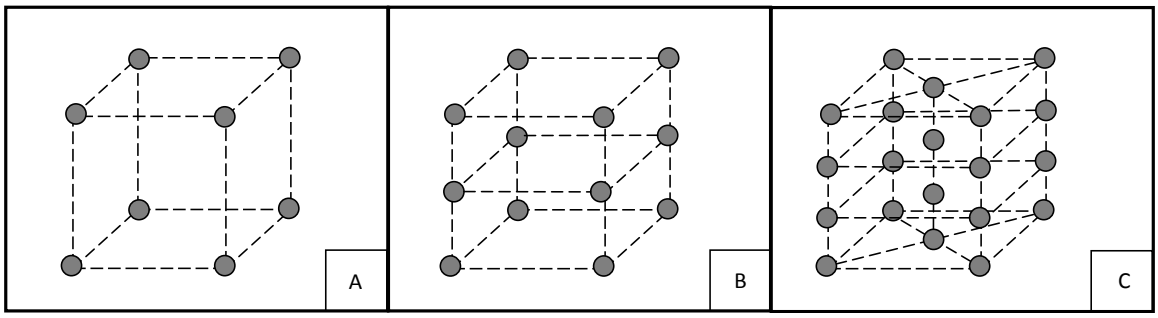

Figure D.4 - Initial particle positions trials. Eight particles in cube configuration (A), twelve particles in three plane configuration (B), and twenty particles in a four plane configuration

D.5 Results

The simulated motor was a surface mount permanent magnet machine. The active length is 85.6 mm and the stator diameter is 200 mm. The stator has twelve slots and has concentrated windings. The motor is rated for 10 kW of power and 40 Nm of torque and a peak power of 20 kW and peak torque of 80 Nm. The simulation was implemented in Matlab R2009b utilizing the parallel computing toolbox. The computer used had an AMD Phenom Quad-Core 2.3 GHz processor with 8 GB of RAM. The parallel computing toolbox in Matlab uses each core as a separate processor allowing for parallel computing leading to faster computation times.

D.6 Convergence Study

The convergence test was run using a steady state solution under full load conditions. The study looked at five trials for each of four different initial distributions. Table 1 shows the results from the convergence study. The eight-particle ordered configuration

could not find the global minimum and had a variance of the fitness of 372.9. The twelve-particle ordered configuration was able to find the global minimum but not consistently and had a variance of the fitness of 1.84. The twenty-particle ordered configuration found the global minimum in every case and had a variance of the fitness function of 0.002. The twenty particle random configuration failed to converge to the global minimum in two of the five trials, trials three and five, and had a variance of the fitness of 270.6.

Figure 5 shows the progress of twenty ordered particles throughout the hyperspace. Notice, at the 10 iteration mark, that the particles are beginning to converge to the global minimum. The convergence criteria in this study was set such the standard deviation of the fitness values for all particles was less than 0.2. Figure 6 shows the three particles fin height value versus the number of iterations. These particles seem to converge by iteration 30, however the convergence criteria was not met until iteration 39 in this case. This may suggest that the convergence criteria could be slackened.

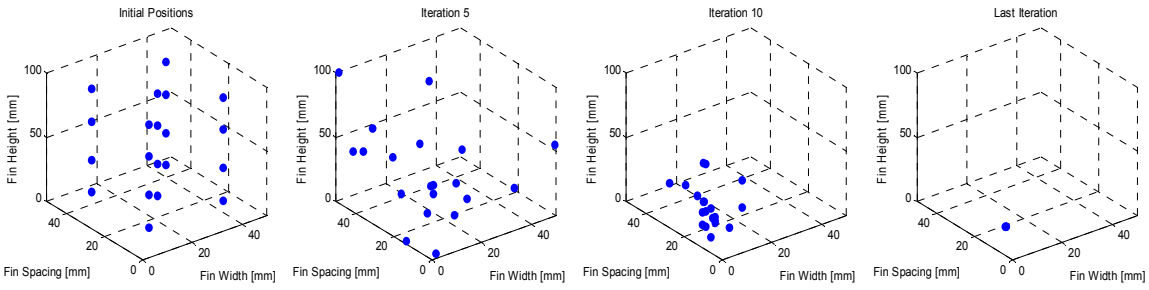

Figure D.5 - Sequence of particle convergence for 20 ordered particles

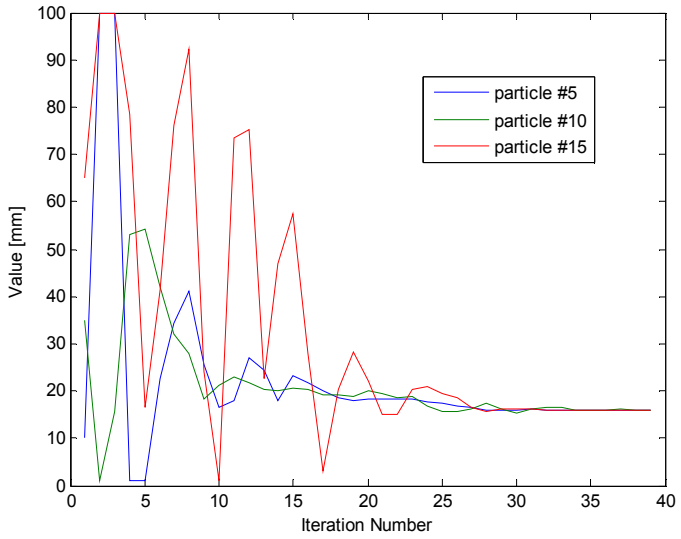

Figure D.6 - Convergence of fin height of three particles for the convergence study

Table D.1 - Convergence test results

		Fin Dimensions (mm)				
population size	Trial No.	h_f	w_f	s_f	No. of Iterations	F
8 - Ordered	1	70.8	8.7	49.9	24	74.2
	2	69.3	8.5	48.8	26	73.0
	3	71.4	8.8	50.0	25	74.3
	4	64.7	8.4	45.3	29	69.7
	5	18.3	4.8	10.2	41	29.8
12 - Ordered	1	19.6	5.0	11.2	42	31.0
	2	16.0	3.9	8.7	44	28.0
	3	15.5	3.6	8.4	47	27.9
	4	16.0	3.9	8.5	39	28.0
	5	15.3	3.6	8.2	40	27.9
20 - Ordered	1	15.7	3.8	8.5	40	27.9
	2	15.4	3.6	8.4	47	27.9
	3	15.5	3.7	8.4	41	27.9
	4	15.5	3.6	8.4	41	27.9
	5	16	3.9	8.6	39	28
20 - random	1	15.4	3.6	8.4	40	27.9
	2	16.1	4.0	8.6	43	28.1
	3	41.8	7.5	27.4	45	45.0
	4	15.4	3.6	8.3	56	27.9
	5	59.0	9.2	40.0	34	65.1

D.6.1 Comparison to Genetic Algorithm

The results from the convergence study were compared to a standard genetic algorithm (GA) technique. The GA technique used was a standard formulation found in the Matlab Optimization Toolbox. The GA was simulated ten times and the number of correct solutions was recorded. Out of the ten trials, GA only converged to the correct solution three times. Three out of ten is 50% less than the random initial distributions PSO case. These results are in line with the results reported in [92].

D.6.2 Case Studies of Time Varying Loads

The PSO was performed on the three fully-transient load profiles presented previously in Figure D.2. Figure D.7 shows the transient maximum winding temperature plot for each case using the optimal fin geometries. Observe that the winding temperature limit has been met, but not exceeded, in each case, thus suggesting an optimal thermal solution. Table D.2 shows the results from the case studies. Case 1 had the longest fins while case 2 had the shortest fins. In all cases the PSO took less than 55 iterations to converge. The aspect ratios of the optimal fin array for the three cases were 5.14:1, 3:1, and 3.7:1 respectively. The mass of the optimal fin array for the three cases were 1.76 kg, 0.88 kg, and 1.29 kg respectively. Finally, the containing volume of the optimal fin array for the three cases were 0.0087 m3 (8.7 L), 0.0077 m3 (7.7 L), and 0.008 m3 (8 L) respectively.

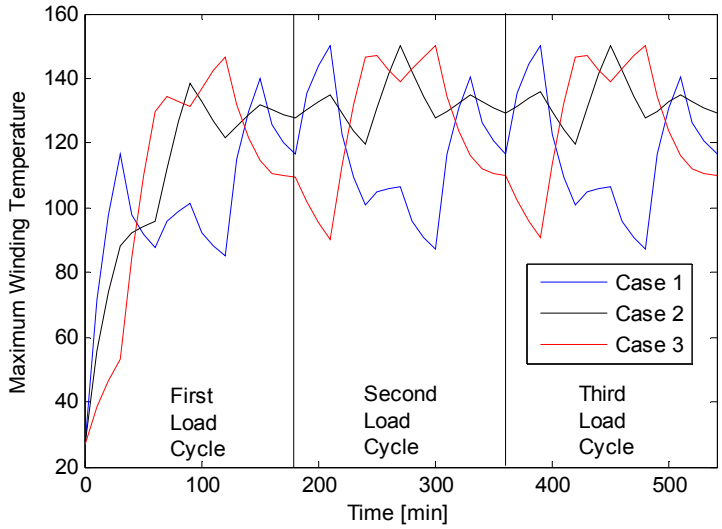

Figure D.7 - Transient temperature of maximum winding temperature for each case study

Table D.2 - Summary of case study results

		Fin Dimensions (mm)					
	Trial No.	h_f	w_f	s_f	No. of Iterations	Time	F
Case 1	1	18.5	3.6	8.2	46	63.4	35.8
	2	18.5	3.6	8.3	53	71.8	35.8
Case 2	1	10.8	3.6	10.2	49	43.2	8.9
	2	10.9	3.6	10.1	51	50.1	8.9
Case 3	1	13.7	3.7	8.5	45	106.4	23.2
	2	13.6	3.7	8.4	39	97.4	23.2

D.7 Discussion

The aspect ratios for case one and three were higher than the allowable value of 3:1. This indicates that the maximum cooling solution could not be found without incurring the penalty of additional manufacturing costs. The second case found a solution at the allowable aspect ratio, which lead to minimal mass. The reduction in aspect ratio and mass between cases one and two are 71% and 100% respectively, however the change in

volume is only 13%. This would imply that the optimal fin design is more dependent on mass and aspect ratio of the fin array than the containing volume.

The initial distribution and weighting coefficients were selected based on experiential knowledge of the PSO problem. A specific combination of initial distribution, number of particles, and weighting coefficients may exist that has more consistent and quicker global convergence. Future work will consider the optimal combination of parameters to improve convergence rates and consistency. Doctor et al. suggested using dual loop particle swarm algorithms to optimize the weighting coefficients for robotic searches [105].

The formulation of the temperature penalty is conservative. Motor windings typically fail because of prolonged exposure to temperatures that exceed the manufactures recommendations. These recommendations are based on the class of insulation of the windings. Future work will consider a more accurate and robust treatment of the temperature penalty by estimating remaining life of the insulation material based on thermal history.

D.8 Conclusion

Based on the work presented the following conclusions were drawn:

1. The application of particle swarm optimization to thermal design of electric machine under time varying loads was demonstrated and shown to be effective

2. The initial population distribution has a significant impact on the consistency of convergence

REFERENCES

[1] (2012). *Baldor Product Line*. Available: http://www.getpower.us/electric_motors.html

[2] C. DEMORRO. (2009). *Caterpillar Builds World's First Hybrid Bulldozer*. Available: http://gas2.org/2009/09/18/caterpillar-builds-worlds-first-hybrid-bulldozer/

[3] Green-Energy.net. (2010). *The Beginner's Guide to hybrid electric vehicle*. Available: http://www.energy-green.net/blog/articles/electric-vehicle/beginner-s-guide-to-hybrid-electric-vehicle-3.html

[4] J. Marks. (2010). *Linkage: Greening Air Travel*. Available: http://www.greensocal.net/2010/05/linkage-greening-air-travel.html

[5] V. Subrahmanyam, *Electric Drives*: The McGraw-Hill Companies, INC., 1996.

[6] A. Boglietti, A. Cavagnino, D. Staton, M. Shanel, M. Mueller, and C. Mejuto, "Evolution and modern approaches for thermal analysis of electrical machines," *IEEE Transactions on Industrial Electronics,* vol. 56, pp. 871-882, 2009.

[7] P. Mellor, D. Roberts, and D. Turner, "Lumped parameter thermal model for electrical machines of TEFCdesign," *IEE Proceedings B [see also IEE Proceedings-Electric Power Applications] Electric Power Applications,* vol. 138, pp. 205-218, 1991.

[8] Z. Lazarevic, R. Radosavljevic, and P. Osmokrovic, "A novel approach for temperature estimation in squirrel-cage induction motor without sensors," *IEEE Transactions on Instrumentation and Measurement,* vol. 48, pp. 753-757, 1999.

[9] S. Chowdhury, S. Chowdhury, and S. Pal, "An Interactive Software for the Analysis of Thermal Characteristics of Capacitor-Run Single-Phase Induction Motors," *Electric Power Components and Systems,* vol. 29, pp. 997-1011, 2001.

[10] R. Ibtiouen, S. Mezani, O. Touhami, N. Nouali, and M. Benhaddadi, "Application of lumped parameters and finite element methods to thethermal modeling of an induction motor," 2001, pp. 505-507.

[11] A. Boglietti, A. Cavagnino, M. Lazzari, A. Pastorelli, and D. Industriale, "A simplified thermal model for variable speed self cooled industrial induction motor," 2002.

[12] M. Valenzuela, P. Verbakel, and J. Rooks, "Thermal evaluation for applying TEFC induction motors on short-time and intermittent duty cycles," *IEEE Transactions on Industry Applications,* vol. 39, pp. 45-52, 2003.

[13] S. Mezani, N. Takorabet, and B. Laporte, "A combined electromagnetic and thermal analysis of induction motors," *IEEE Transactions on Magnetics,* vol. 41, 2005.

[14] O. Okoro, "Steady and transient states thermal analysis of a 7.5-kW squirrel-cage induction machine at rated-load operation," *IEEE Transactions on Energy Conversion,* vol. 20, 2005.

[15] C. Kral, A. Haumer, M. Haigis, H. Lang, and H. Kapeller, "Comparison of Measurements with a CFD Analysis and a Thermal Equivalent Circuit Model of a TEFC Induction Machine," 2006.

[16] C. Kral and A. Haumer, "Consistent equivalent circuit parameters of induction motors for the calculation of partial load efficiencies," 2008, pp. 698-705.

[17] C. Kral, A. Haumer, and T. Bäuml, "Thermal model and behavior of a totally-enclosed-water-cooled squirrel-cage induction machine for traction applications," *IEEE Transactions on Industrial Electronics,* vol. 55, p. 3555, 2008.
[18] A. Shenkman and M. Chertkov, "Experimental method for synthesis of generalized thermal circuit of polyphase induction motors," *IEEE Transactions on Energy Conversion,* vol. 15, 2000.
[19] C. Kral, T. Habetler, R. Harley, F. Pirker, G. Pascoli, H. Oberguggenberger, and C. Fenz, "Rotor temperature estimation of squirrel-cage induction motors by means of a combined scheme of parameter estimation and a thermal equivalent model," *IEEE Transactions on Industry Applications,* vol. 40, p. 1049, 2004.
[20] A. Boglietti, A. Cavagnino, and D. Staton, "TEFC induction motors thermal models: A parameter sensitivity analysis," *IEEE Trans. Ind. Appl,* vol. 41, pp. 756–763, 2005.
[21] D. Staton, A. Boglietti, and A. Cavagnino, "Solving the more difficult aspects of electric motor thermal analysis in small and medium size industrial induction motors," *IEEE Transactions on Energy Conversion,* vol. 20, 2005.
[22] A. Boglietti, A. Cavagnino, M. Parvis, A. Vallan, D. di Ingegneria Elettrica, and I. Turin, "Evaluation of radiation thermal resistances in industrial motors," *IEEE Transactions on Industry Applications,* vol. 42, pp. 688-693, 2006.
[23] A. Boglietti and A. Cavagnino, "Analysis of the endwinding cooling effects in TEFC induction motors," *IEEE Transactions on Industry Applications,* vol. 43, pp. 1214-1222, 2007.
[24] Y. K. Chin, E. Nordlund, and D. A. Staton, "Thermal analysis lumped-circuit model and finite element analysis," in *IPEC 2003 - 6th International Power Engineering Conference, November 27, 2003 - November 29, 2003*, Singapore, 2003, pp. 1019-1024.
[25] A. Boglietti, A. Cavagnino, and D. Staton, "Thermal sensitivity analysis for TEFC induction motors," 2004, pp. 160-165.
[26] A. Boglietti, A. Cavagnino, M. Pastorelli, D. Staton, A. Vagati, D. Industriale, and I. Turin, "Thermal analysis of induction and synchronous reluctance motors," *IEEE Transactions on Industry Applications,* vol. 42, pp. 675-680, 2006.
[27] D. G. Dorrell, "Combined Thermal and Electromagnetic Analysis of Permanent-Magnet and Induction Machines to Aid Calculation," *Industrial Electronics, IEEE Transactions on,* vol. 55, pp. 3566-3574, 2008.
[28] A. Armor, "Transient, three-dimensional, finite-element analysis of heat flow in turbine-generator rotors," *IEEE Transactions on Power Apparatus and Systems,* pp. 934-946, 1980.
[29] D. Sarkar, P. Mukherjee, and S. Sen, "Use of 3-dimensional finite elements for computation of temperature distribution in the stator of an induction motor," 1991, pp. 75-86.
[30] C. Hwang, S. Wu, and Y. Jiang, "Novel approach to the solution of temperature distribution in the stator of an induction motor," *IEEE Transaction on Energy Conversion,* vol. 15, pp. 401-406, 2000.
[31] F. Marignetti, V. Colli, and Y. Coia, "Design of Axial Flux PM Synchronous Machines through 3D Coupled Electromagnetic Thermal and Fluid dynamical Finite Elements Analysis," 2007.

[32] C. Liao, C. Chen, T. Katcher, S. Center, and T. Oaks, "Thermal management of AC induction motors using computational fluiddynamics modeling," 1999, pp. 189-191.
[33] *ANSYS Maxwell*. Available: http://www.ansys.com/Products/Simulation+Technology/Electromagnetics/Electromechanical+Design/ANSYS+Maxwell
[34] F. P. Incropera, *Fundamentals of heat and mass transfer*, 5th ed. ed. New York :: J. Wiley, 2002.
[35] Carpenter. Available: http://www.cartech.com/
[36] Available: www.matweb.com
[37] H. Kanzaki, K. Sato, and M. Kumagai, "A study of an estimation method for predicting the equivalent thermal conductivity of an electric coil," *Heat transfer. Japanese research,* vol. 21, pp. 123-138, 1992.
[38] L. Alberti and N. Bianchi, "A coupled thermal–electromagnetic analysis for a rapid and accurate prediction of IM performance," *IEEE Transactions on Industrial Electronics,* vol. 55, p. 3575, 2008.
[39] J. R. Mayor and S. A. Semidey, "Generic electric machine thermal model development using an automated finite difference approach," in *2009 IEEE International Electric Machines and Drives Conference, IEMDC '09, May 3, 2009 - May 6, 2009*, Miami, FL, United states, 2009, pp. 137-143.
[40] K. Rao, "Augmentation of heat transfer in the axial ducts of electrical machines with tape generated swirl flow," *IEEE Transactions on Power Apparatus and Systems,* pp. 2750-2756, 1983.
[41] C. Jeon, M. Yoon, and S. Kauh, "Heat transfer enhancement in the unfinned frame of an externally cooled induction motor," *Heat Transfer Engineering,* vol. 21, pp. 25-34, 2000.
[42] T. Nakahama, K. Suzuki, S. Hashidume, F. Ishibashi, and M. Hirata, "Cooling airflow in unidirectional ventilated open-type motor for electric vehicles," *IEEE Transaction on Energy Conversion,* vol. 21, pp. 645-651, 2006.
[43] C. Micallef, S. Pickering, K. Simmons, and K. Bradley, "An alternative cooling arrangement for the end region of a totally enclosed fan cooled (TEFC) induction motor," 2008.
[44] J. Mugglestone, S. Pickering, and D. Lampard, "Prediction of the heat transfer from the end winding of a TEFCstrip-wound induction motor," 1999, pp. 484-486.
[45] W. Rippel and D. Kobayashi, "Direct Lamination Cooling of Motors For Electric Vehicles," 2003.
[46] K. Rahman, N. Patel, T. Ward, J. Nagashima, F. Caricchi, F. Crescimbini, G. Motors-ATC, and C. Torrance, "Application of direct drive wheel motor for fuel cell electric and hybrid electric vehicle propulsion system," 2004.
[47] L. Zhenguo, L. Ru, G. Jianhong, F. Deping, and X. Bin, "Study on the integration of electrical machines adopted evaporative cooling technology," 2007, pp. 1099-1102.

[48] X. Zhang, H. Wang, G. Zhang, and G. Gu, "Temperature characteristics in the stator model of a permanent magnet motor by water-cooling and evaporative cooling," in *Electrical Machines and Systems, 2005. ICEMS 2005. Proceedings of the Eighth International Conference on*, 2005, pp. 2408-2410 Vol. 3.

[49] Y. Peles, A. Kosar, C. Mishra, C. J. Kuo, and B. Schneider, "Forced convective heat transfer across a pin fin micro heat sink," *International Journal of Heat and Mass Transfer,* vol. 48, pp. 3615-3627, 2005.

[50] A. Kosar and Y. Peles, "Thermal-hydraulic performance of MEMS-based pin fin heat sink," *Journal of heat transfer,* vol. 128, p. 121, 2006.

[51] W. M. Kays, M. E. Crawford, and B. Weigand, *Convective heat and mass transfer*. Maidenhead: McGraw-Hill Education, 2005.

[52] J. Thome and L. Consolini, "Mechanisms of Boiling in Microchannels: Critical Assessment," *Microfluidics Based Microsystems,* pp. 83-105, 2010.

[53] J. Thome, "State-of-the-art overview of boiling and two-phase flows in microchannels," *Heat Transfer Engineering,* vol. 27, pp. 4-19, 2006.

[54] J. Thome, "Boiling in microchannels: a review of experiment and theory," *International Journal of Heat and Fluid Flow,* vol. 25, pp. 128-139, 2004.

[55] S. Kandlikar, "Heat transfer mechanisms during flow boiling in microchannels," *Journal of heat transfer,* vol. 126, p. 8, 2004.

[56] S. Kandlikar and W. Grande, "Evolution of Microchannel Flow Passages--Thermohydraulic Performance and Fabrication Technology," *Heat Transfer Engineering,* vol. 24, pp. 3-17, 2003.

[57] S. Kandlikar, "Fundamental issues related to flow boiling in minichannels and microchannels," *Experimental Thermal and Fluid Science,* vol. 26, pp. 389-407, 2002.

[58] I. Mudawar and D. Maddox, "Enhancement of critical heat flux from high power microelectronic heat sources in a flow channel," *Journal of Electronic Packaging,* vol. 112, p. 241, 1990.

[59] D. Maddox and I. Mudawar, "Single-and two-phase convective heat transfer from smooth and enhanced microelectronic heat sources in a rectangular channel," *Journal of heat transfer,* vol. 111, p. 1045, 1989.

[60] Y. Lie, J. Ke, W. Chang, T. Cheng, and T. Lin, "Saturated flow boiling heat transfer and associated bubble characteristics of FC-72 on a heated micro-pin-finned silicon chip," *International Journal of Heat and Mass Transfer,* vol. 50, pp. 3862-3876, 2007.

[61] D. McNeil, A. Raeisi, P. Kew, and P. Bobbili, "A comparison of flow boiling heat-transfer in in-line mini pin fin and plane channel flows," *Applied Thermal Engineering,* 2010.

[62] D. B. Tuckerman and R. F. W. Pease, "High-performance heat sinking for VLSI," *Electron Device Letters, IEEE,* vol. 2, pp. 126-129, 1981.

[63] S. S. Mehendale, A. M. Jacobi, and R. K. Shah, "Fluid Flow and Heat Transfer at Micro- and Meso-Scales With Application to Heat Exchanger Design," *Applied Mechanics Reviews,* vol. 53, pp. 175-193, 2000.

[64] W. Qu and I. Mudawar, "Experimental and numerical study of pressure drop and heat transfer in a single-phase micro-channel heat sink," *International Journal of Heat and Mass Transfer,* vol. 45, pp. 2549-2565, 2002.

[65] C. B. Sobhan and S. V. Garimella, "A COMPARATIVE ANALYSIS OF STUDIES ON HEAT TRANSFER AND FLUID FLOW IN MICROCHANNELS," *Microscale Thermophysical Engineering,* vol. 5, pp. 293-311, 2001/10/01 2001.

[66] N. García-Hernando, A. Acosta-Iborra, U. Ruiz-Rivas, and M. Izquierdo, "Experimental investigation of fluid flow and heat transfer in a single-phase liquid flow micro-heat exchanger," *International Journal of Heat and Mass Transfer,* vol. 52, pp. 5433-5446, 2009.

[67] X. F. Peng and G. P. Peterson, "Convective heat transfer and flow friction for water flow in microchannel structures," *International Journal of Heat and Mass Transfer,* vol. 39, pp. 2599-2608, 1996.

[68] I. Hassan, P. Phutthavong, and M. Abdelgawad, "MICROCHANNEL HEAT SINKS: AN OVERVIEW OF THE STATE-OF-THE-ART," *Microscale Thermophysical Engineering,* vol. 8, pp. 183-205, 2004/01/01 2004.

[69] G. L. Morini, "Single-phase convective heat transfer in microchannels: a review of experimental results," *International Journal of Thermal Sciences,* vol. 43, pp. 631-651, 2004.

[70] S. G. Kandlikar and W. J. Grande, "Evaluation of Single Phase Flow in Microchannels for High Heat Flux Chip Cooling—Thermohydraulic Performance Enhancement and Fabrication Technology," *Heat Transfer Engineering,* vol. 25, pp. 5-16, 2004/12/01 2004.

[71] R. S. Prasher, J. Dirner, J. Y. Chang, A. Myers, D. Chau, D. He, and S. Prstic, "Nusselt number and friction factor of staggered arrays of low aspect ratio micropin-fins under cross flow for water as fluid," *Journal of heat transfer,* vol. 129, p. 141, 2007.

[72] A. Kosar, C. Mishra, and Y. Peles, "Laminar flow across a bank of low aspect ratio micro pin fins," *Journal of fluids engineering,* vol. 127, p. 419, 2005.

[73] K. A. Moores and Y. K. Joshi, "Effect of tip clearance on the thermal and hydrodynamic performance of a shrouded pin fin array," *Journal of heat transfer,* vol. 125, p. 999, 2003.

[74] B. Short Jr, P. Raad, and D. Price, "Performance of pin fin coldwalls constructed of cast aluminum: Part I: Friction factor correlations," *Proc. AIAA J. Thermophys. Heat Transfer,* vol. 16, pp. 389-396, 2002.

[75] B. Short Jr, P. Raad, and D. Price, "Performance of pin fin coldwalls constructed of cast aluminum: Part II: Colburn $ J $-factor correlations," *Proc. AIAA J. Thermophys. Heat Transfer,* vol. 16, pp. 397-403, 2002.

[76] M. K. Chyu, Y. C. Hsing, and V. Natarajan, "Convective Heat Transfer of Cubic Fin Arrays in a Narrow Channel," *Journal of Turbomachinery,* vol. 120, pp. 362-367, 1998.

[77] A. Siu-Ho, W. Qu, and F. Pfefferkorn, "Experimental Study of Pressure Drop and Heat Transfer in a Single-Phase Micropin-Fin Heat Sink," *Journal of Electronic Packaging,* vol. 129, pp. 479-487, 2007.

[78] A. M. S. Ho, W. Qu, and F. Pfefferkorn, "Pressure Drop and Heat Transfer in a Single-Phase Micro-Pin-Fin Heat Sink," *ASME Conference Proceedings,* vol. 2006, pp. 213-220, 2006.

[79] A. Kosar, "Two-phase pressure drop across a hydrofoil-based micro pin device using R-123," *Experimental Thermal and Fluid Science,* vol. 32, pp. 1213-1221, 2008.
[80] A. Kosar and Y. Peles, "Boiling heat transfer in a hydrofoil-based micro pin fin heat sink," *International Journal of Heat and Mass Transfer,* vol. 50, pp. 1018-1034, 2007.
[81] J. Y. Min, S. P. Jang, and S. J. Kim, "Effect of tip clearance on the cooling performance of a microchannel heat sink," *International Journal of Heat and Mass Transfer,* vol. 47, pp. 1099-1103, 2004.
[82] A. Žukauskas, "Heat Transfer from Tubes in Crossflow," in *Advances in Heat Transfer*. vol. Volume 8, P. H. James and F. I. Thomas, Eds., ed: Elsevier, 1972, pp. 93-160.
[83] SPEED. Available: http://www.speedlab.co.uk/index.html
[84] S. A. Semidey, D. Yao, J. R. Mayor, and R. G. Harley, "Optimal electromagnetic-thermo-mechanical integrated design for surface mount permanent magnet machines considering load profiles," in *Energy Conversion Congress and Exposition (ECCE), 2010 IEEE*, 2010, pp. 3646-3653.
[85] S. A. Semidey, D. Yao, J. R. Mayor, R. G. Harley, and T. G. Habetler, "Optimal Electromagnetic-Thermo-Mechanical Integrated Design Candidate Search and Selection for Surface-Mount Permanent-Magnet Machines Considering Load Profiles," *Industry Applications, IEEE Transactions on,* vol. 47, pp. 2460-2468, 2011.
[86] Y. Duan, R. G. Harley, and T. G. Habetler, "A Useful Multi-objective Optimization Design Method for PM Motors Considering Nonlinear Material Properties," presented at the IEEE Energy Coversion Congress and Exposition, San Jose, CA, Sept. 20-24, 2009.
[87] Z. Q. Zhu and D. Howe, "Instantaneous Magnetic Field Distribution in Permanent Magnet Brushless DC Motors, Part I: Open-Circuit Field," *IEEE Tranactions on Magnetics,* vol. 29, pp. 124-135, Jan. 1993 1993.
[88] Y. Duan, R. G. Harley, and T. G. Habetler, "Method for Multi-objective Optimized Designs of Surface Mount Permanent Magnet Motors with Concentrated or Distributed Stator Windings," presented at the International Electric Machines and Drive Conference, Miami,FL, May 3-6, 2009.
[89] Swiftech. (2012). Available: http://www.swiftech.com/MCRX20-QP-RADIATOR-SERIES.aspx#tab2
[90] O. Nelles, "Nonlinear system identification," *Measurement Science and Technology,* vol. 13, p. 646, 2002.
[91] O. Wen, D. Zarko, and T. A. Lipo, "Permanent Magnet Machine Design Practice and Optimization," in *Industry Applications Conference, 2006. 41st IAS Annual Meeting. Conference Record of the 2006 IEEE*, 2006, pp. 1905-1911.
[92] Y. Duan, R. Harley, and T. Habetler, "Comparison of Particle Swarm Optimization and Genetic Algorithm in the design of permanent magnet motors," 2009, pp. 822-825.
[93] J. Kennedy and R. Eberhart, "Particle swarm optimization," 1995, pp. 1942-1948.
[94] R. Eberhart and J. Kennedy, "A new optimizer using particle swarm theory," 1995.

[95] Y. del Valle, G. Venayagamoorthy, S. Mohagheghi, J. Hernandez, and R. Harley, "Particle swarm optimization: Basic concepts, variants and applications in power systems," *IEEE Transactions on Evolutionary Computation,* vol. 12, p. 171, 2008.
[96] V. Subrahmanyam, *Electric drives: concepts and applications*: Tata McGraw-Hill Publishing Company, 1996.
[97] M. Baggu and H. Hess, "Evaluation of an Existing Thermal Model of an Induction Motor and its Further Application to an Advanced Cooling Topology," 2007.
[98] Y. Chin, E. Nordlund, and D. Staton, "Thermal analysis–Lumped circuit model and finite element analysis," 2003, pp. 952-957.
[99] M. Clerc and J. Kennedy, "The particle swarm-explosion, stability, and convergence in amultidimensional complex space," *IEEE Transactions on Evolutionary Computation,* vol. 6, pp. 58-73, 2002.
[100] R. Mendes, J. Kennedy, and J. Neves, "The fully informed particle swarm: Simpler, maybe better," *IEEE Transactions on Evolutionary Computation,* vol. 8, pp. 204-210, 2004.
[101] J. Kennedy, R. Eberhart, and Y. Shi, *Swarm intelligence*: Morgan Kaufmann Publishers, 2001.
[102] Y. Shi, "Feature article on particle swarm optimization," *IEEE Neural Network Society, Feature Article,* pp. 8–13, 2004.
[103] S. A. Semidey, Y. Duan, J. R. Mayor, and R. Harley, "Optimal Electromagnetic-Thermo-Mechanical Integrated Design for Surface Mount Permanent Magnet Machines Considering Load Profiles," in *2010 ECCE*, Atlanta, GA, United States, 2010.
[104] M. Alrasheed, C. de Silva, and M. Gadala, "A Modified Particle Swarm Optimization Scheme and Its Application in Electronic Heat Sink Design," 2007.
[105] S. Doctor, G. Venayagamoorthy, and V. Gudise, "Optimal PSO for collective robotic search applications," 2004, pp. 1390-1395.